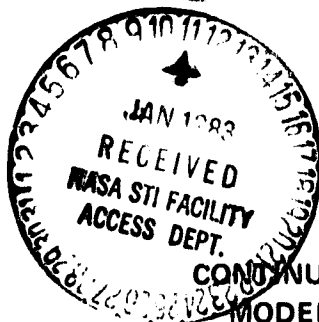


## **General Disclaimer**

### **One or more of the Following Statements may affect this Document**

- This document has been reproduced from the best copy furnished by the organizational source. It is being released in the interest of making available as much information as possible.
- This document may contain data, which exceeds the sheet parameters. It was furnished in this condition by the organizational source and is the best copy available.
- This document may contain tone-on-tone or color graphs, charts and/or pictures, which have been reproduced in black and white.
- This document is paginated as submitted by the original source.
- Portions of this document are not fully legible due to the historical nature of some of the material. However, it is the best reproduction available from the original submission.

NASA CR-167977  
BEERS 1-82-16-23



CONTINUED DEVELOPMENT OF A DETAILED  
MODEL OF ARC DISCHARGE DYNAMICS

by B.L. Beers, V.W. Pine, and S.T. Ives

BEERS ASSOCIATES, INC.

Post Office Box 2549  
Reston, Virginia 22090

Prepared for

NATIONAL AERONAUTICS AND SPACE ADMINISTRATION

NASA Lewis Research Center

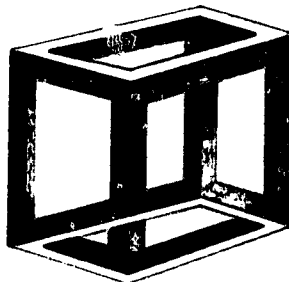
Contract NAS3-22530

(NASA-CR-167977) CONTINUED DEVELOPMENT OF A  
DETAILED MODEL OF ARC DISCHARGE DYNAMICS  
Contract Report, Aug. 1980 - Mar. 1982  
(Beers Associates, Inc.) 156 p  
HC A08/MF A01

N8J-16234

Unclass  
02375

CSCL 20L G3/76



# BEERS ASSOCIATES

|  |  |  |  |   |  |
|--|--|--|--|---|--|
| 1. Report No.<br>NASA CR-167977  |  | 2. Government Accession No.                          |  | 3. Recipient's Catalog No.  |  |
| 4. Title and Subtitle<br>Continued Development of a Detailed Model of Arc Discharge Dynamics   |  |  |  | 5. Report Date<br>15 December 1982  |  |
|  |  |  |  | 6. Performing Organization Code   |  |
| 7. Author(s)<br>B. L. Beers, V.W. Pine & S.T. Ives   |  |  |  | 8. Performing Organization Report No.<br>1-82-16-23                                   |  |
| 9. Performing Organization Name and Address<br>BEERS ASSOCIATES, INC.<br>Post Office Box 2549<br>Reston, Virginia 22090  |  |  |  | 10. Work Unit No.<br>YOV 8405   |  |
|  |  |  |  | 11. Contract or Grant No.<br>NAS3-22530   |  |
| 12. Sponsoring Agency Name and Address<br>National Aeronautics and Space Administration<br>Lewis Research Center<br>Cleveland, Ohio 44136  |  |  |  | 13. Type of Report and Period Covered<br>Contract Report<br>August, 1980 - March 1982 |  |
|  |  |  |  | 14. Sponsoring Agency Code<br>5532  |  |
| 15. Supplementary Notes  |  |  |  |   |  |
| 16. Abstract<br><br><p>Using a previously developed set of codes (SEMC, CASCAD, ACORN), a parametric study was performed to quantify the parameters which describe the development of a single electron indicated avalanche into a negative tip streamer. The electron distribution function in Teflon is presented for values of the electric field in the range of <math>4 \times 10^8</math> volts/meter to <math>4 \times 10^9</math> volts/meter. A formulation of the scattering parameters is developed which shows that the transport can be represented by three independent variables. The distribution of ionization sites is used to indicate an avalanche. The self consistent evolution of the avalanche is computed over the parameter range of scattering set.</p> <p style="text-align: center;">ORIGINAL PAGE 19<br/>OF POOR QUALITY</p> |  |  |  |   |  |
| 17. Key Words (Suggested by Author(s))<br><br>Arc discharge, streamer development, electron transport, avalanche, electron distribution function.  |  |  | 18. Distribution Statement<br><br>Unclassified - Unlimited |   |  |
| 19. Security Classif. (of this report)<br>Unclassified   |  | 20. Security Classif. (of this page)<br>Unclassified |  | 21. No. of Pages<br>152   |  |
|  |  |  |  | 22. Price*  |  |

\* For sale by the National Technical Information Service, Springfield, Virginia 22161

## TABLE OF CONTENTS

|  | <u>Page</u> |
|--|-------------|
| 1. INTRODUCTION.....                                 | 1           |
| 2. CODE MODIFICATIONS.....                           | 3           |
| 2.1 SEMC MODIFICATIONS.....                          | 3           |
| 2.2 CASCAD MODIFICATIONS.....                        | 9           |
| 2.3 ACORN MODIFICATIONS.....                         | 10          |
| 3. COMPUTATIONAL STUDIES.....                        | 11          |
| 3.1 SEMC STUDIES.....                                | 11          |
| 3.1.1 SCATTERING PARAMETER FORMULATION: SCALING..... | 12          |
| 3.1.2 SEMC RESULTS.....                              | 19          |
| 3.1.2.1 MOBILITY.....                                | 19          |
| 3.1.2.2 DIFFUSION COEFFICIENTS.....                  | 22          |
| 3.1.2.3 IONIZATION LENGTH.....                       | 27          |
| 3.1.3 DISCUSSION.....                                | 30          |
| 3.2 CASCAD STUDIES.....                              | 37          |
| 3.2.1 ANALYTICAL ESTIMATES.....                      | 37          |
| 3.2.2 CASCAD RESULTS AND DISCUSSION.....             | 47          |
| 3.3 ACORN STUDIES.....                               | 55          |
| 3.3.1 ACORN RELATED ANALYSIS AND SCALING.....        | 55          |
| 3.3.2 ACORN RESULTS AND DISCUSSION.....              | 70          |
| 4. INITIATION MECHANISMS.....                        | 84          |
| 5. QUENCHING AND BLOWOFF MECHANISMS.....             | 85          |
| 6. SUMMARY.....                                      | 98          |
| REFERENCES.....                                      | 100         |
| APPENDIX 1.....                                      | 102         |
| APPENDIX 2.....                                      | 111         |
| APPENDIX 3.....                                      | 116         |
| APPENDIX 4.....                                      | 125         |
| APPENDIX 5.....                                      | 132         |
| APPENDIX 6.....                                      | 139         |



## LIST OF APPENDICES

|   | <u>Page</u> |
|---|-------------|
| 1. Lin, D.L., Electron Multiplication in Solids, <u>Physical Review</u> , B20, 5238, 1979.  | 102         |
| 2. Lin, D.L. and Beers, B.L., Stochastic Treatment of Electron Multiplication Without Scattering in Dielectrics, <u>Journal of Applied Physics</u> , 52, 5, 3575, 1981.   | 111         |
| 3. Beers, B.L., Pine, V.W. and Ives, S.T., Theoretical Properties of Streamers in Solid Dielectrics, 1981 Annual Report, 390, <u>Conference on Electrical Insulation and Dielectric Phenomena</u> , IEEE Electrical Insulation Society, 1981. | 116         |
| 4. Beers, B.L., Pine, V.W. and Ives, S.T., Internal Breakdown of Charged Spacecraft Dielectrics, <u>IEEE Transactions on Nuclear Science</u> , NS-28, 6, 4529, 1981.  | 125         |
| 5. O'Dwyer, J.J. and Beers, B.L., Thermal Breakdown in Dielectrics, 1981 Annual Report, 193, <u>Conference on Electrical Insulation and Dielectric Phenomena</u> , IEEE Electrical Insulation Society, 1981.                                  | 132         |
| 6. O'Dwyer, J.J., Space Charge Enhanced Emission into a Dielectric Solid, paper to be published in the <u>Journal of Applied Physics</u> .  | 139         |

## 1. INTRODUCTION

The work presented herein represents the results of the first phase of activities sponsored by the NASA Lewis Research Center under Contract No. NAS 3-22530. The activities were directed to the "Continued Development of a Detailed Model of Arc Discharge Dynamics". This work is a continuation of previously documented results on the subject [Beers, et al., 1979]. The purpose of these studies is to develop a model of the catastrophic breakdown and discharge of spacecraft dielectrics which have been charged by the geosynchronous substorm plasma environment. In previous studies, a series of codes (SEMC, CASCAD, ACORN) were developed to describe the development of a single electron-initiated avalanche into a negative tip streamer. A conceptual model was also presented for a discharge mechanism which proceeds by a stochastic (random) succession of this basic process. The results presented herein are specifically directed toward a more fundamental understanding of this model. A major portion of the effort was directed towards characterizing the numerical solutions computed with the code models.

A primary goal of the studies was to explore the parameter space associated with the numerical solutions of the code models. Preparatory to initiating these parametric studies, it was necessary to modify the code packages in order to use them. The required modifications are described in Section 2. Details of these changes and a user's manual are described in a separate document entitled Operational Aspects of the Computer Codes: SEMC, CASCAD, and ACORN, Beers Associates, Inc., Report No. 1-82-16-04.

Section 3 of the report details the results of an extensive series of computations over a wide range of problem parameters. The results are presented on a code-by-code basis. In Section 3.1 the results of SEMC computations of the electron distribution function are presented.

Computational results from the CASCAD model of the undistorted avalanche are given in Section 3.2. A total of 60 separate calculations were performed for each of the above 2 sections. Section 3.3 describes the details of ACORN calculations of the evolution of the self-consistent electron avalanche. Eleven distinct computational configurations were considered here.

Section 4 gives a very brief discussion of the work on discharge initiation in space. The reader is referred to several appendices where published papers on the subject have been reproduced. The published results describe the activities performed during the contract period. Work of a more speculative nature is presented in Section 5 on discharge quenching and blow off mechanisms. The results of all work are briefly summarized in Section 6.

Six appendices to the body of the text present reproductions of published papers which were generated either directly or indirectly by the work described in this report. Appendices 1 and 2 describe semi-analytic calculations of the electron distribution function. These results support the interpretation of the SEMC results of Section 3.1. A paper describing the preliminary results of Section 3.3 is reproduced as Appendix 3. Appendix 4 gives detailed calculations supporting an internal discharge initiation mechanism which was developed. In Appendix 5, calculations of thermal breakdown in the presence of field distortion are given. Finally, further developments in the classical approach to the discharge problem are given in Appendix 6.

## 2. CODE MODIFICATIONS

An extensive set of modifications to the SEMC-CASCAD-ACORN family of computer codes previously developed has been implemented. The set of modifications may conveniently be split into two areas: upgrades to the physical models; and installation of graphics. These modifications will be discussed in the following sections on a code-by-code basis. Operational features of the updated codes are separately documented in a user's guide report. The modified codes were delivered and installed on the Lewis Research Center UNIVAC 1108 system.

### 2.1 SEMC MODIFICATIONS

Three major changes were made to the SEMC code:

- Modification of the mean free path sampling algorithm;
- Computation of an equilibrium velocity-space distribution; and,
- Automatic linkage to the CASCAD code.

These modifications are discussed in turn below.

The first change modified the mean free path sampling routine. In the usual Monte Carlo transport calculation, the energy of the particle does not change between collisions. For the required calculations however, the presence of large electric fields requires a new sampling approach.

**ORIGINAL PAGE IS  
OF POOR QUALITY**

The probability  $P(x)$  that a particle will have a collision along a path between  $x$  and  $x + dx$  is:

$$P(x)dx = \frac{1}{\lambda} \left\{ \exp \left[ - \int_0^x \frac{dx'}{\lambda} \right] \right\} dx$$

where  $\lambda$  is the mean free path. In order to sample from this distribution, we equate the probability that a random number is between  $\xi$  and  $\xi + d\xi$  (denoted  $G(\xi)d\xi$ ) to the above probability that a collision occurs between  $x$  and  $x + dx$ . By noting that  $G(\xi) = 1$  for random numbers uniformly distributed on the interval  $[0,1]$ , we obtain

$$d\xi = \frac{1}{\lambda} \left\{ \exp \left[ - \int_0^x \frac{dx'}{\lambda} \right] \right\} dx \quad . \quad (2.1.1)$$

Or by the integration

$$\int_0^\xi d\xi = \int_0^x \frac{1}{\lambda} \left\{ \exp \left[ - \int_0^x \frac{dx'}{\lambda} \right] \right\} dx \quad . \quad (2.1.2)$$

We observe however, that the integrand on the right is an exact differential and obtain:

$$\xi = 1 - \exp \left[ - \int_0^x \frac{dx'}{\lambda} \right] \quad (2.1.3)$$

or

$$\ln(1 - \xi) = - \int_0^x \frac{dx'}{\lambda} \quad . \quad (2.1.4)$$

For those situations in which the particle is in force free flight between collisions, the total macroscopic cross section  $\Sigma_t$  remains constant between collisions. The mean free path, related to the total macroscopic cross section by:

$$\lambda = \frac{1}{\Sigma_t} \quad (2.1.5)$$

is also a constant. Integration is easily performed to yield:

$$x = -\lambda \ln(1 - \xi) \quad (2.1.6)$$

Since  $1 - \xi$  has the same distribution as  $\xi$ , we have the familiar result:

$$x = -\lambda \ln \xi \quad (2.1.7)$$

In order to sample in time, one merely replaces  $x$  by  $t$  (time) and  $\lambda$  by  $\tau$  (mean free time) in the above expressions.

When there is an electric field present however, a charged particle will experience an acceleration between collisions, resulting in a constantly changing particle energy over the particle path. The mean free path (mean free time) is no longer constant in general ( $\Sigma_t$  is a function of energy) and the integration of Equation (2.1.4) depends on the form of  $\lambda$ . For a tabular form of  $\lambda(E)$ , the integration must be performed numerically. The scheme presently implemented is as follows:

- (1) Begin with a particle energy  $E_0$ .
- (2) Select a random number  $\xi'$ .
- (3) Numerically integrate  $1/\tau$  from 0 to  $t'$  until the integration is equal (to a prescribed accuracy) to  $\ln(\xi')$ .

- (4) The time to the next collision is then  $t'$ .
- (5) The coordinates of the next collision site are given by an integration of the equations of motion.

While the above discussion could easily be given in terms of distance and mean free path, the time to the next collision site must be determined from a numerical inversion of a rather complicated expression previously developed [Beers, et al., 1979]. An overall reduction in the complexity of the calculation is achieved by use of the mean free time formulation.

The second major modification was the incorporation of an algorithm for scoring the equilibrium velocity distribution  $g_0(\vec{v})$ . Scoring the equilibrium velocity distribution allows for the computation of the macroscopic transport coefficients directly from appropriate velocity space integrations. Routines for performing these computations have also been included in the code.

A method of scoring the equilibrium velocity distribution  $g_0(\vec{v})$  has been devised. An understanding of this distribution may be obtained through the following argument. One may obtain  $g_0(\vec{v})$  by visualizing a snapshot in time of the electron dynamics in phase space. The distribution  $g_0(\vec{v})$  may then be obtained by tabulating the instantaneous velocity of all particles in the snapshot. With the Monte Carlo methods however, we are able to follow only one sample particle at a time. One may view each trajectory as a contribution to the phase space snapshot by sampling the velocity of each trajectory at a single randomly selected time. By sampling a trajectory at many points in time, for example at a random time between each collision, the statistical uncertainty in the calculated value of  $g_0(\vec{v})$  for a fixed number of particle trajectories will be greatly reduced. This is the method implemented in the code.

The transport coefficients are obtained by velocity space integrations. The average velocity  $\langle \vec{v} \rangle$  is simply

$$\langle \vec{v} \rangle = \int \vec{v} g_0(\vec{v}) d\vec{v} \quad . \quad (2.1.8)$$

ORIGINAL PAGE IS  
OF POOR QUALITY

The drift velocity then, is the component of  $\langle \vec{v} \rangle$  in the direction of the field, and components perpendicular to the field should vanish with sufficiently good statistics. The mobility is obtained in the usual fashion.

Now, introduce the random velocity  $\vec{u}$  by the equation

$$\vec{v} = \langle \vec{v} \rangle + \vec{u} \quad (2.1.9)$$

The mean random energy  $T$  (mean energy minus drift energy) is given by

$$T = \int \frac{1}{2} m^* (\vec{u} \cdot \vec{u}) g_0(\vec{v}) d\vec{v} \quad (2.1.10)$$

The energy may be split into components parallel and perpendicular to the field in the obvious fashion.

The diffusion coefficients are obtained from the integrals previously derived using the Chapman-Enskog theory [Beers, et al., 1979]. Using the notation given in that reference, let  $K(\vec{v}, \vec{v}_0)$  be the scattering kernel for the Boltzmann equation. Let  $\vec{I}$  be the following vector integral:

$$\vec{I}(\vec{v}_0) = \int \vec{v} K(\vec{v}, \vec{v}_0) d\vec{v} \quad (2.1.11)$$

It follows from symmetry arguments that  $\vec{I}$  has the form

$$\vec{I}(\vec{v}_0) = \vec{v}_0 K_1(v_0^2) \quad (2.1.12)$$

where  $K_1$  is a scalar function of the variable  $(\vec{v}_0 \cdot \vec{v}_0)$ . The diffusion tensor  $\bar{D}$  may be written as the following integral:

$$\bar{D} = \int d\vec{v} \frac{g_0(\vec{v})}{K_1(v^2)} \vec{v} \vec{v} \quad (2.1.13)$$



where  $\vec{u}$  was introduced in Equation (2.1.9). The tensor  $\bar{\bar{D}}$  may be diagonalized, with diagonal components being the coefficients along the electric field and perpendicular to the electric field.

Finally, the ionization rate  $\beta$  is given by

$$\beta = \int d\vec{v} \, v_{\text{ion}}(\vec{v}) \, g_0(\vec{v}) \quad , \quad (2.1.14)$$

where  $v_{\text{ion}}(\vec{v})$  is the fundamental ionization rate for an electron with velocity  $\vec{v}$ . Routines for performing all the above integrations have been included in SEMC.

The final major modification to SEMC was the installation of an automated link between SEMC and CASCAD. The link was implemented by installing in SEMC a routine to write the distribution function of ionization sites on disk. This file is subsequently read by CASCAD with no user intervention required.

## 2.2 CASCAD MODIFICATIONS

In addition to the automated linkage described in Section 2.1, two other changes were made to CASCAD. The previous version of CASCAD was not able to follow the calculations for more than 13 generations. This limit is imposed by the amount of central memory required to store the location of each electron in the cascade. This limit was extended beyond 24 generations by the use of a dual file flip-flop buffering scheme. At the end of each generation, the locations of the electrons are stored on one disk file. These locations are then read, updated and stored on the second disk file. At the end of each generation, the read/write pointers are interchanged and the process repeated. The disk storage available was sufficient to run all cases of interest.

The final modification to CASCAD involved the installation of graphics display routines. At the end of each CASCAD run, the following four (4) plots are produced:

- charge density contour plot;
- electric potential contour plot;
- electric field magnitude contour plot; and,
- electric field vector plot.

## 2.3 ACORN MODIFICATIONS

Modifications to ACORN were made primarily in the development of a complete graphics output system and for the replacement of the routine formerly used to print the arrays. A vector plot routine was developed to provide a clear concise display of the electric field. At many points within the calculated grid an arrow is drawn. The length of the arrow is proportional to the magnitude of the electric field at that point. The direction is that of the electric field vector at that point. The routine chooses the density of arrows to be as large as possible, without producing a cluttered plot.

The contour routine developed for ACORN was designed to provide the option of either user-specified contour levels or contour levels chosen by the routine itself. Past experience has indicated that many automated graphics schemes frequently chose scaling levels which do not reasonably span the calculational regimes of interest. For this reason a more flexible scheme seemed desirable. For the ACORN results presented here, the contour levels chosen by the routine have thus far been entirely satisfactory. The routines as implemented in ACORN therefore use automated scaling as a default, with user override only when desired.

The remaining plots, such as the electron number density versus one spatial variable with the other spatial variable fixed, were also generated with a more generalized plot routine. This routine can also be used on a stand alone basis for other purposes. Again the automated scaling within this routine has proven satisfactory for the case of interest. This routine is also used to produce time history plots of the problem variables.

All three of the main plotting routines, CONTOUR, VECPLT and GRAPH were designed as general purpose stand alone routines. These routines are now available for incorporation into future codes. A complete description of how to use these graphics packages is included in the appendix of the companion operational procedures report.

### 3. COMPUTATIONAL STUDIES

An extensive series of computations was performed using the SEMC/CASCAD/ACORN family of codes. The computations were performed on site at LEWIS RESEARCH CENTER. These computations are discussed on a code-by-code basis in the following text.

#### 3.1 SEMC STUDIES

The computer code SEMC solves the linear Boltzmann transport equation for the electron distribution function in the presence of an applied electric field. No electron self-scattering effects are included in the simulation. The electrons undergo collisional events with a background set of scattering centers. A specification of the scattering events determines a model for the electron interaction with the background material.

A crude model which was developed earlier [Beers, et al., 1979] represents the interaction of conduction band (quasi-free) electrons in a solid material representing Teflon. It was the purpose of the SEMC computational studies to explore the dependence of the electron distribution function (and resulting transport coefficients) on the parameters which define the scattering model. As all subsequent calculations in the CASCAD/ACORN series depend on the coefficients determined from the SEMC calculations, a determination of the sensitivity of these parameters on the material model also provides information for subsequent CASCAD/ACORN calculations.

The choice of scattering models for the SEMC computations, results the subsequent calculations, and a discussion of these results are presented below.

### 3.1.1 SCATTERING PARAMETER FORMULATION: SCALING

As currently formulated, the single scattering Monte Carlo Code SEMC requires the definition of three distinct processes: elastic scattering, inelastic energy loss (non-ionizing), and ionization. The scale for these processes is set by some overall dimensional quantity having units of length (i.e., mean free path). Thus, the input depends on three dimensional parameters  $\lambda_{el}$ ,  $\lambda_0$ ,  $\lambda_I$  where the  $\lambda$ 's are the mean free paths for the respective processes. In addition, the inelastic and ionization processes are characterized by their energy thresholds (denoted  $\hbar\omega$  and  $E_I$  respectively). These two dimensional parameters characterize the energy loss of the electron. The only other dimensional parameters available are the electronic effective mass  $m^*$ , the electronic charge  $e$ , and the electric field  $F$ . One might also introduce the density of the solid  $N$ . Within the present formulation however, it will be assumed that  $N$  only enters the problem through the mean free paths (MFP), with all MFP's scaling inversely with density.

From this list of eight dimensional variables  $\lambda_{el}$ ,  $\lambda_0$ ,  $\lambda_I$ ,  $E_I$ ,  $\hbar\omega$ ,  $m^*$ ,  $e$  and  $F$ , three independent variables may be chosen to represent the fundamental units of mass, length, and time. All other dimensional variables may then be expressed in terms of this basic set. A convenient choice is the electronic effective mass  $m^*$ , the elastic mean free path  $\lambda_{el}$ , and the ionization energy  $E_I$  (a quantity conjugate to time). Denoting the fundamental dimensional units by a subscript "naught", we then have the following expressions for the units of mass, length, time, velocity, force and energy:

ORIGINAL PAGE IS  
OF POOR QUALITY

$$M_0 = m^* \quad , \quad (3.1.1)$$

$$L_0 = \lambda_{el} \quad , \quad (3.1.2)$$

$$T_0 = \sqrt{\frac{m^*}{2E_I}} \lambda_{el} \quad , \quad (3.1.3)$$

$$V_0 = \sqrt{\frac{2E_I}{m^*}} \quad , \quad (3.1.4)$$

$$\mathcal{F}_0 = \frac{E_I}{\lambda_{el}} \quad , \quad \text{and} \quad (3.1.5)$$

$$E_0 = E_I \quad . \quad (3.1.6)$$

All other dimensional quantities may be expressed in terms of the fundamental units of mass, length and time. For example, the units of the diffusion coefficient  $D_0(L_0^2 T_0^{-1})$  are

$$D_0 = \sqrt{\frac{2E_I}{m^*}} \lambda_{el} \quad . \quad (3.1.7)$$

(It is implicitly assumed that the temperature of the lattice is fixed in the above discussion, and that the temperature dependence of the solution enters only through the parameters already given).

The remaining problem variables may be expressed in terms of the three basic variables, together with dimensionless parameters formed from various combinations of the problem variables. A convenient set of dimensionless parameters is:

$$\Lambda_I = \frac{\lambda_I}{\lambda_{el}} , \quad (3.1.8)$$

$$\Lambda_0 = \frac{\lambda_0}{\lambda_{el}} , \quad (3.1.9)$$

$$R = \frac{\hbar\omega}{E_I} , \quad (3.1.10)$$

$$X = \frac{E_I}{eF\lambda_{el}} , \quad \text{and} \quad (3.1.11)$$

$$\Omega = \frac{e}{F\lambda_{el}^2} . \quad (3.1.12)$$

where  $\Lambda_I$  and  $\Lambda_0$  are the length ratios and  $R$ ,  $X$ , and  $\Omega$  are energy ratios. The quantity  $X$  is the ratio of ionization energy to energy gained in an elastic mean free path, while  $\Omega$  is the ratio of electrostatic Coulomb energy in a mean free path to the energy gain in a mean free path. The two quantities  $e$  and  $F$  enter the linear Boltzmann equation as a product  $e \cdot F$  (in the external force term). Dimensional analysis of this equation gives rise to quantities which depend on this product, rather than on  $e$  and  $F$  individually. It follows that the equation, and hence the solution, is independent of the variable  $\Omega$  because  $\Omega$  varies as the ratio of  $e$  and  $F$ . The variable  $\Omega$  enters only when the electron can act on itself (i.e., in collective problems).

With the above information, it is an elementary task to rewrite all the problem variables in terms of the three dimensional variables, and the four dimensionless parameters  $\Lambda_I$ ,  $\Lambda_0$ ,  $R$  and  $X$ . Distinct problems (not obtainable by scaling) are therefore specified by the four dimensionless variables noted above. Of these, only the quantity  $X$  depends on the external field strength, so that  $X$  may be chosen as the variable specifying field strength. The remaining three parameters  $\Lambda_I$ ,  $\Lambda_0$ , and  $R$  characterize the scattering parameter set.

For the purposes of this investigation, we will now suppress one of these variables ( $\Lambda_I$ ). Shown in Figure 3.1.1 is a typical ionization cross-section (determining  $\lambda_I$ ). The major feature to note is that the cross-section rises very sharply out of threshold, reaches a peak substantially above threshold, and then begins to trail off slowly for higher energies. For solid densities, cross-sections with this order of magnitude correspond to rather short mean free paths (a few Ångströms). Except for enormous fields (greater than  $10^{10}$  V/M), the energy gained in an ionization mean free path is completely negligible compared to the energy required to pass the peak in the cross-section. For moderate fields the electron will lose essentially all of its energy in the collision ionization. This implies that the results will be very insensitive to the exact value of the cross-section above threshold. In conformity with all other investigators, we will make the assumption that this parameter is not of concern for the field strengths of interest here; only if a study of runaway electrons were required would it make sense to investigate this parameter. For solids these runaways occur at field strengths substantially higher than those of interest.

The parameter variations for the present study are those involving  $R$  and  $\Lambda_0$ . For the model of Teflon chosen during the first phase of this work [Beers, et al., 1979], the optical phonon energy  $\hbar\omega$  was taken to be 0.11 eV, while the band gap  $E_I$  was taken as 6.5 eV to a corresponding  $R$ -value of 0.017. Reasonable band gaps for insulators may be chosen in the range from 2 to 10 eV. Optical phonon energies in polymer type materials typically vary in the range of 0.04 to 0.4 eV. This range of energy values produces a spread of  $R$ -values from 0.004 to 0.2. We have chosen three  $R$ -values to span this range [0.2, 0.03, 0.004]; other values may be interpolated as required. The dependence of ionization on this parameter may be partially understood from the literature and is discussed in Section 3.1.3 below.

In the Teflon Model previously investigated the quantity  $\Lambda_0$  had a value of 4.4. Because cross-sections in polymers do not vary widely, it is unlikely that this quantity will vary by more than a factor of 5 from this nominal value. We therefore choose the values of  $\Lambda_0$  to be [1, 5, 25].



ORIGINAL PAGE IS  
OF POOR QUALITY

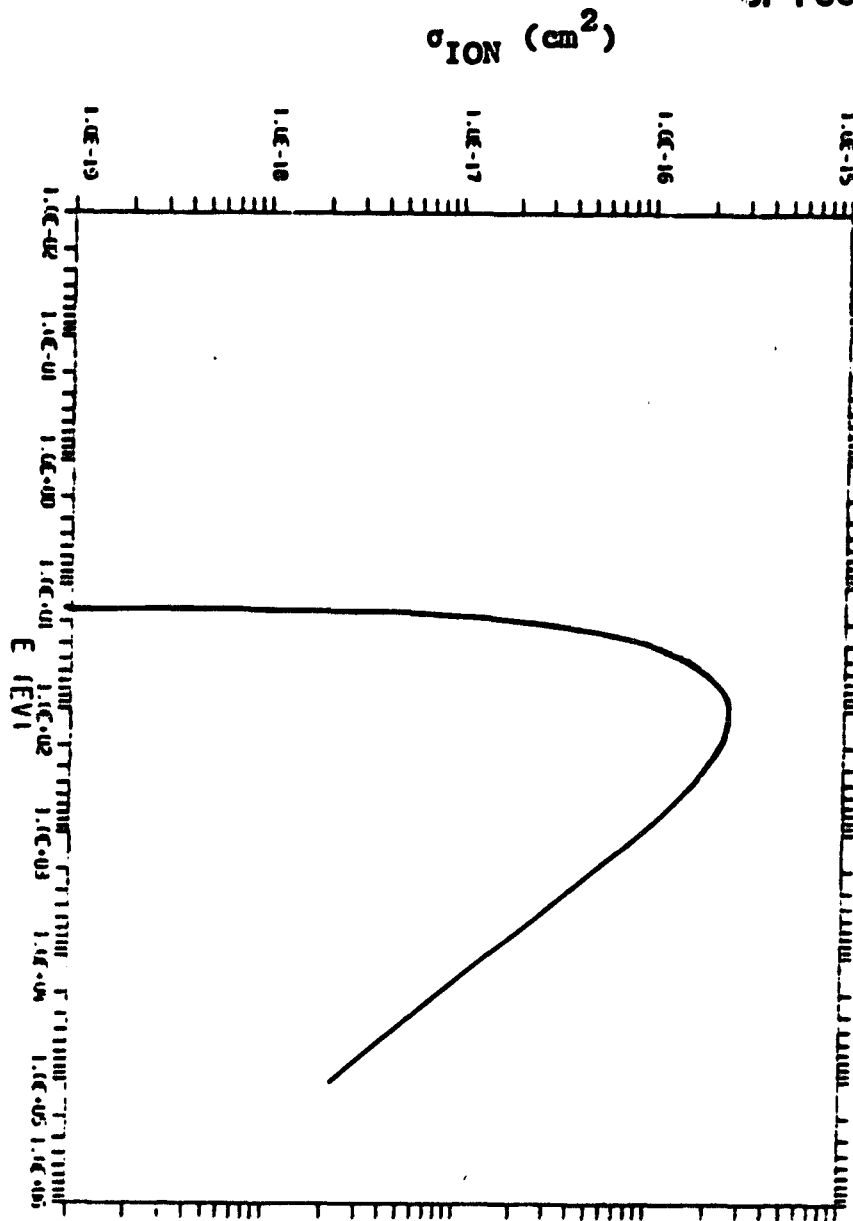


Figure 3.1.1 Total Ionization Cross Section in  $\text{N}_2$ ;  
From [Strickland, et al., 1976].

ORIGINAL PAGE IS  
OF POOR QUALITY

All combinations of the above parameters give rise to nine different cross-section sets. Because the code SEHC requires dimensional inputs, the fundamental units must be given specific values, and the actual parameters determining  $R$  and  $\Lambda_0$  must be given their appropriate values. Specifically the quantities  $\lambda_{e\ell}$ ,  $E_I$ , and  $m^*$  have the same values as in the previous study, whereas  $\hbar\omega$  and  $\lambda_0$  are varied to give the required variations in  $R$  and  $\Lambda_0$ . Also, the ionization mean path retains the same value as previously. The fixed parameters are:

$$\begin{aligned}\lambda_{e\ell} &= 6 \times 10^{-10} \text{ m} \quad , \\ \lambda_I &= 2 \times 10^{-10} \text{ m} \quad , \\ E_I &= 6.5 \text{ eV} \quad ,\end{aligned}\tag{3.1.13}$$

and last, the electronic mass (chosen as the bare electron mass).

Table 3.1.1 defines the variations of  $\hbar\omega$  and  $\lambda_0$  used to define a material model (cross-section set). Each set is given a numerical label from 1 to 9, spanning the range of  $R$ ,  $\Lambda_0$  discussed above. In addition, a 10th model is included in the table representing the nominal model developed in the previous study. [Beers, et al., 1979].

The field values chosen for the computations were all at the high end of the physical scale. Based on general theoretical considerations (see Section 3.1.3 below), the high field results may readily be extrapolated to lower field values. Six field values were chosen, spanning a single decade of field strength. These values were  $[4 \times 10^9, 2 \times 10^9, 8 \times 10^8, 6 \times 10^8, 4 \times 10^8]$ , where the quantities in brackets are in volts per meter. These field values correspond to values of the dimensionless variable  $X$  of  $[2.7, 5.4, 10.8, 13.5, 18.1, 27.1]$ .

ORIGINAL PAGE IS  
OF POOR QUALITY

| MODEL<br>NUMBER | OPTICAL<br>PHONON<br>ENERGY<br>(eV) | R     | OPTICAL<br>PHONON<br>MFP<br>°<br>Å | $\Lambda_0$ |
|-----------------|-------------------------------------|-------|------------------------------------|-------------|
| 1               | 1.300                               | 0.200 | 6                                  | 1           |
| 2               | 0.195                               | 0.030 | 6                                  | 1           |
| 3               | 0.026                               | 0.004 | 6                                  | 1           |
| 4               | 1.300                               | 0.200 | 30                                 | 5           |
| 5               | 0.195                               | 0.030 | 30                                 | 5           |
| 6               | 0.026                               | 0.004 | 30                                 | 5           |
| 7               | 1.300                               | 0.200 | 150                                | 25          |
| 8               | 0.195                               | 0.030 | 150                                | 25          |
| 9               | 0.026                               | 0.004 | 150                                | 25          |
| 10              | 0.110                               | 0.017 | 26                                 | 4.3         |

Table 3.1.1

Definition of Material Models by Parameters R,  $\Lambda_0$

### 3.1.2 SEMC RESULTS

The updated version of SEMC was exercised on the ten models of Table 3.1.1. Each material model was run for the six field levels discussed in Section 3.1.1, for a total of 60 distinct computations. The results are summarized below.

#### 3.1.2.1 MOBILITY

Shown in Figure 3.1.2 is the mobility for three different models (3, 6, 9). Each of these models has a fixed value of the optical phonon energy. The mean free path for optical phonon emission increases with increasing model number. Thus, we see that an increase in optical phonon MFP leads to a decrease in mobility, but that the absolute mobility is relatively insensitive to this parameter. Each of the other sets (for constant R) shows the same behavior.

Shown in Figure 3.1.3 is the mobility for three models (4, 5, 6) which have a fixed value of  $\Lambda_0$ . In this case the optical phonon energy decreases with increasing model number. The dependence on optical phonon energy and field level is somewhat more complicated, as evidenced by the cross-over in the curves. In absolute terms however, the mobility is very insensitive to this parameter. Other sets with fixed  $\Lambda_0$  show similar behavior.

It may be concluded that the mobility is very insensitive to the value of  $\hbar\omega$  and only slightly sensitive to the value of  $\lambda_0$ . The mobility does however, show a strong dependence on the value of the electric field, varying by a factor of 5 over a decade of field strength.

ORIGINAL PAGE IS  
OF POOR QUALITY

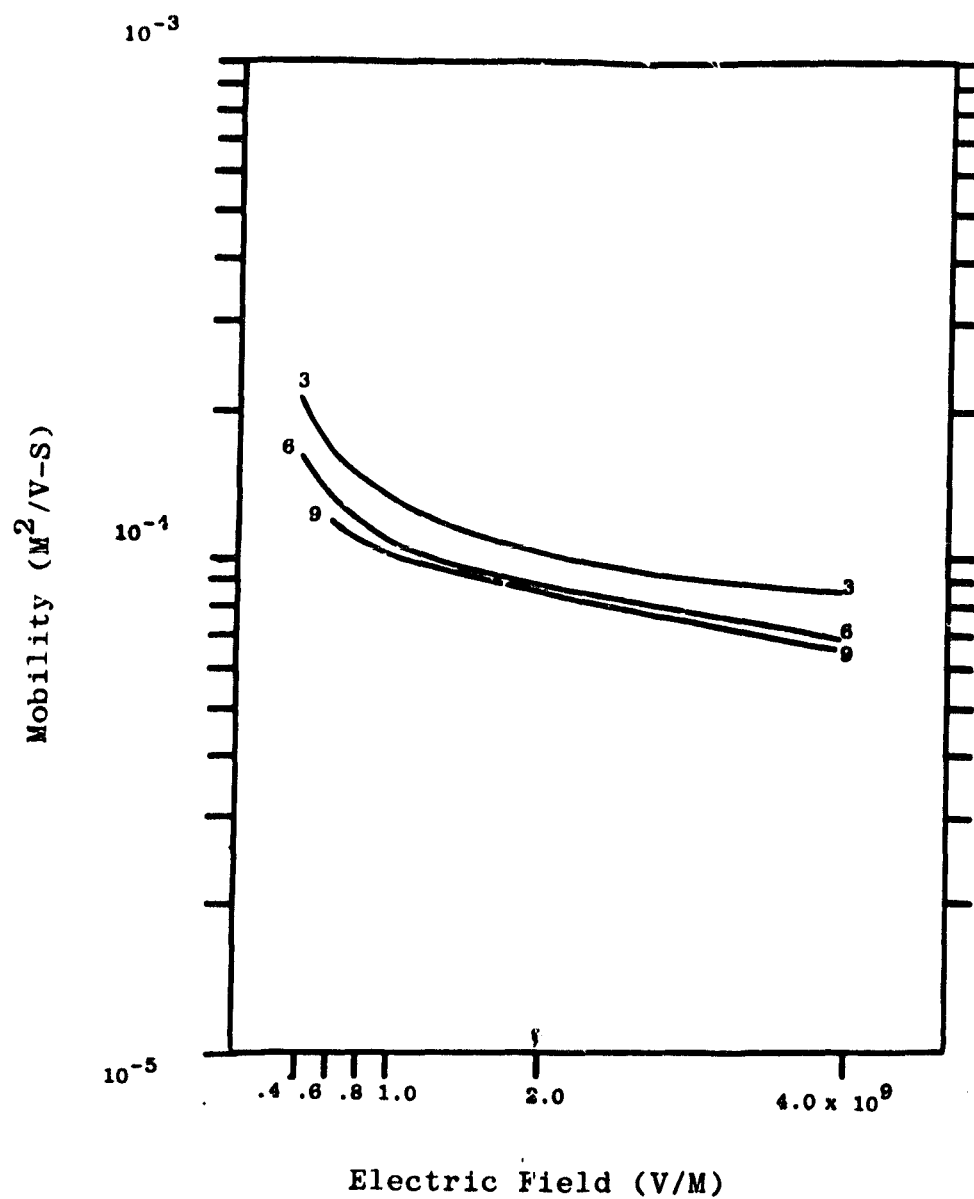


Figure 3.1.2 Mobility Versus Electric Field for Three Scattering Sets, With Fixed R.

ORIGINAL PAGE IS  
OF POOR QUALITY

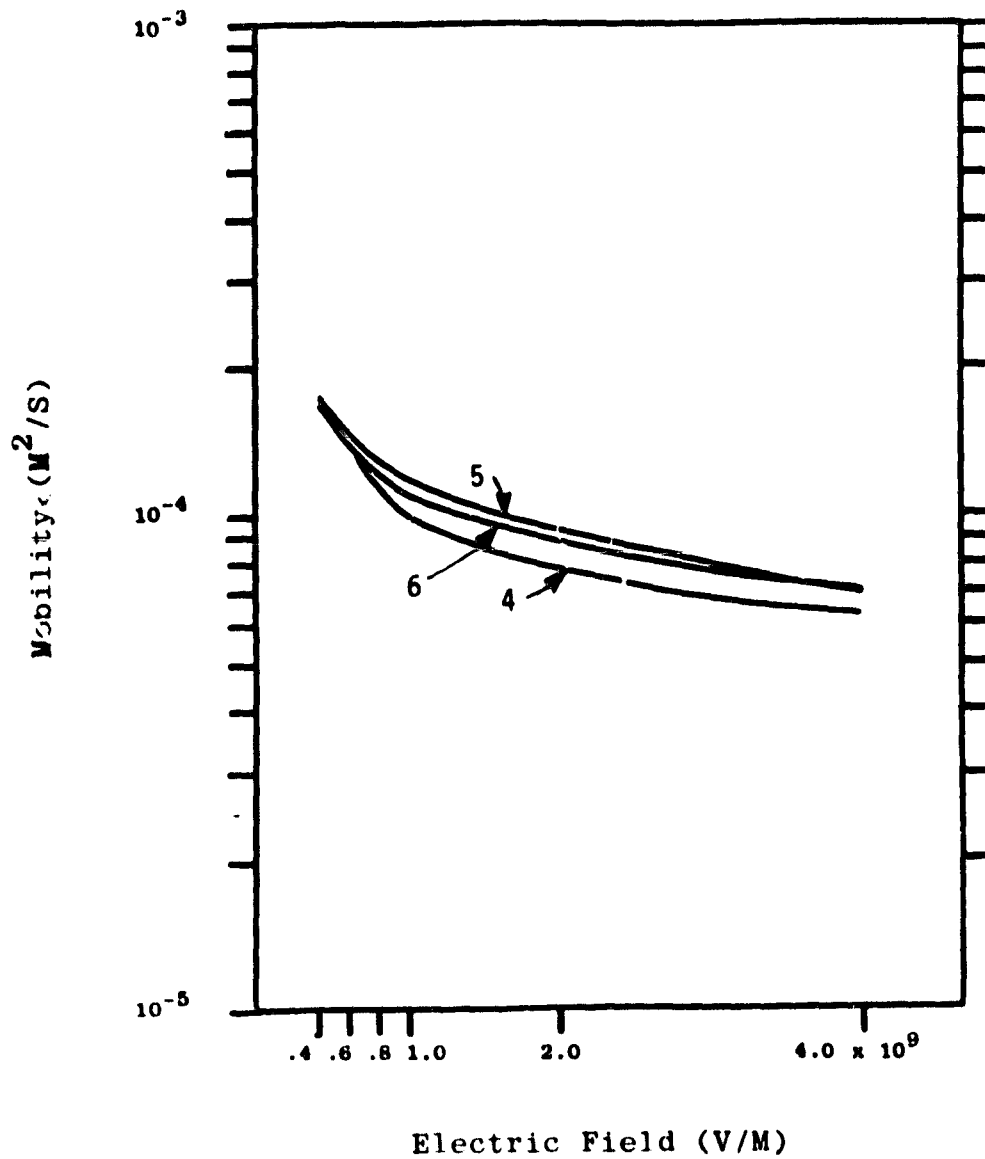


Figure 3.1.3 Mobility Versus Electric Field for Three Scattering Sets with Fixed  $\Lambda_0$ .

### 3.1.2.2 DIFFUSION COEFFICIENTS

Shown in Figure 3.1.4 is the transverse diffusion coefficient for three scattering sets with fixed  $R$ . Increasing the optical phonon MFP corresponds to an increasing scattering set number. We also see that an increase in the optical phonon MFP leads to an increase in the diffusion coefficient and that the absolute change is small. Other groups of scattering sets with fixed  $R$  show similar variation. Illustrated in Figure 3.1.5 is the transverse diffusion coefficient for three scattering sets having fixed  $\Lambda_0$ . Increasing set numbers correspond to decreasing optical phonon energy. The dependence on this parameter (optical phonon energy) is much stronger, with variations of nearly 50% between sets 4 and 5. The relationship is also not monotonic as is evidenced by the shuffled order and the apparent crossing at low fields. The other sets (for fixed  $\Lambda_0$ ) show the same ordering with respect to  $\hbar\omega$ . The field dependence of the transverse diffusion coefficient is quite weak. (The scale on the figure is linear and exaggerates the variation of this quantity).

Shown in Figure 3.1.6, family (3, 6, 9) represents the longitudinal diffusion coefficient for three scattering sets which have the same value of  $R$ . For small values of the field, an increase in  $\lambda_0$  results in an increase in diffusion. For high values of the field, this ordering is not present. A cross-over point is evident and the dependence on  $\lambda_0$  is quite weak. The cross-section family (2, 5, 8) shows similar behavior, but the family (1, 4, 7) is different in that there is a uniform increase in diffusion for increasing  $\lambda_0$ . It appears that the cross-over point may be at much higher fields. All the families show a similar weak variation as a function of  $\lambda_0$ .

Shown in Figure 3.1.7 is the longitudinal diffusion coefficient for variations in  $\hbar\omega$ , with  $\lambda_0$  fixed. Both the longitudinal diffusion coefficient and the transverse coefficient demonstrate an identical behavior with  $\hbar\omega$ . Other families show the same behavior as well.

ORIGINAL PAGE IS  
OF POOR QUALITY

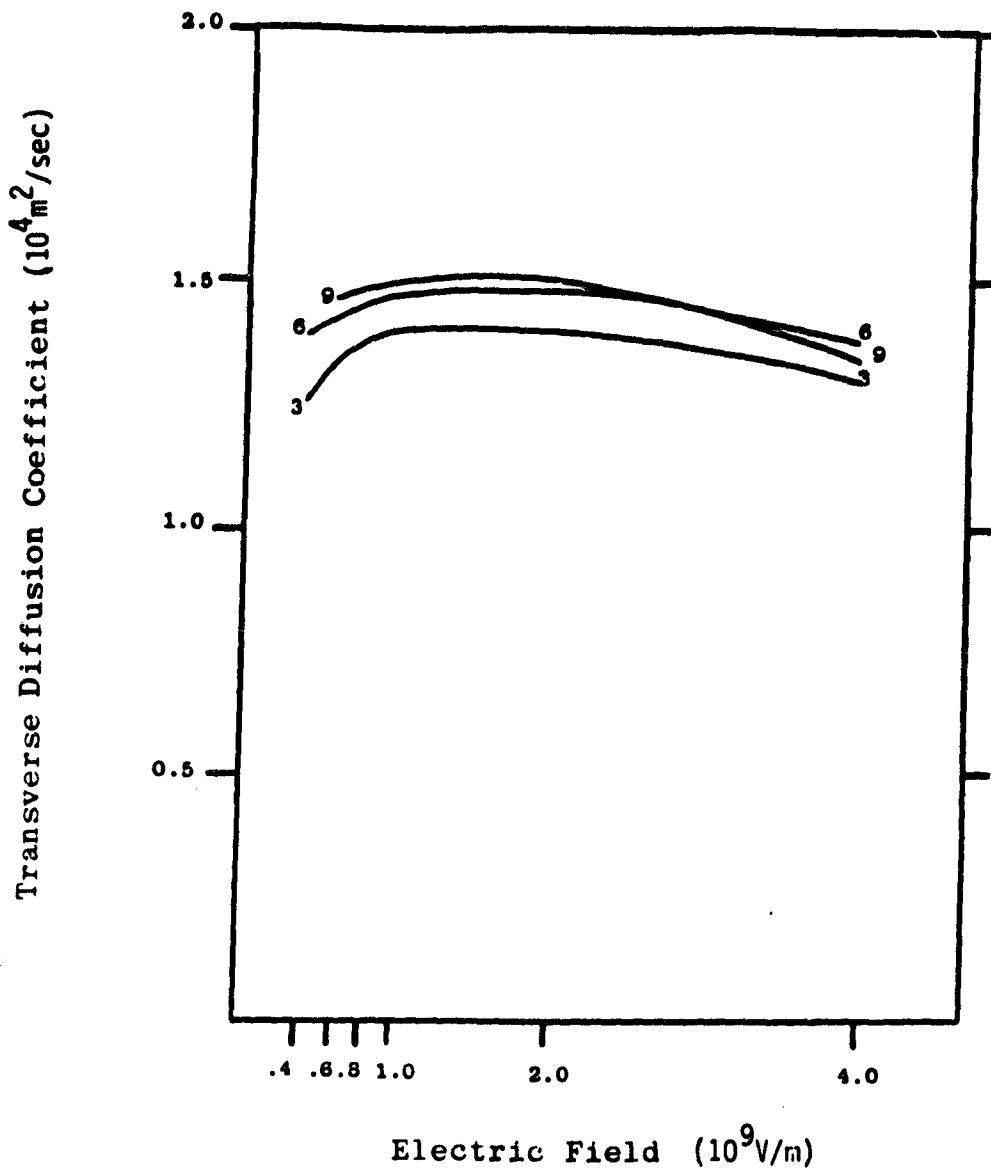


Figure 3.1.4 Transverse Diffusion Coefficient Versus Electric Field for Three Scattering Sets With Fixed R.



ORIGINAL PAGE IS  
OF POOR QUALITY

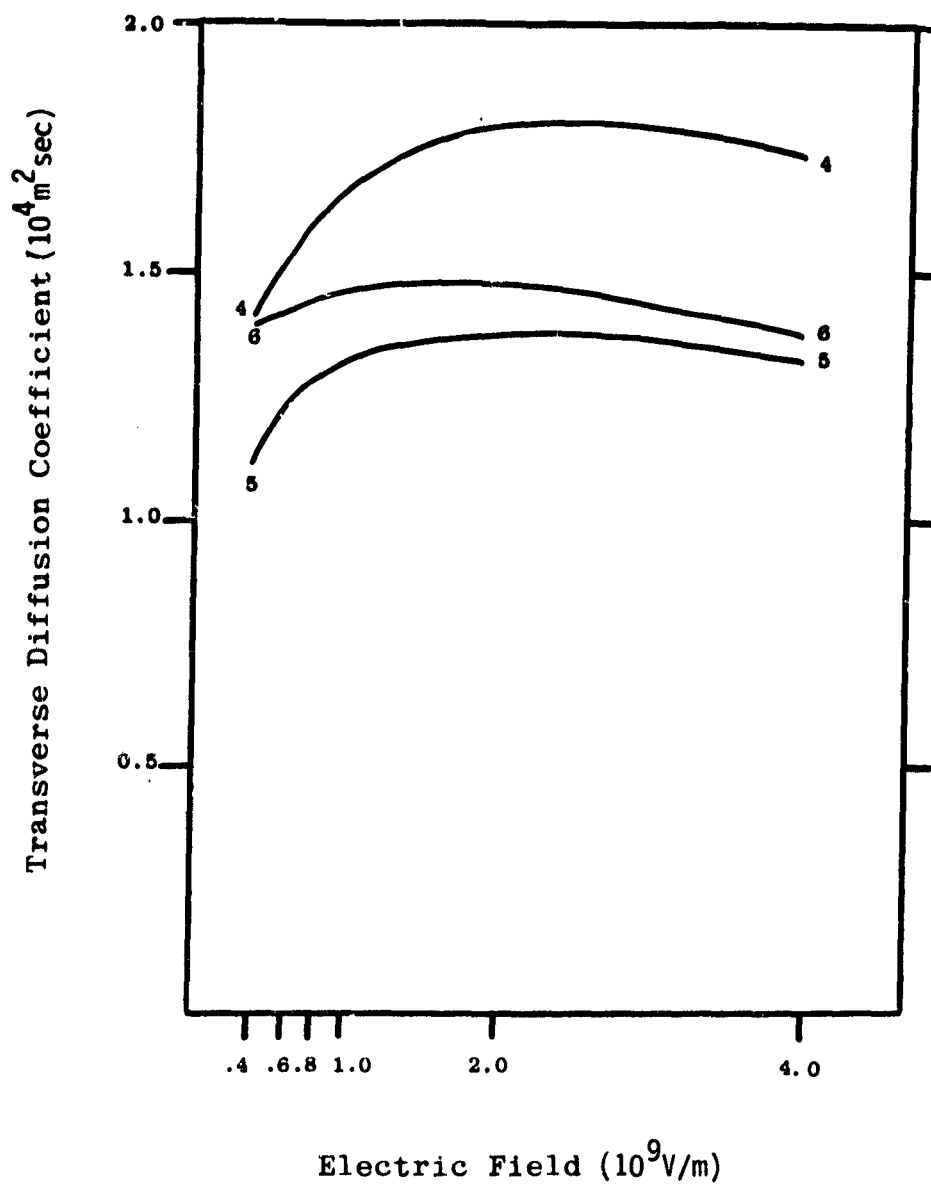


Figure 3.1.5 Transverse Diffusion Coefficient  
Versus Electric Field for Three  
Scattering Sets With Fixed  $\Lambda_0$ .

ORIGINAL PAGE IS  
OF POOR QUALITY

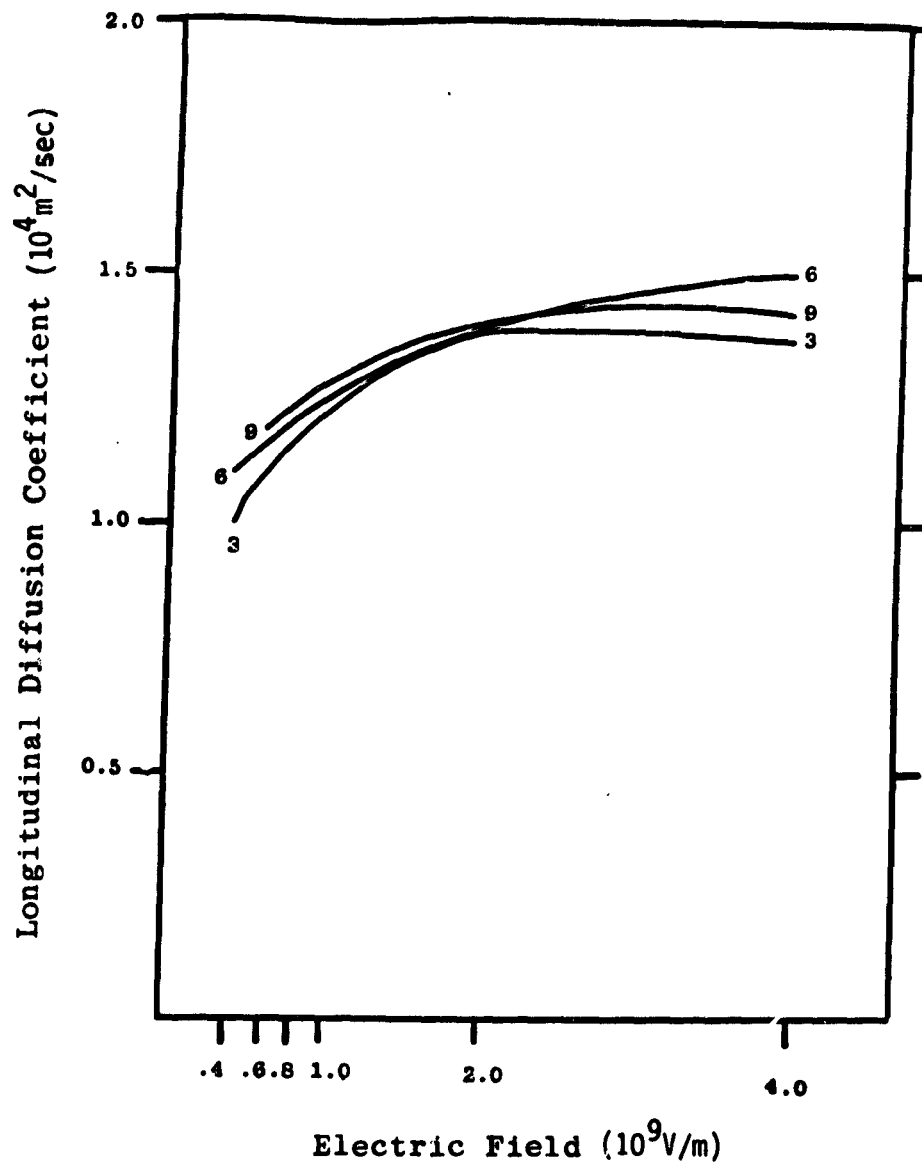


Figure 3.1.6 Longitudinal Diffusion Coefficient Versus  
Electric Field for Three Scattering Sets  
With Fixed R.

ORIGINAL PAGE IS  
OF POOR QUALITY

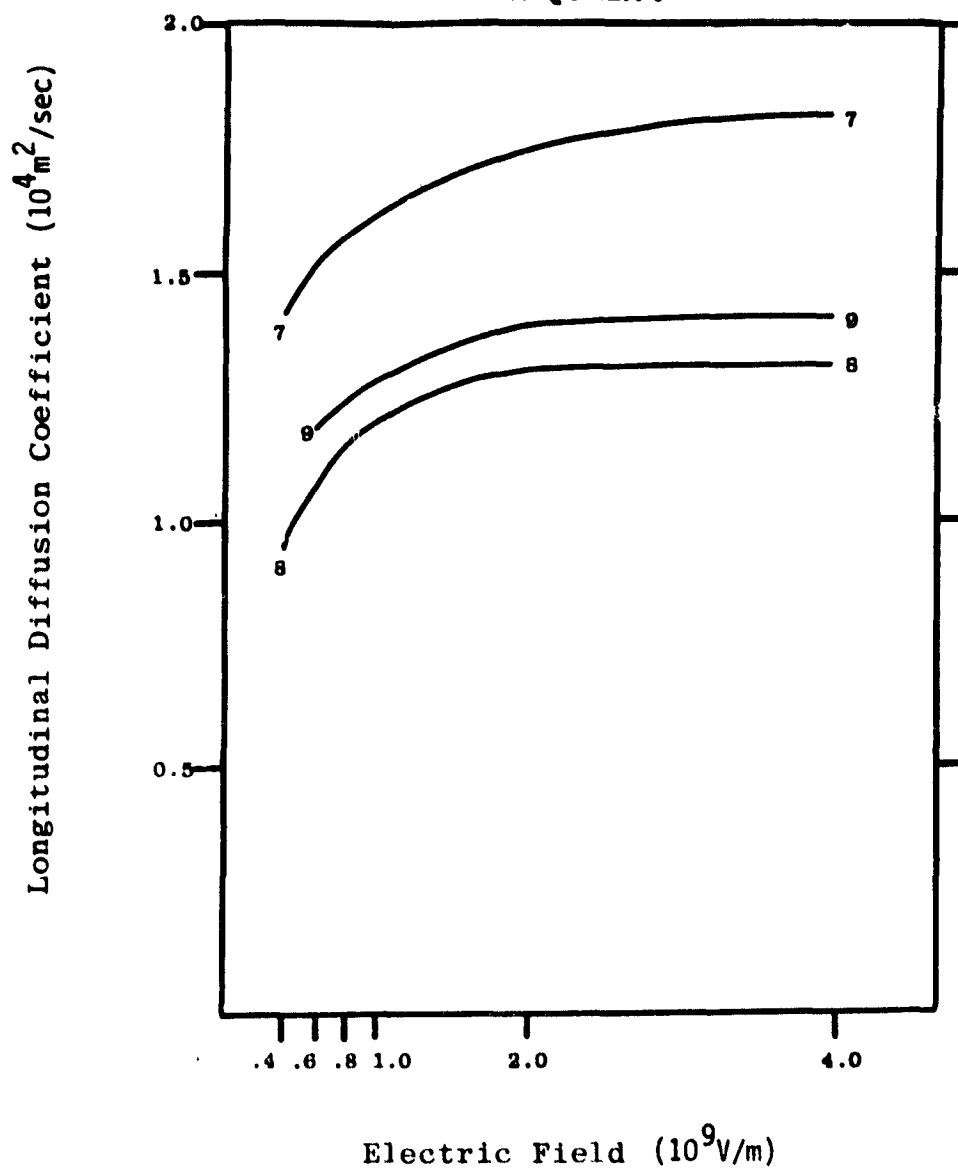


Figure 3.1.7 Longitudinal Diffusion Coefficient Versus Electric Field for Three Scattering Sets With Fixed  $\Lambda_0$ .

The variation in the longitudinal diffusion coefficient with field is comparable to the variation of the transverse coefficient, varying by less than a factor of 2 over a decade of field strength.

### 3.1.2.3 IONIZATION LENGTH

Shown in Figure 3.1.8 is the ionization length versus electric field for three scattering sets having a fixed value of  $\hbar\omega$ . For low values of the field, an increase in the optical phonon MFP leads to a decrease in the ionization length. For higher fields, this rather sharp difference decreases and the curves coalesce, cross, and the dependence on  $\lambda_0$  inverts, but is much weaker. Other families of scattering sets show a similar behavior.

Shown in Figure 3.1.9 is the ionization length for three scattering sets with fixed  $\lambda_0$  and different values of  $\hbar\omega$ . An increase in optical phonon energy at low fields gives rise to a strong increase in ionization length. At high fields there is a coalescence of the curves, showing a strong suppression of the dependence on this parameter. Other families for fixed  $\lambda_0$  show similar behavior.

The most remarkable feature is the very strong dependence on electric field, with variation of more than a factor of 200 over one decade of field strength. Because this is the quantity most sensitive to field strength, a compilation of all the computed ionization lengths is given in Figure 3.1.10.

ORIGINAL PAGE IS  
OF POOR QUALITY

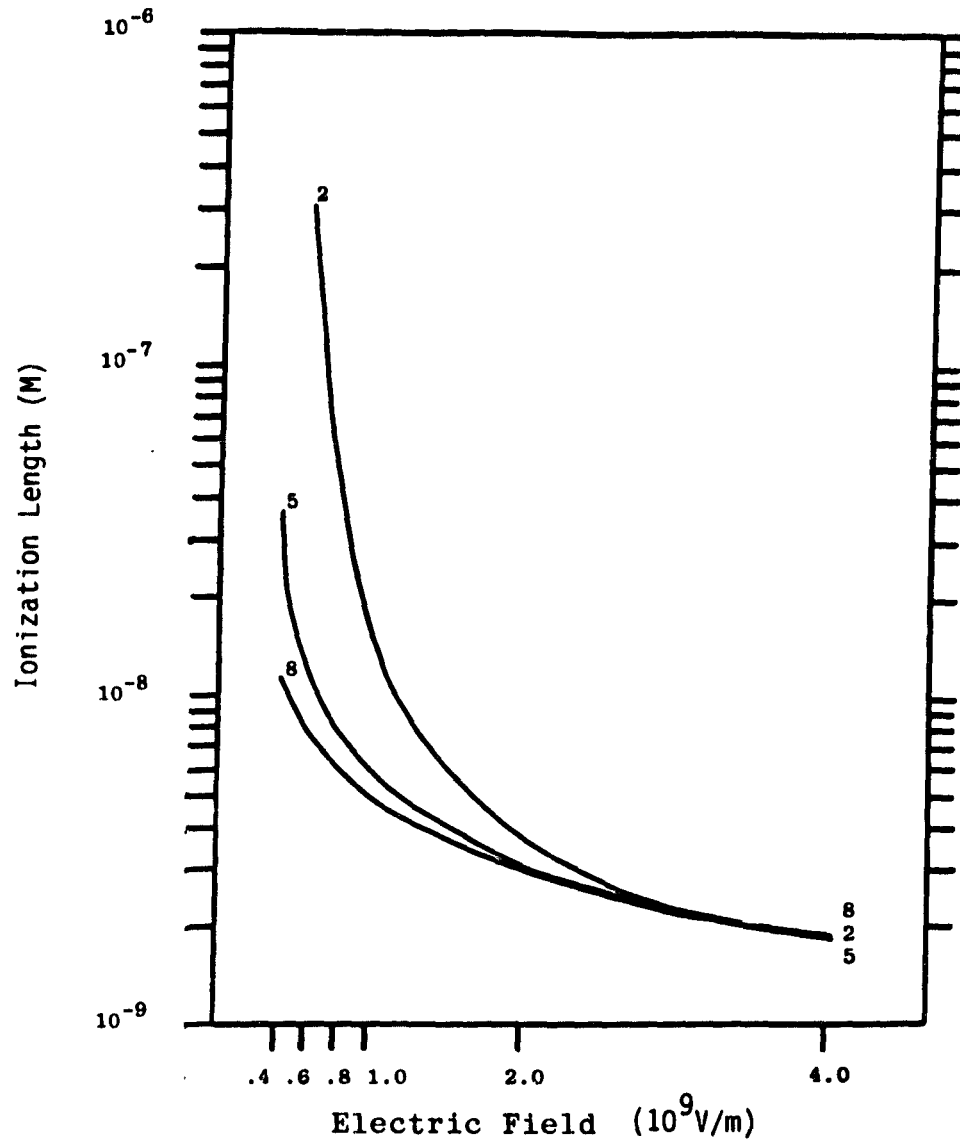


Figure 3.1.8 Ionization Length Versus Electric Field  
for Three Scattering Sets With Fixed R.

ORIGINAL PAGE IS  
OF POOR QUALITY

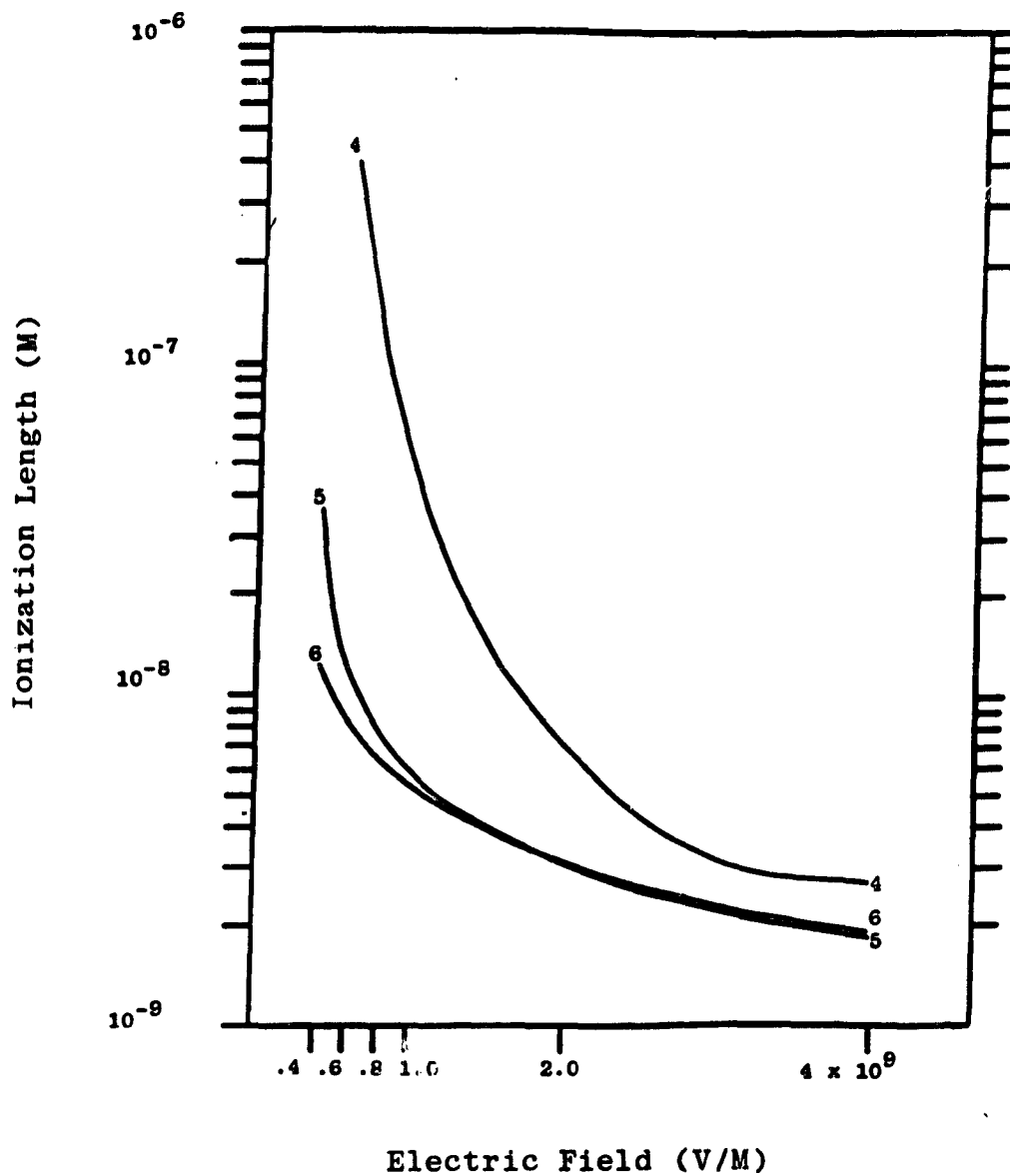


Figure 3.1.9 Ionization Length Versus Electric Field for Three Scattering Sites With Fixed  $\Lambda_0$ .

ORIGINAL PAGE IS  
OF POOR QUALITY

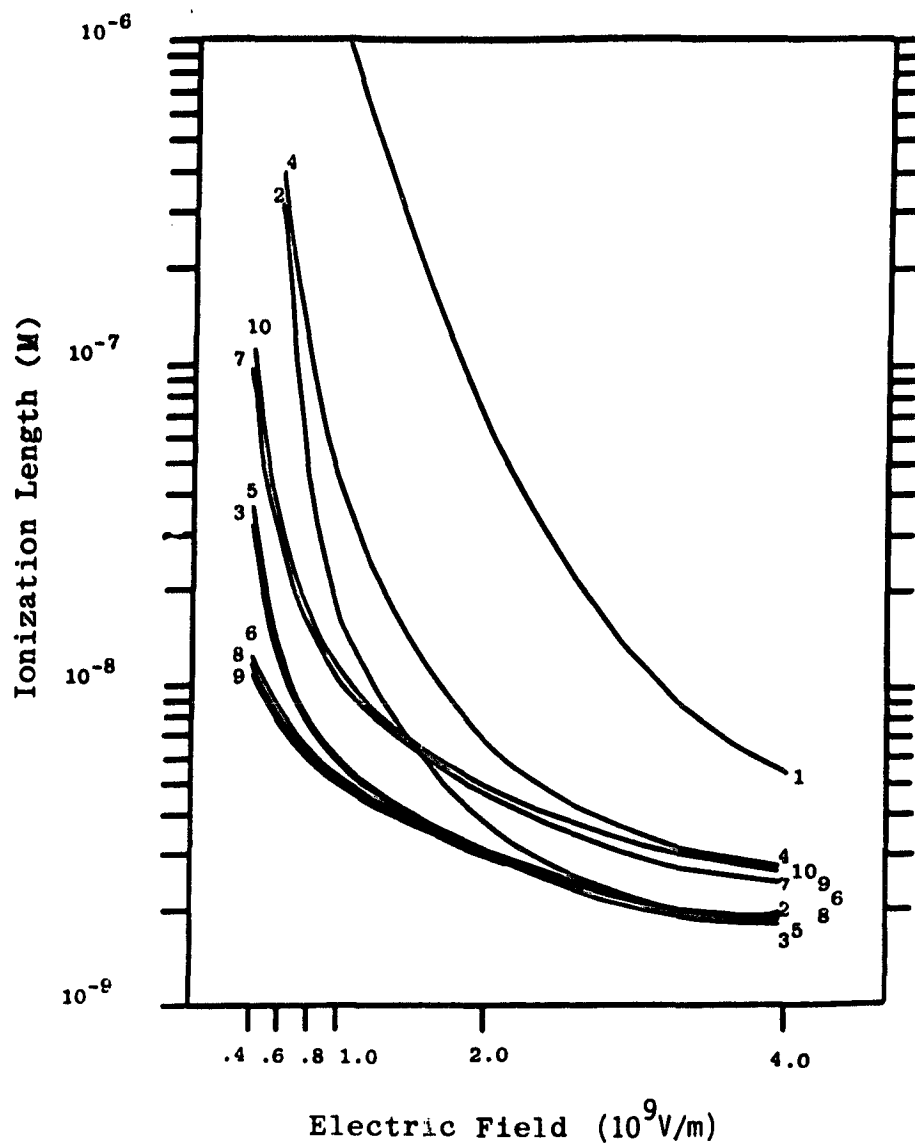


Figure 3.1.10 Ionization Length vs Electric Field for the  
Models of Table 3.1.1.

### 3.1.3 DISCUSSION

A momentum transfer collision rate  $\nu_D$  is related to the mobility  $\mu$  by the relation

$$\mu = \frac{e}{m^* \nu_D} \quad . \quad (3.1.14)$$

The rate  $\nu_D$  is related to the mean free path for momentum transfer  $\lambda_D$ , and the mean speed  $\bar{v}$  by the usual relation

$$\nu_D = \frac{\bar{v}}{\lambda_D} \quad . \quad (3.1.15)$$

Because the inelastic processes do not lead to any net momentum transfer on the average, the quantity  $\lambda_D$  is equal to  $\lambda_{el}$  (a constant). Thus, all the dependence of  $\mu$  on the model (and field) is through the mean speed  $\bar{v}$ . As the field increases and the electrons heat up, with a consequent rise in  $\bar{v}$ , the mobility decreases as seen in the calculated results. Equation (3.1.15) is implicit, because the mean speed includes a contribution due to the drift velocity  $v_D$ . Using the random velocity  $\vec{u}$  (with magnitude  $u$ ) defined in Equation (2.1.9), we have the obvious relation

$$\bar{v}^2 = v_D^2 + u^2 \quad . \quad (3.1.16)$$

Combining relations (3.1.14-3.1.16) together with the relation of drift velocity and mobility, the resulting equation may be solved for  $\nu_D$ . The following result is found



$$v_D = \left\{ \sqrt{\frac{1}{2} \left( \sqrt{1 + 4Y^2} - 1 \right)} \right\} u \quad (3.1.17)$$

$$\equiv (f(Y)u)$$

where

$$Y = \frac{e F \lambda_{e\ell}}{2 \left( \frac{1}{2} m^* u^2 \right)} \quad (3.1.18)$$

Equation (3.1.17) displays explicitly the dependence of the drift velocity on the mean random energy of the electrons. Combining Equation (3.1.17) with the definition of mobility gives

$$\mu(F) = \frac{f(Y)}{Y} \mu(0) \quad , \quad (3.1.19)$$

where  $f(Y)$  is defined in Equation (3.1.17) and  $\mu(0)$  is given by

$$\mu(0) = \frac{e \lambda_{e\ell}}{m^* u} \quad (3.1.20)$$

Equation (3.1.19) is a useful form for the mobility. The quantity  $\mu(0)$  has the dimensions of  $\mu$ , reduces to the zero field mobility at  $F = 0$ , and is a relatively weak function of the electric field. Most of the variation of the mobility due to the field is contained in the dimensionless function  $f(Y)/Y$ , which varies with the dimensionless quantity  $Y$ . The variable  $Y$  is directly proportional to the field  $F$  and inversely proportional to the random energy of an electron  $(\frac{1}{2} m^* u^2)$ . Shown in Figure 3.1.11 is the random energy of the electron for the various models computed above. While the energy varies strongly with electric field, it does not vary too strongly from model to model.

ORIGINAL PAGE IS  
OF POOR QUALITY

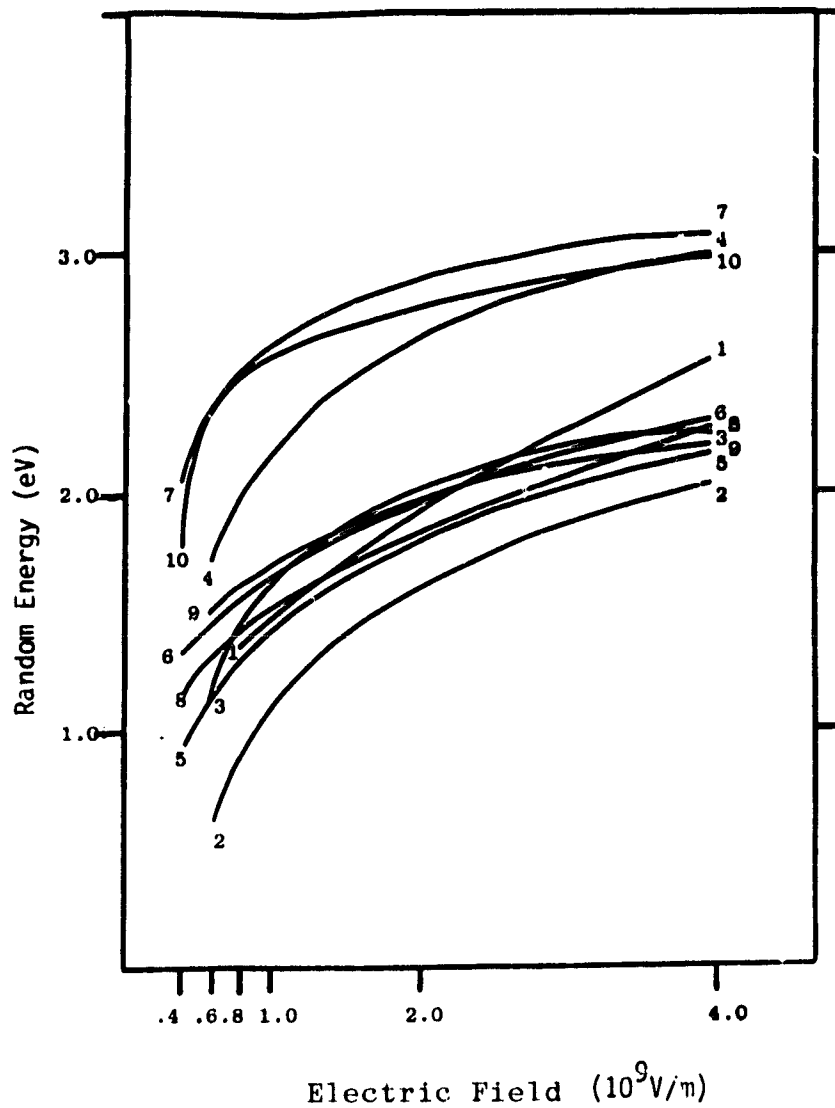


Figure 3.1.11 Random Energy Versus Field Strength  
for Various Scattering Models.

**ORIGINAL PAGE 18  
OF POOR QUALITY**

It is possible to feel comfortable with the relative insensitivity of mobility results to the material parameters together with the relatively strong dependence on field. Scattering is dominated by the elastic process. The drift velocity must saturate at high fields. For the ACORN computations of Section 3.3, we will assume a single fit to the mobility of all models, an excellent assumption based on the computed results.

In elementary kinetic theory, the diffusion coefficient  $D$  is related to the average energy and the collision frequency  $\nu$  for randomizing collisions,

$$D \approx \frac{1}{3} \frac{\langle v^2 \rangle}{\nu} \quad . \quad (3.1.21)$$

Equating  $\langle v^2 \rangle$  with  $\bar{v}^2$  and assuming that only the elastic collisions are randomizing, we find

$$D \approx \frac{1}{3} \bar{v} \lambda_{el} \quad . \quad (3.1.22)$$

The dependence of  $D$  on  $\bar{v}$  given by Equation (3.1.22) shows that heating of the electrons will lead to an increase in  $D$ . This expression may be rewritten in terms of  $u$ , to yield

$$D = \frac{1}{3} u \lambda_{el} \sqrt{\frac{1}{2} \left( 1 + \sqrt{1 + 4Y^2} \right)} \quad . \quad (3.1.23)$$

The explicit dependence of  $D$  on the field is contained in the quantity under the radical, while the dimensional dependence is contained in the factor outside the radical.

**ORIGINAL PAGE IS  
OF POOR QUALITY**

Although the quantity  $Y$  varies relatively rapidly as a function of the field, the quantity under the radical is a very weak function of  $Y$  for the range of values taken on by  $Y$ . In a first approximation, the dependence on the field may therefore be suppressed. As displayed by Figure 3.1.11,  $D$  may be seen to vary as the square root of the random energy of the electron,  $\mu$ . This dependence accounts for the substantially slower variation of  $D$  with both field and model parameters. It is apparent however, that increasing the energy of the electrons does increase diffusion. In the computational approach to ACORN of Section 3.3 below, we will ignore both the model and field dependence of the diffusion coefficient. This seems well justified in view of the calculated results.

As a final parenthetical note, Equations (3.1.23) and (3.1.19) may be combined to give an expression for the Einstein relation

$$\frac{D}{\mu} = \frac{\zeta \cdot \frac{1}{2} m^* u^2}{e} \quad , \quad (3.1.24)$$

where

$$\zeta = \frac{2}{3} Y \left\{ \frac{\sqrt{1 + 4Y^2} + 1}{\sqrt{1 + 4Y^2} - 1} \right\}^{1/2} \quad . \quad (3.1.25)$$

The quantity  $\zeta$  is the distribution dependent coefficient in the general Einstein relation [Bates, et al., 1962].

The quantity displaying the strongest dependence on both the scattering model and field strength is the ionization length. The dependence of this quantity on both model parameters and field may be understood from the work of Lin, [1979] and Lin and Beers, [1981], which is based on the work of Baraff, [1962]. The first two of these papers are reproduced herein as Appendices 1 and 2 respectively because they are the result of previously sponsored NASA work on this subject. To facilitate comparison with results

in those papers, we present in Figure 3.1.12, a plot of the inverse ionization length  $\alpha$  (in dimensionless units) versus the dimensionless field variable  $X$  of Equation (3.1.11). The plot is specifically chosen to be log-linear. It can be seen that most of the curves are very nearly straight lines on this plot. This provides a rationale for extrapolation to lower field values corresponding to a fit to  $\alpha$  of the form

$$\alpha = \alpha_M \exp \left\{ - \frac{F_M}{F} \right\}, \quad (3.1.26)$$

where  $\alpha_M$  and  $F_M$  are fitting parameters. In fact, this form of  $\alpha$  is used in the ACORN computations within Section 3.3 below.

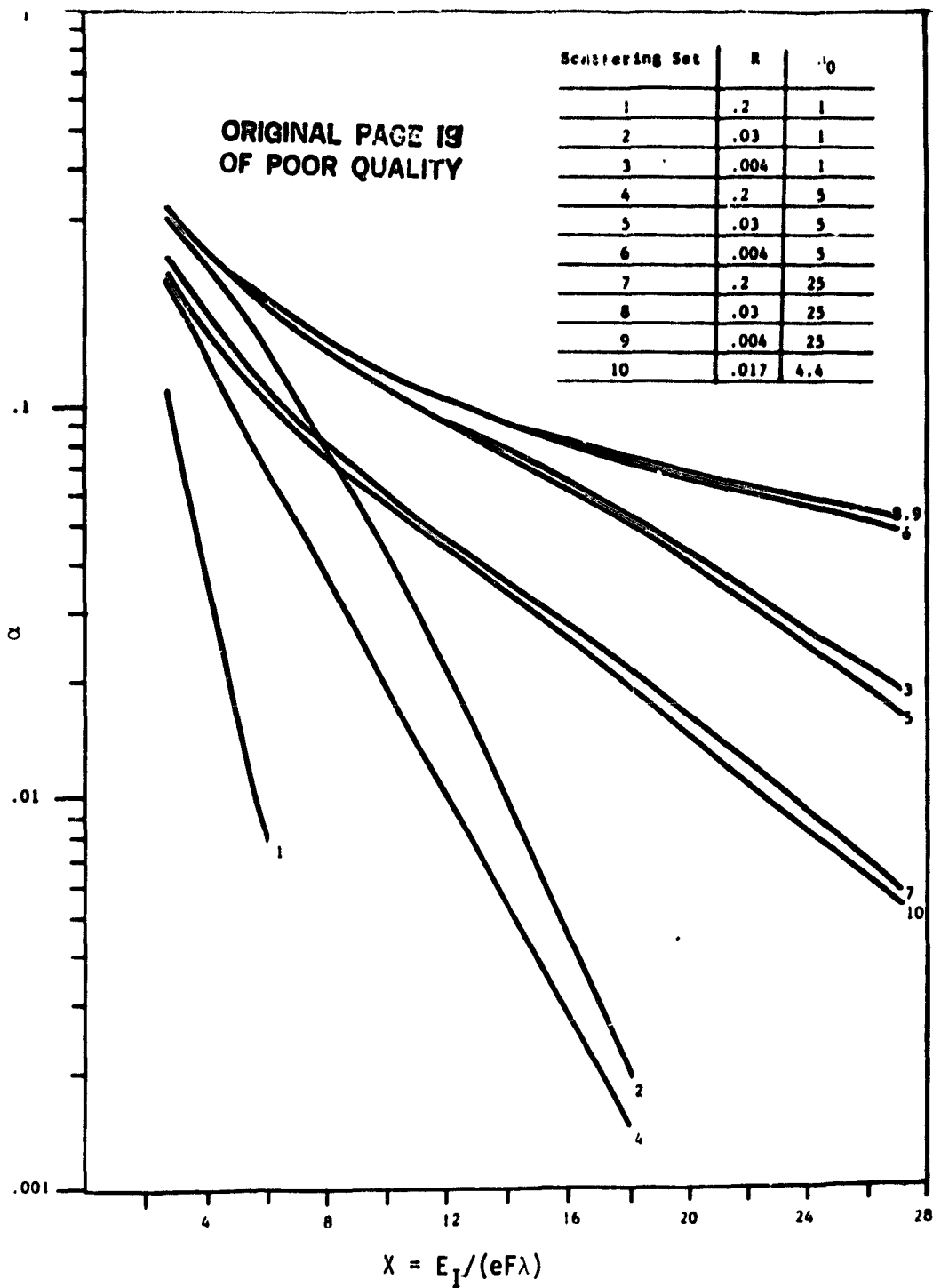


Figure 3.1.12 Inverse Ionization Length  $\alpha$  Versus the Dimensionless Field Variable  $x$ .

## 3.2 CASCAD STUDIES

CASCAD is a Monte Carlo computer code which uses the distribution of ionization sites computed by SEMC to generate an avalanche of electrons. New electrons are created at each step, and the resulting distribution of charge is used to compute the self-field. When the self-field reaches a pre-assigned value, the code scores the final distribution of positive and negative charges. This code was exercised for each of the solution sets generated by SEMC, i.e., 10 scattering models at 6 different field levels.

It is possible to estimate the fields due an avalanche by invoking various approximations. A discussion of these estimates is given in Section 3.2.1. These estimates are used as background for interpreting the results of the CASCAD calculations. The computed results are discussed in Section 3.2.2.

### 3.2.1 ANALYTICAL ESTIMATES

In a continuum approximation to the basic avalanching process, the number density of electrons  $n_-$  is determined by the equation

$$\frac{\partial n_-}{\partial t} + \vec{\nabla} \cdot (n_- \vec{v}) = \beta n_- + D \nabla^2 n_- \quad (3.2.1)$$

If the self fields are ignored, then  $\vec{v}$ ,  $\beta$ , and  $D$  are constants. The equation is then linear in  $n_-$ . The quantity  $\beta$  provides a unit of time, while  $|\vec{v}|$

**ORIGINAL PAGE IS  
OF POOR QUALITY**

provides a unit of velocity. These together provide a unit of length  $\lambda$  (the ionization length) given by  $\lambda = |\vec{v}|/\beta$ , or  $\beta = \alpha |\vec{v}|$ . Equation (3.2.1) may be brought to dimensionless form by scaling out these quantities. Choose the drift velocity to be in the  $z$  direction. Equation (3.2.1) reduces to

$$\left( \frac{\partial n_-}{\partial t'} + \frac{\partial n_-}{\partial z'} \right) = n_- + \zeta_1 \nabla^2 n_- \quad (3.2.2)$$

where  $\zeta_1 = \frac{\beta D}{v_D^2} \quad , \quad (3.2.3)$

is a dimensionless diffusion coefficient, and the space and time variables are now dimensionless. The solution to Equation (3.2.2) is

$$n_-(\vec{r}', t') = n_-^0 e^{t'} \left( \frac{1}{2 \sqrt{\pi \zeta_1 t'}} \right)^3 \exp \left[ -\frac{(\vec{x}'^2 + \vec{y}'^2 + (z' - t')^2)}{4 \zeta_1 t'} \right] . \quad (3.2.4)$$

The boundary conditions for the problem are such that the solution reduces to a  $\delta$  function centered at the origin at  $t' = 0$ , and vanishes at infinity. The solution represents a diffusion sphere which is translating in space with unit velocity. The r.m.s. sphere radius satisfies the relation.

$$\langle r'^2 \rangle = 6 \zeta_1 t' \quad , \quad (3.2.5)$$

where  $\langle \rangle$  indicates a density weighted average. Larger values of  $\zeta_1$  therefore correspond to more rapid diffusion.



**ORIGINAL PAGE IS  
OF POOR QUALITY**

The total number of electrons  $N_-$  may be shown to increase exponentially

$$N_- = N_-^0 e^{t'} \quad (3.2.6)$$

The density of positive charge sites  $n_+$  satisfies the equation

$$\frac{\partial n_+}{\partial t'} = n_- \quad (3.2.7)$$

with  $n_-$  in the form given by Equation (3.2.4), the required integral is not analytically tractable, so that the resulting charge density and electric field cannot be brought to simple form.

Reverting to dimensional variables, and working in the co-moving frame ( $\vec{y} = \vec{x} - \vec{v}t$ ), the magnitude of the electric field  $F$  due to the electrons alone may be shown to be

$$|F| = F_1 f_1 \left( \sqrt{3/2} |\vec{y}| / r_0 \right) \quad (3.2.8)$$

where

$$F_1 = \frac{3}{2} \frac{e \exp(\beta t)}{4\pi\epsilon_0 r_0^2} \quad (3.2.9)$$

$e$  is the electronic charge,  $\epsilon_0$  is the permittivity of free space,

$$r_0^2 = 6 Dt \quad (3.2.10)$$

**ORIGINAL PAGE IS  
OF POOR QUALITY**

and

$$f_1(x) = \frac{\text{erf}(x)}{x^2} - \frac{2}{\sqrt{\pi}} \frac{e^{-x^2}}{x} \quad . \quad (3.2.11)$$

In Equation (3.2.11), erf is the standard error function [Abramowitz, 1965]. The function  $f_1$  is plotted in Figure 3.2.1. It may be seen to have a maximum at  $x = 1$  ( $|\vec{y}| = \sqrt{2/3} r_0$ ). The value at the maximum is 0.428. The maximum value of the electric field is therefore

$$F_{\max} = 0.428 F_1 \quad . \quad (3.2.12)$$

A convenient form of this equation may be obtained by using Equation (3.2.10), and introducing the dimensionless time  $t' = \beta t$

$$F_{\max} = \tilde{F}_1 \left[ \frac{e^{t'}}{t'} \right] \quad , \quad (3.2.13)$$

where

$$\tilde{F}_1 = (0.428) \frac{e\beta}{16\pi\epsilon_0 D} \quad . \quad (3.2.14)$$

Introduce another dimensionless variable  $\zeta_2$  by the equation

$$\zeta_2 = \frac{e \alpha^2}{\epsilon_0 F_0} \quad , \quad (3.2.15)$$

where  $F_0$  is the ambient field. Equation (3.2.14) may then be written

$$\tilde{F}_1 = \frac{(0.428)}{16\pi} \left( \frac{\zeta_2}{\zeta_1} \right) \cdot F_0 \quad . \quad (3.2.16)$$

ORIGINAL PAGE IS  
OF POOR QUALITY

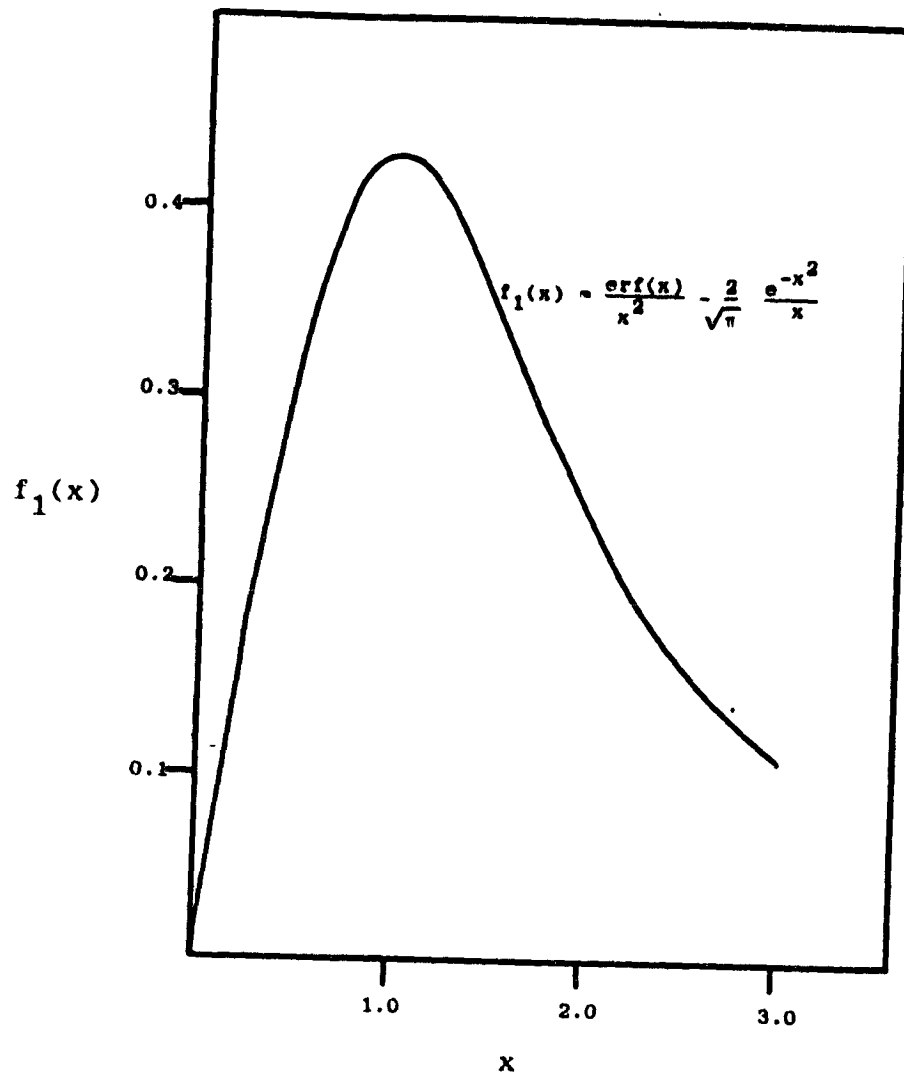


Figure 3.2.1 Dimensionless Field Variation  
for Diffusion Sphere

Equations (3.2.16), (3.2.13), together with the spatial dependence given by  $f_1(x)$  in Equation (3.2.11) give a complete characterization of the field due to the diffusing electrons. The field is radial and centered about the co-moving origin.

The function  $(e^{t'}/t')$  has a minimum at  $t' = 1$ . Assume the solution is only valid for  $t' > 1$ . Then this expression for the self-electric field gives a first estimate of when the self-field will become important. It will not become important until the field due to the negative charge alone becomes comparable to the external field. When this field does become comparable to the external, however, it does not follow that the total self-field is important. The field due to the positive charge which is left behind will give a canceling contribution over much of the volume, leading to a reduction in field.

The electric field due to the positive charge  $\vec{F}_+$  satisfies the equation

$$\frac{\partial \vec{F}_+(\vec{x}, t)}{\partial t} = -\beta \vec{F}_-(\vec{x}, t) \quad (3.2.17)$$

by virtue of Equation (3.2.7). The total electric field  $\vec{F}$  is therefore given by

$$\vec{F}(\vec{x}, t) = \vec{F}_-(\vec{x}, t) - \beta \int_0^t dt' \vec{F}_-(\vec{x}, t'), \quad (3.2.18)$$

with  $\vec{F}_-(\vec{x}, t)$  given by Equation (3.2.8). Unfortunately, the integral in Equation (3.2.18) is not analytically tractable (the situation is not helped by working with the potential).

Estimates of the peak field due to Equation (3.2.18) are necessary. It is possible to compute the multipole moments of the charge distribution giving rise to the electric field (3.2.18). The dipole movement  $\vec{p}$  is found

**ORIGINAL PAGE 13  
OF POOR QUALITY**

to be

$$\vec{p} = \frac{e\vec{v}}{\beta} (1 - e^{\beta t}) \quad (3.2.19)$$

Since the total charge  $Q$  is simply  $e^{\beta t}$ , we have the expression

$$|\vec{p}| = 2Qa \quad (3.2.20)$$

where  $2a$  is the length of the dipole and

$$2a = \frac{|\vec{v}|}{\beta} (1 - e^{-\beta t}) \quad (3.2.21)$$

After a few generations, this tends to a constant (the ionization length). Thus, a reasonable approximation to the fields is provided by the field associated with two diffusion spheres separated by an ionization length.

A good estimate of this field is provided by the field from two spheres of uniform charge density separated by an ionization length. As may be seen from Equations (3.2.12) and (3.2.9), a maximum field matching may be accomplished by putting all the charge  $Q$  inside a sphere of radius  $1.25 r_0$ , which we denote  $r'_0$ . Three cases may be distinguished:

$$(I) \quad \lambda > 2r'_0 \quad ; \quad (3.2.22)$$

$$(II) \quad r'_0 < \lambda < 2r'_0 \quad ; \text{ and } (3.2.23)$$

$$(III) \quad \lambda < r'_0 \quad . \quad (3.2.24)$$

**ORIGINAL PAGE IS  
OF POOR QUALITY**

Case (I) corresponds to two non-overlapping spheres, while case (III) corresponds to two spheres with a strong overlap (separation of centers less than a radius).

With this model, a rigorous value may be derived for the maximum field strength. The relation is

$$F_{\max} = F_0 \left\{ \sqrt{\frac{2}{3}} \cdot \frac{(0.428)}{16\pi} \frac{\zeta_2}{\zeta_1^{3/2}} \right\} \left\{ \frac{e^{t'}}{t'^{3/2}} \right\} h \left( \frac{1}{\sqrt{6\zeta_1 t'}} \right), \quad (3.2.25)$$

where the function  $h$  is defined by

$$\begin{aligned} h(x) &= \frac{1}{2} \left\{ \frac{x^2 - 2x + 2}{x(x-1)^2} \right\} & x > 2 \\ &= \frac{1}{2} & 0.618 < x < 2 \\ &= \frac{1}{2} \left\{ \frac{(x+2)}{(1+x)^2} \right\} & 0 < x < 0.618 \end{aligned} \quad (3.2.26)$$

The function  $h(x)$  is plotted in Figure 3.2.2. It has a maximum value of unity for small  $x$  (large time). The quantities in curly brackets will be recognized as the field of a dipole, written in dimensionless form. Note that this depends only on the dimensionless ratio  $(\zeta_2 \zeta_1^{-3/2})$ . The quantity  $h$  gives a measure of the degree of overlap between the positive and negative charge. Note that for long times  $h$  tends to unity, at which time there is substantial overlap of the distributions. Note that for small values of  $\zeta_1$  (diffusion less important)  $h$  gives substantial corrections to the dipole field for long periods of time.

ORIGINAL PAGE IS  
OF POOR QUALITY

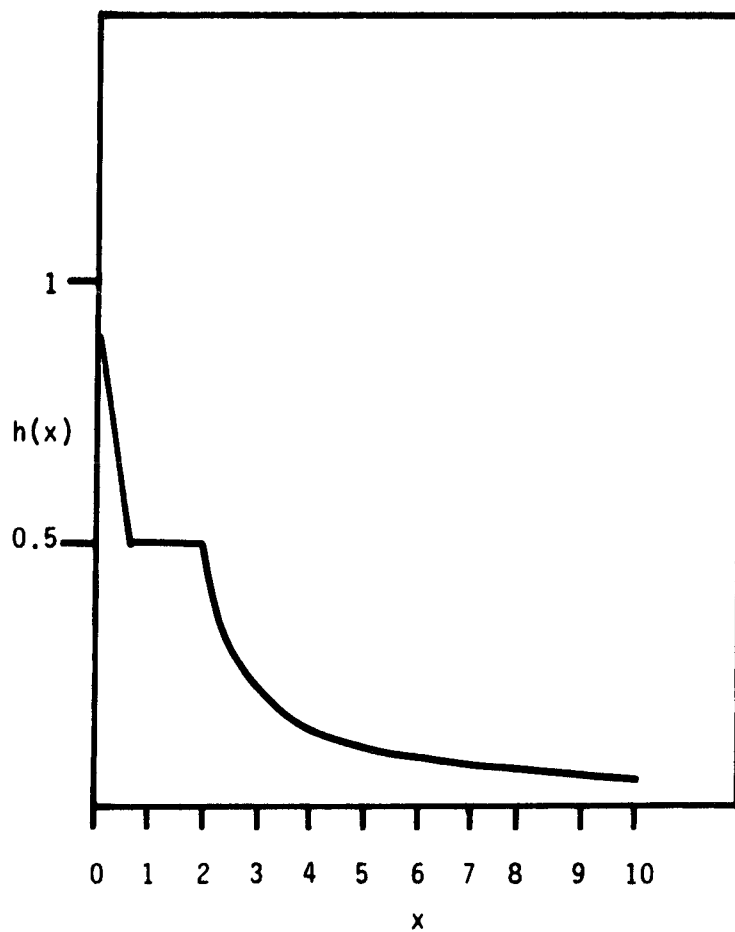


Figure 3.2.2 Plot of Function  $h(x)$  Defined in Equation (3.2.26)

In the limit that a sufficient number of electrons are involved in an avalanche so that a continuum representation is sensible, Equation (3.2.25) should provide a rather good representation of peak electric field in an avalanche. The spatial distribution implied by the model should also be rather good over most of space.

The rather complicated considerations were investigated in an attempt to understand the CASCAD computations presented in the next section. As will be explained in that section, the analytical treatment becomes inadequate when only a small number of electrons are involved in the avalanche. Further discussion may be found in the next section.



### 3.2.2 CASCAD RESULTS AND DISCUSSION

CASCAD computes the evolution of a single-electron initiated avalanche by a Monte Carlo method. The avalanche proceeds in the undistorted applied field. The self-field is computed at each stage of the process. When the self-fields reach a preassigned percentage of the applied field, the process is terminated. The purpose of this code is to provide the initial conditions for the ACORN computations of the next section. Unfortunately, it has not been possible to automate the interface of these two codes during the current period of activity.

The lack of an automatic linkage between the two codes means that it is necessary for an analyst to look over the CASCAD output very carefully, and decide on a procedure for providing an analytical fit to the data. The data fit may then be used as an input routine for defining the initial condition of the ACORN routine.

Because of the large number of computations, it was decided to attempt a universal fitting procedure for the CASCAD output. The analytical considerations of the previous section were pursued in an attempt to provide a rationale for a fitting procedure. It was hoped that an adequate fitting of the data would be provided by using the charge densities given by Equations (3.2.4) and (3.2.7).

The diagnostic which was used to compare the adequacy of a possible fit to the computed data was a comparison of the number of generations required to reach a preassigned self-field level as obtained in CASCAD versus the same quantity predicted by Equation (3.2.25). Additionally, the functional form of the fields, as computed by CASCAD, was compared to the form of the fields as given by Equation (3.2.25) and related equations.

Qualitatively, the fields computed by CASCAD appear to be describable by the model of Equation (3.2.25) and related formulae. Quantitatively, however, significant disagreement was found between the predicted values of the maximum field using Equation (3.2.25) and those computed from ACORN. The reason for this discrepancy has been uncovered. The understanding required to elucidate the discrepancy has shed new light on the avalanche process.

The understanding and resulting conclusion is as follows. When the self-fields of an avalanche become important after a relatively few generations ( $\sim 10$ ), the transition to a continuum model of the process is not strictly justified. A discrete description of the avalanche will have statistical features which are not present in the analytic continuum description of Section 3.1. The transition to a continuum description required by the CASCAD/ACORN interface must therefore be viewed as a transition to an ensemble averaged description. Further definition of the interpretation of the ACORN results will be required. Further discussion of the observations which lead to these conclusions is given below.

For each of the material models and field strengths of Section 3.1, a CASCAD computation of the avalanche was performed (60 calculations). The calculation proceeded until the self-field reached 50% of the applied field. In most cases, this required very few generations (approximately 10). Analytic computations of the number of generations required to reach this same field level were also performed. The first computations were made using the most rudimentary estimates of the field as presented in Section 3.3.2 of a previous report [Beers, et al., 1979]. Preliminary spot checks comparing these analytical results with the CASCAD results suggested good agreement. A later complete comparison of all 60 cases was performed. Significant differences appeared.

Because of these differences, it was felt that perhaps the analytic estimates which led to the equation referred to in the previous paragraph were too crude. A more detailed estimate was therefore performed. The results of this estimation procedure are presented in Section 3.2.1 above. The best

estimate of the maximum field in the avalanche is provided by Equation (3.2.25). It was believed that this equation should correctly predict the maximum field within a factor of 2. The number of generations to reach a given field should therefore be predicted to within differences of one or two from the actual.

Table 3.2.1 provides a comparison of the number of generations required to reach 50% of the impressed field for all sixty computations. The number of generations predicted by Equation (3.2.25) is shown in brackets, while the actual number achieved in the CASCAD calculation is unbracketed. It is evident from this table that good agreement between the two is not present.

The discrepancies of Table 3.2.1 are similar when cruder estimates of the self-field are made. As noted above, the first approach to explaining the differences was to obtain a better analytic estimate of the field. As evidenced by Table 3.2.1, the better estimates did not eliminate the differences. The second approach looked more carefully at the parameters controlling the CASCAD calculations.

The most obvious quantity to check is gridding which is used to perform the field calculations in CASCAD. Figure 3.2.3 summarizes the effect of grid size. The ordinate of the figure is the ratio of the number of generations obtained by CASCAD to number predicted, as taken from Table 3.2.1. The abscissa is the ratio of the axial grid size which was used in the CASCAD calculation divided by the characteristic ionization length for the problem (as obtained from SEMC). The figure is constructed as a standard scatter-plot.

It is obvious from the figure that the degree of agreement between the CASCAD computed result, and the analytical prediction is very strongly related to the normalized grid size. Large grid size corresponds to analytic underprediction, while small grid size corresponds to analytical overprediction. A linear regression of the data is also shown on the figure (the dashed line). The equation of this fit is shown on the figure.

**ORIGINAL PAGE IS  
OF POOR QUALITY**

**TABLE 3.2.1**

Comparison of Number of Generations Required for Avalanche Self-Field to Reach 50% of Impressed Field CASCAD Result is Unbracketed. Predicted Result from Equation (3.2.25) is Given in Brackets.

| Cross<br>Section<br>Set | Ambient Electric Field (V/M) |                 |                 |                 |                 |                 |
|-------------------------|------------------------------|-----------------|-----------------|-----------------|-----------------|-----------------|
|                         | $4 \times 10^9$              | $2 \times 10^9$ | $1 \times 10^9$ | $8 \times 10^8$ | $6 \times 10^8$ | $4 \times 10^8$ |
| 1                       | 9(8)                         | 18(11)          |                 |                 |                 |                 |
| 2                       | 5(8)                         | 6(9)            | 11(9)           | 18(9)           | 19(11)          |                 |
| 3                       | 2(8)                         | 5(9)            | 6(9)            | 8(9)            | 9(9)            |                 |
| 4                       | 5(10)                        | 9(11)           | 16(12)          | 18(13)          | 19(13)          |                 |
| 5                       | 5(9)                         | 5(9)            | 7(9)            | 8(9)            | 10(10)          | 14(10)          |
| 6                       | 1(9)                         | 5(9)            | 7(10)           | 7(10)           | 7(10)           | 8(10)           |
| 7                       | 5(10)                        | 7(11)           | 9(12)           | 11(12)          | 14(13)          | 16(13)          |
| 8                       | 5(8)                         | 6(9)            | 6(9)            | 7(10)           | 7(10)           | 8(8)            |
| 9                       | 5(9)                         | 7(10)           | 6(10)           | 7(10)           | 7(10)           |                 |
| 10                      | 6(10)                        | 7(10)           | 8(11)           | 10(12)          | 12(12)          | 17(12)          |

ORIGINAL PAGE IS  
OF POOR QUALITY

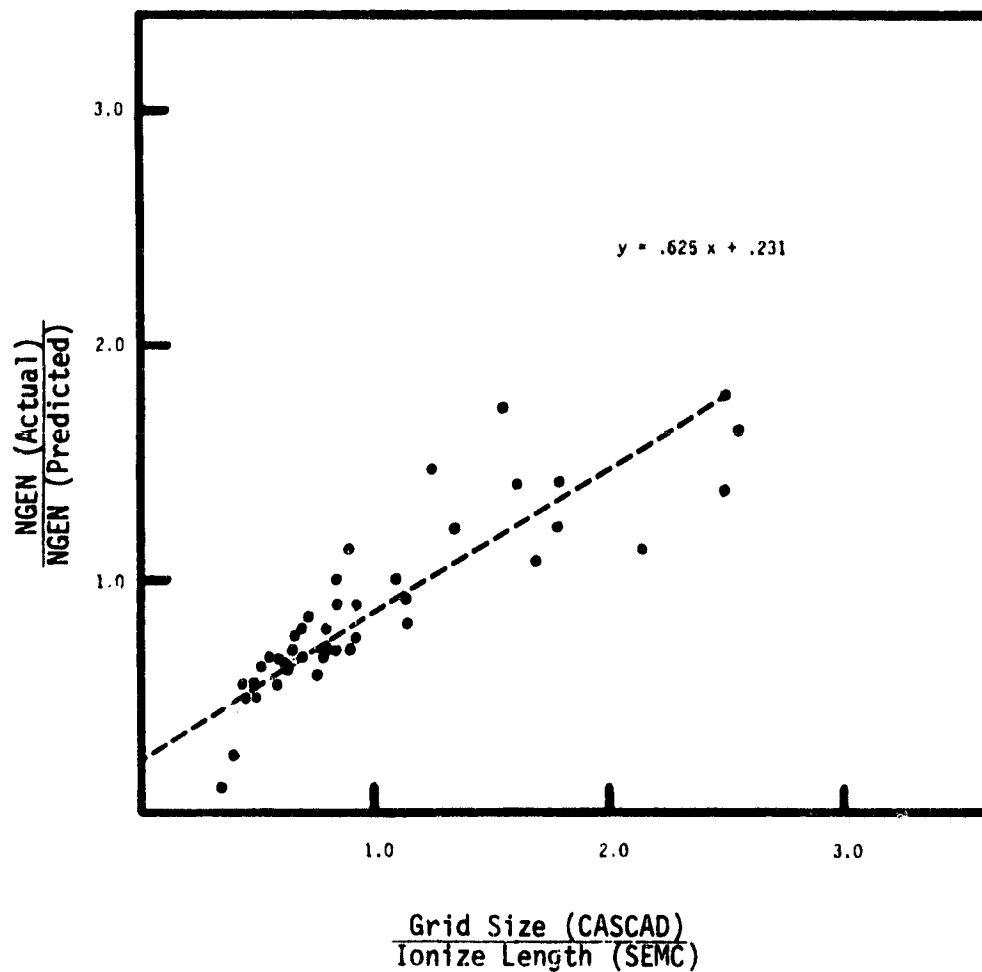


Figure 3.2.3. Scatter Plot Displaying the Covariance Between the Ratio of Computed to Predicted Generations to Achieve a Specified Relative Field Level and the Normalized Grid Size - see text for explanation.

A reasonable interpretation of Figure 3.2.3 is that the results of the CASCAD computations are strongly grid-size dependent. This hypothesis was tested by computing the identical problem for several choices of grid size. These comparative computations confirmed the hypothesis. Smaller grid size gives rise to larger values of the calculated fields. Larger grid size gives rise to smaller values of the computed field. The number of generations required to reach 50% of the applied field increases with increasing grid size.

The fact that the CASCAD results are sensitive to the choice of grid size should not be construed to mean that the results are incorrect, but only that the results are subject to interpretation. Some comments must be made about the numerical algorithm. In principle, one can easily compute the electric field from a system of discrete charges by using Coulomb's law for point charges. It was deliberately decided to not follow this procedure in computing the self-field of the avalanche. The rationale for the decision is simple. The purpose of the calculation is to provide initial conditions for the transition to a continuum description of the avalanche. The quantity which is desired is the value of the self-electric field in this same continuum description. Only if the field is large in this smeared description will it be important to the subsequent evolution of the smeared description. If a discrete representation of the field is used, it is very difficult to decide what is meant by the maximum field. Getting close to a bare charge will always lead to a large field, independent of the number of particles in the avalanche. Not only is it desired to make the transition to a continuum approximation, but it is deliberately intended to exclude this field close to the bare charge. The force between bare positive and negative charges (in the short range sense) is meant to be handled via the primary ionization processes.

We are led to the conclusion that a smeared description of the charge is necessary. Given this choice, the difficulties of gridding become apparent. If only a small number of generations are required to reach important

levels of the self-field, then the statistical aspects of the avalanche may dominate. Choosing too small a grid leads to a significant probability that bins will end up with a single charge in them, leading to the same problems with large local fields as with Coulomb's law. Choosing too large a grid tends to give cancellation of the fields due to separated charge if the grid size is larger than the separation distance. The separation of charge occurs over an ionization distance. The conclusion that must be reached from this discussion is that the best one can do in gridding the problem is to choose the grid size to be very nearly equal to the ionization length. Choosing the grid either larger, or smaller tends to lead to poor results. This statement is borne out by the linear regression which is drawn in on Figure 3.2.3. It passes very near the point (1,1).

These observations are sufficiently important to restate. A given set of discrete charges from an avalanche has electric fields associated with it which can be computed exactly using Coulomb's law. It is desired to describe this set of charges in a continuum approximation. To do this requires a choice of distance scale for describing a "charge density". Equivalently, a choice of distance scale is required for averaging the electric field. The choice of distance scale must be consistent with the scale of the physics of interest. More fine-grained distance scales always lead to larger local fields, and larger fluctuations in the local fields. A choice of grid size in the CASCAD algorithm is a choice of the distance scale over which averages are to be performed. The computed fields will depend on the choice of grid size.

The behavior of the peak computed local field in CASCAD and its dependence on grid size is entirely intelligible. The physical distance scale of importance is the avalanche length. Choice of a grid spacing significantly larger than this will lead to an averaging over positive and negative charges which will tend to obscure the effect which is being studied. Choosing grid size much smaller than this will lead to a very noisy (non smooth) local field description with larger values of the local field. The optimum choice of

ORIGINAL PAGE IS  
OF POOR QUALITY

distance scale is therefore very nearly equal to the ionization length. For this choice of gridding, the analytical results of Section 3.2.1 provide a reasonable representation of the CASCAD results.

Of course, these results were implicit in the choice of algorithms in CASCAD. The very strong dependence on grid size shown in Figure 3.2.3 was not anticipated. This strong dependence is due to the relatively small number of particles involved in the avalanche. Inspection of the analytically predicted number of generations in Table 3.2.1 shows it to be a very weak function of the problem parameters. The number of electrons is typically  $2^{10} = 1024$ . For this small number of electrons, the averaging will be highly sensitive to the choice of scale used for the averaging. The strong dependence on gridding for a relatively small variation in the grid size simply reflects the small number of particles on the avalanche.

We conclude that the charge densities computed by CASCAD may be adequately represented with Equations (3.2.4) and (3.2.7). The parameter  $t'$  is taken to have the value given by Equation (3.2.6) where  $N_0$  is unity and  $N_0$  is the total number of electrons in the avalanche. These formulae have been used to provide the initial conditions for the ACORN computations of the next section.

Because of the small number of particles in the avalanche when self-fields become important, it will be necessary in future investigations to determine more carefully the statistical fluctuations about the ensemble mean given by the above procedure. There may be significant features of the process contained in these fluctuations.



### 3.3 ACORN STUDIES

The computer code ACORN is designed to compute the self-consistent evolution of the electron avalanche. A series of computations has been performed using this code for various values of the impressed field and several different material models. These computations are discussed below.

#### 3.3.1 ACORN RELATED ANALYSIS AND SCALING

The computations to be performed were determined by the following considerations. The equations which are solved by the ACORN package depend on the three transport coefficients  $\mu$ ,  $D$ ,  $\beta$  (mobility, diffusion coefficient, ionization rate) and the impressed electric field  $F_0$ . The ionization rate  $\beta$  is related to the inverse of the ionization length (denoted  $\alpha$ ) by the equation  $\beta = \alpha v_D$  where  $v_D$  is the drift velocity in the ambient field. The quantity  $\alpha$  is often referred to as the first Townsend coefficient. Specifying  $\alpha$ ,  $\mu$  and the field provides a value of  $\beta$ . We will treat  $\mu$ ,  $D$  and  $\alpha$  as the set of independent transport coefficients.

The transport coefficients are functions of the local field. From the results of Section 3.1, it was determined that the mobility and diffusion are very nearly independent of material model for the range of models and electric fields considered. The quantity displaying the greatest variation with material model (and field strength) is the inverse ionization length,  $\alpha$ . This parameter was used as the discrimination variable. That is, it was decided to choose three material models which had first Townsend coefficients  $\alpha$  which bracketed the apparent range of variation of the  $\alpha$ 's computed for the ten distinct models.

Material model 10 (see Table 3.1.1) was specifically chosen as the nominal parameter set. Variations in material model parameters were chosen to bracket the parameters of this set. By referring to Figure 3.1.12, it may be seen that the ionization coefficient  $\alpha$  for scattering set 10 is bracketed by ionization coefficients for the other scattering sets. The values of  $\alpha$  on the high side (slow decrease with decreasing field) are clearly bracketed by those of scattering set number 9. This set was chosen as the set having the weakest dependence on field in the regime of interest. The decision on the low side was much more difficult. Scattering set number 1 had such a sharp dependence on field that values of  $\alpha$  for low field were not obtained in the SEMC computations. It was decided to eliminate this scattering set on these grounds. The ionization is simply too low at many field strengths of interest. Scattering sets 2 and 4 have very similar slopes, but different absolute values. It was decided to use scattering set number 2 to represent the lower bound on ionization behavior. Its behavior is most different in that it crosses some of the other ionization curves.

The final choice of scattering parameter sets dictated that ACORN computations be performed using SEMC data from scattering sets 2, 9 and 10. Set 10 represents the nominal case; set 9 represents the high ionization limit, and set 2 represents the low ionization limit for the computations. The specific transport coefficients used for the computations were chosen as follows. The existing version of ACORN has the requirement that the diffusion coefficient be a constant, independent of location, field strength, or orientation. The SEMC computations presented in Section 3 above demonstrate that this constancy is a reasonable approximation. We have used the corresponding values from the SEMC calculations in each of the ACORN computations. These values are presented in Table 3.3.1 below.

ORIGINAL PAGE IS  
OF POOR QUALITY

| Scattering Set | Electric Field<br>V/m | Diffusion Coefficient |
|----------------|-----------------------|-----------------------|
| 2              | $2 \times 10^9$       | $1.18 \times 10^{-4}$ |
| 2              | $1 \times 10^9$       | $9.77 \times 10^{-5}$ |
| 2              | $8 \times 10^8$       | $8.19 \times 10^{-5}$ |
| 9              | $4 \times 10^9$       | $1.42 \times 10^{-4}$ |
| 9              | $1 \times 10^8$       | $1.28 \times 10^{-4}$ |
| 9              | $8 \times 10^8$       | $1.24 \times 10^{-4}$ |
| 10             | $4 \times 10^9$       | $1.73 \times 10^{-4}$ |
| 10             | $2 \times 10^9$       | $1.60 \times 10^{-4}$ |
| 10             | $1 \times 10^9$       | $1.59 \times 10^{-4}$ |
| 10             | $8 \times 10^8$       | $1.55 \times 10^{-4}$ |
| 10             | $6 \times 10^8$       | $1.49 \times 10^{-4}$ |

Table 3.3.1  
Diffusion Coefficients from SEMC

**ORIGINAL PAGE IS  
OF POOR QUALITY**

The existing version of ACORN calls for a specific functional fit to the electronic mobility  $\mu$  as a function of the electric field. The results of the SEMC computations of Section 3.1 demonstrated that the dependence of the mobility on scattering parameter set was quite weak. A universal field dependent parameterization was therefore chosen for all ACORN calculations. The equation for the mobility  $\mu$  is given by

$$\mu = \mu_M F^{-A} \quad , \quad (3.3.1)$$

where

$$\mu_M = 1.29 \text{ m}^2/\text{V-s} \quad , \quad (3.3.2)$$

$$A = 0.44 \quad ,$$

and the local electric field  $F$  is expressed in Volts/meter.

As evidenced by Figure 3.1.12, the dependence of the ionization coefficient  $\alpha$  on local electric field  $F$  is reasonably well represented by an exponential. This type of parameterization has been chosen for all ACORN calculations, with the specific parameters depending on the material model (scattering set). The functional form of the ionization coefficient  $\alpha$  was taken to be

$$\alpha = \alpha_M \exp \left[ - \frac{F_M}{F} \right] \quad , \quad (3.3.3)$$

where  $\alpha$  and  $\alpha_M$  have units of  $\text{m}^{-1}$  and the local electric field  $F$  has units of V/m. Table 3.3.2 gives the values of the parameters  $\alpha_M$  and  $F_M$  for the various scattering sets.

The computations presented in Section 3.2 below were performed using the transport coefficients noted above. The values of the ambient field were chosen to span the regime of interest, and are reported specifically in

ORIGINAL PAGE IS  
OF POOR QUALITY

| Scattering Set | $\alpha_M (m^{-1})$ | $F_M (V/m)$        |
|----------------|---------------------|--------------------|
| 2              | $1.37 \times 10^9$  | $3.55 \times 10^9$ |
| 9              | $4.35 \times 10^8$  | $7.04 \times 10^8$ |
| 10             | $5.10 \times 10^8$  | $1.63 \times 10^9$ |

$$\alpha = \alpha_M \exp \left[ - \frac{F_M}{F} \right]$$

Table 3.3.2  
Coefficients for the Equation of the Ionization Coefficient

the results section. As a result of these calculations, certain similarities in the computed solutions were noted. These similarities prompted an investigation into the anticipated scaling dependence of solutions of self-consistent avalanche equations. An investigation of scaling relationships sheds further light on the expected behavior of the solutions. A discussion of this feature of the problem follows.

The equations which describe the evolution of the avalanche as solved by ACORN are:

$$\frac{\partial n_-}{\partial t} = \beta n_- + \vec{\nabla} \cdot (n_- \mu \vec{F}) + D \vec{\nabla}^2 n_- \quad (3.3.4)$$

$$\frac{\partial n_+}{\partial t} = \beta n_- \quad , \quad (3.3.5)$$

$$\vec{\nabla} \cdot \vec{F} = \frac{e(n_+ - n_-)}{\epsilon} \quad , \quad (3.3.6)$$

where  $n_-$  is the mobile electron density,  $n_+$  the hole density,  $\vec{F}$  the electric field,  $\mu$  the electronic mobility,  $D$  the diffusion coefficient,  $e$  the electronic charge,  $\epsilon$  the dielectric permittivity of the medium, and  $\beta = \alpha |v_D|$  is the ionization rate,  $\alpha$  being the inverse ionization length discussed above and  $v_D = -\mu F$  being the electronic drift velocity. Denote the ambient electric field by  $F_0$ , and the values of  $\beta$ , and  $\mu$  evaluated at  $F_0$  as  $\beta_0$ ,  $\mu_0$ . Let the functions  $g_1(F)$  and  $g_2(F)$  be defined by the equations

$$\mu(F) = \mu_0 g_1(F) \quad , \quad (3.3.7)$$

$$\beta(F) = \beta_0 g_2(F) \quad , \quad (3.3.8)$$

so that  $g_1$  and  $g_2$  both have values of unity at  $F = F_0$ . Choose the unit of time  $T_0$  to be  $\beta_0^{-1}$ , the unit of velocity  $V_0 = \mu_0 F_0$ , with the unit distance  $X_0$

given by  $\lambda_0 = V_0 T_0$  (ambient ionization length). If the unit of electric field is chosen to be the ambient field  $F_0$ , and all quantities are replaced with their non-dimensional analogs (which we denote with the  $\hat{\phantom{x}}$  symbol) (e.g.,  $t = T_0 \hat{t}$ ), Equations (3.3.4 - 3.3.6) may be brought to the form

$$\frac{\partial \hat{n}_-}{\partial \hat{t}} = g_2 \hat{n}_- + \hat{\nabla} \cdot (g_1 \hat{n} \hat{F}) + \zeta_1 \hat{\nabla}^2 \hat{n}_- \quad (3.3.9)$$

$$\frac{\partial \hat{n}_+}{\partial \hat{t}} = g_2 \hat{n}_- \quad (3.3.10)$$

$$\hat{\nabla} \cdot \hat{F} = \hat{\zeta}_2 (\hat{n}_+ - \hat{n}_-) \quad (3.3.11)$$

where two dimensionless variables,  $\zeta_1$  and  $\hat{\zeta}_2$  have been introduced, and are given by the relations

$$\zeta_1 = \frac{D \beta_0}{\mu_0^2 F_0^2} \quad (3.3.12)$$

$$\hat{\zeta}_2 = \frac{e n_0 \mu_0}{\epsilon \beta_0} \quad (3.3.13)$$

The variable  $\zeta_1$  is the dimensionless diffusion coefficient which was introduced in Section 3.2.1. The variable  $\hat{\zeta}_2$  depends on the choice of the unit of density  $n_0$ . A free choice of  $n_0$  is possible. In particular,  $n_0$  may be chosen so that the variable  $\hat{\zeta}_2$  has a value of unity. The choice leads to the following expression for  $n_0$ :

ORIGINAL PAGE IS  
OF POOR QUALITY

$$n_0 = \frac{\beta_0 F_0}{e \mu_0} \quad (3.3.14)$$

$$= \frac{\epsilon \alpha_0 F_0}{e}$$

The second expression in Equation (3.3.14) for  $n_0$  may be compared to an expression previously obtained for a "critical" charge density. If the critical charge density has the form  $e n_c$ , where  $n_c$  is a critical number density, then  $n_c$  is identical to the value of  $n_0$  given by Equation (3.3.14). Thus, choosing  $n_0$  so that  $\hat{\zeta}_2$  has a value of unity is equivalent to measuring number densities in terms of the critical number density  $n_c$ . Recall that the critical charge density (and associated critical number density) occurs as a saturation charge density near the streamer tip.

Equations (3.3.9 - 3.3.11) explicitly display the scaling properties of the avalanche equation. Because the parameter  $\hat{\zeta}_2$  may be chosen equal to unity, different problems are specified by different values of the parameter  $\hat{\zeta}_1$ , and different forms of the functions  $g_1$  and  $g_2$ . In the limit that  $g_1$  and  $g_2$  are weakly varying functions of the field (and hence nearly unity) different problems will be specified by the single parameter  $\zeta_1$ . This parameter is the same parameter introduced in the discussion of the electron continuity equation in Section 3.2.1. Different problems are specified by different values of  $\zeta_1$ . Other parameter variations may be obtained by dimensional scaling.

Of course, the functions  $g_1$  and  $g_2$  introduce other parametric dependence in general. If the functional form for the mobility given by Equation (3.3.1) is used, then the function  $g_1$  depends only on the dimensionless field  $\hat{F}$ , and introduces no further parametric dependence. Using the fits of Equations (3.3.1) and (3.3.3) gives rise to a form of the function  $g_2$  which has the expression

$$g_2(\hat{F}) = \exp \left\{ \frac{F_M}{F_0} \left( 1 - \frac{1}{\hat{F}} \right) \right\} \hat{F} (1 - A) \quad (3.3.15)$$

where  $A = 0.44$  was derived in the above mentioned equations.



The function  $g_2$  depends on the dimensionless parameter  $(F_M/F_0)$ . The range of variation  $\zeta_1$  and  $(F_M/F_0)$  for the computed results is noted below. Within the existing models used for ACORN, these two parameters are sufficient to describe all possible distinct solutions.

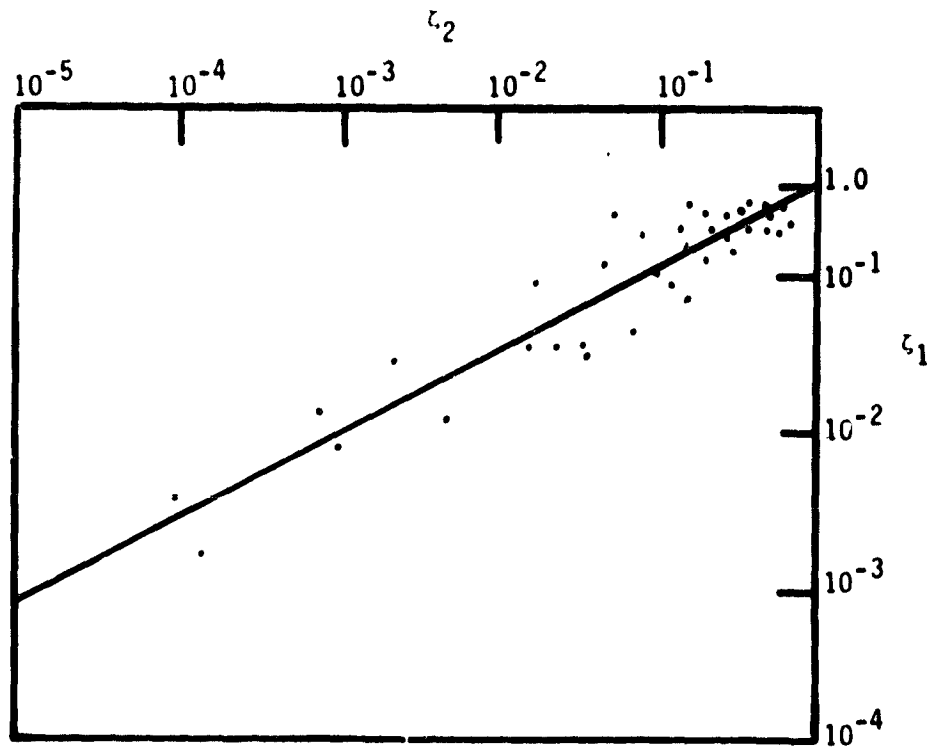
Several other interesting features of the scaling should be noted. Let subscript "naught" again denote values of parameters in an ambient electric field  $F_0$ . Equation (3.3.12) gives an expression for a dimensionless constant which can be formed from some of these parameters. The set of parameters defining a problem is  $\{D_0, \beta_0, \mu_0, F_0, e/\epsilon\}$ , together with the subsidiary relations  $v_0 = \mu_0 E_0$ , and  $\beta_0 = \alpha_0 v_0$ . This entire set of parameters may be characterized in a slightly different manner. One chooses three independent dimensional parameters to provide the fundamental dimensions. The dimensions of any of the given quantities may then be written as powers of these basic dimensional units. Any given quantity may be rewritten as a dimensionless constant multiplied by the appropriate algebraic expression of fundamental units.

For the above set of quantities, a convenient choice of the dimensional parameters is  $\beta_0$ ,  $v_0 = \mu_0 E_0$ , and  $E_0$ . The remaining parameters  $(D_0, e/\epsilon)$  may be re-expressed as dimensionless constants times various powers of the dimensional units. With the indicated choice of units, the dimensionless diffusion coefficient is given by  $\zeta_1$  of Equation (3.3.12). The dimensionless coupling constant corresponding to  $e/\epsilon$  (denoted by  $\zeta_2$ ) is given by

$$\zeta_2 = \left( \frac{e \beta_0^2}{\epsilon F_0 v_0^2} \right), \quad (3.3.16)$$

$$= \frac{e \alpha_0^2}{\epsilon F_0}.$$

ORIGINAL PAGE 13  
OF POOR QUALITY



$$\zeta_1 = (0.379) \cdot \zeta_2 = 0.533$$

Figure 3.3.1 Scatter Plot of the Dimensional Quantities  $\zeta_1$  and  $\zeta_2$  Obtained From Various SEMC Computations. See text for explanation.

**ORIGINAL PAGE IS  
OF POOR QUALITY**

The reason for the choice of notation, and the precise relation of  $\zeta_2$  to  $\hat{\zeta}_2$  will emerge below.

The quantities  $\zeta_1$  and  $\zeta_2$  characterize the dimensionless parameters which can be formed from the given problem parameters. Shown in Figure 3.3.1 is a scatter plot of the values of  $\zeta_1$  and  $\zeta_2$ . The plot was constructed as follows. For each SEMC computation (10 materials models, 5 field levels) the values of  $\zeta_1$  and  $\zeta_2$  were computed. Each SEMC computation gives rise to a pair  $(\zeta_1, \zeta_2)$ . Each of these pairs was plotted on the figure.

From the plot, it may be seen that the two parameters show a very wide range of variation, (as much as five orders of magnitude for  $\zeta_2$ ). The plot is rather remarkable because a definite covariance is shown between the values of these presumably independent variables. A linear regression of the observed covariance yields the equation

$$\zeta_1 = (0.379) \cdot \zeta_2^{0.533} \quad (3.3.17)$$

This equation suggests that the quantity  $(\zeta_1^2/\zeta_2)$  is very nearly a constant over a wide range of parameter values. This quantity has the expression

$$\frac{\zeta_1^2}{\zeta_2} = \frac{\epsilon}{e} \left( \frac{D_0}{\mu_0} \right)^2 \frac{1}{F_0} \quad (3.3.18)$$

This equation, together with Equation (3.3.17) implies that the transport coefficients  $\mu_0$ ,  $D_0$  obtained from SEMC computations satisfy the rough equality

$$\frac{D_0}{\mu_0} \approx (0.379) \cdot \sqrt{\frac{eF_0}{\epsilon}} \quad (3.3.19)$$

For the choice of models which have been computed, Equation (3.3.19) is an Einstein type relation which gives the field dependence of the mean electron energy. Though the relation (3.3.19) appears very reasonable, there is no a priori explanation of this behavior. It remains a problem for future understanding.

The net result of the above discussion is that a SEMC output is characterized by a single parameter,  $\zeta_1$ . The second parameter  $\zeta_2$  is obtained from  $\zeta_1$  by the relation (3.3.17). Two things should be noted. The first relates to the regression Equation (3.3.17) and the second relates to scaling of ACORN results. In a preliminary report of this work [Beers, et al., 1981]; (reproduced here as Appendix 3) it was reported that  $\zeta_1^{3/2}/\zeta_2$  was very nearly a constant for the parameters of interest. It was noted that the quantity  $(\zeta_1^{3/2}/\zeta_2)$  also occurs in Equation (3.2.25), the expression for the self-field of the undistorted avalanche. It was speculated that there was some deeper meaning associated with this coincidence. This speculation is now believed to be incorrect.

The constancy of the quantity  $(\zeta_1^{3/2}/\zeta_2)$  was obtained from an inadequate (eyeball) fit to the data. The properly weighted linear regression of the data represented by Equation (3.3.17) yields the approximate constancy of  $(\zeta_1^2/\zeta_2)$ . This is a very different result. Though the resulting expression for the Einstein relation is not understood a priori it does have a reasonable form. Were  $(\zeta_1^{3/2}/\zeta_2)$  to be constant, the resulting Einstein relation would contain an exponential of the field on the right-hand side, a very difficult expression to reconcile. The constant value of  $(\zeta_1^2/\zeta_2)$  also makes it clear that this relation is completely independent of the self-field effects of undistorted avalanches. There is no relation.

In the same publication [Beers, et al., 1981] it was further suggested that the covariance of the values of  $\zeta_1$  and  $\zeta_2$  exhibited by Figure 3.3.1 provides an explanation of the similarity of the form of the solutions of the ACORN computations. While this statement is superficially correct, it

ORIGINAL PAGE IS  
OF POOR QUALITY

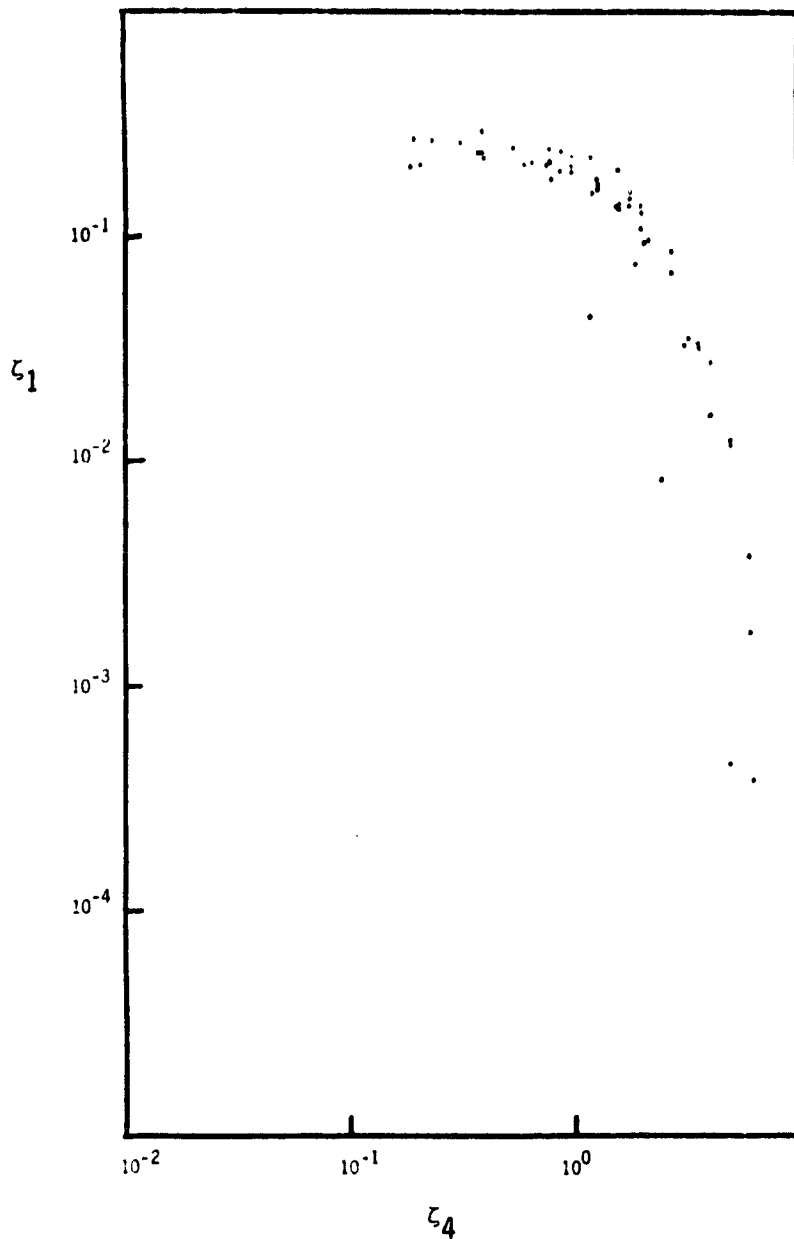


Figure 3.3.2. Scatter Plot of the Quantities  
 $\zeta_1$ ,  $\zeta_4$ . See text for explanation.

does not provide the proper interpretation of the phenomenon. As shown in the discussion on the scaling of the underlying equations, the physical description may be cast in a dimensionless form which depends on the dimensionless parameters  $\zeta_1$  and  $\hat{\zeta}_2$ . The quantity  $\hat{\zeta}_2$  as given by Equation (3.3.13) depends on a choice of the unit density  $n_0$ . If the unit density is chosen to be  $n_0 = \alpha_0^3$ , the quantity  $\hat{\zeta}_2$  takes on the value of  $\zeta_2$ . With this choice, the equations depend on the two parameters  $\zeta_1$  and  $\zeta_2$ .

However, as shown in the previous discussion of the scaling, the unit density may be chosen such that  $\hat{\zeta}_2$  takes on a value of unity. Even if there were no covariance of  $\zeta_1$  and  $\zeta_2$ , the problem may be brought to a form which does not depend on  $\zeta_2$ . The reason that a single parameter defines a problem is now apparent. There is no predefined natural unit of density for the problem. The only naturally occurring density is the critical density, a quantity which is dynamically determined. The conclusion to be drawn from these facts is that the dependence of the solution on the parameter  $\zeta_2$  is trivial, and can be obtained by dimensional arguments alone. In the limit that  $g_1$  and  $g_2$  are constant, problems solved by ACORN depend on a single parameter,  $\zeta_1$ .

The characterization of the scaling laws may now be completed. Dimensional analysis is used to bring the equations to the form (3.3.9-3.3.11). A choice of  $n_0$  is made such that  $\hat{\zeta}_2$  is unity. Explicit use is made of the ACORN functional fits for mobility and ionization rate to provide explicit functional forms for  $g_1$  and  $g_2$ . The two functions  $g_1$  and  $g_2$  depend on the dimensionless field  $\hat{F}$  and a single dimensionless parameter (which we denote  $\zeta_4$ ). The quantity  $\zeta_4$  is simply the ratio  $F_M/F_0$  of Equation (3.3.15). Thus, all problems solved by ACORN in this series of calculations depend on two parameters,  $\zeta_1$  and  $\zeta_4$ . There are no other parameters.

The dependence on two parameters is only apparent. Shown in Figure 3.3.2 is a scatter plot of the values of  $(\zeta_1, \zeta_4)$  the plot was constructed by computing the values of  $\zeta_1$  and  $\zeta_4$  which occur for the different SEMC computations. Each point represents a separate SEMC calculation. Again, a strong covariance

with very little scatter can be seen. The relation between  $\zeta_1$  and  $\zeta_4$  displayed by Figure 3.3.2 is easily understood. The quantity  $\zeta_1$  depends on  $\zeta_4$  through the quantity  $\beta_0$ . Because the dependence is exponential the small variation in other problem parameters is marked.

The conclusion is that for practical purposes, all ACORN computations may be shown to depend on a single parameter. The parameter  $\zeta_1$  (or  $\zeta_4$ ) may be chosen as the discriminating parameter. All other changes of problem parameters which do not vary the value of  $\zeta_1$  lead to solutions which can be obtained by dimensional scaling.

### 3.3.2 ACORN RESULTS AND DISCUSSION

A series of eleven computations was performed with the ACORN code. Transport coefficients were obtained for scattering sets (10, 9, 2) as described in Section 3.3.1. Scattering set 10 was used for computations at 5 field values ( $4 \times 10^9$ ,  $2 \times 10^9$ ,  $8 \times 10^8$ ,  $6 \times 10^8$  volts/meter), while scattering sets 9 and 2 were used for computation at three field values ( $4 \times 10^9$ ,  $2 \times 10^9$ ,  $8 \times 10^8$  volts/meter). The rationale for the choice was discussed in Section 3.3.1.

The plots which were generated as diagnostics of the calculations were quite remarkable. Visual inspection of these plots leads to a very strong impression that the form of the solution is the same, independent of problem parameters. That is, the plots are all qualitatively the same as the plots which were previously presented for a single computation [Beers, et al., 1979]. This "sameness" of the solutions was regarded as highly significant. A substantial investigation was initiated to understand this occurrence. The results of that investigation will now be discussed.

The investigation has been based on the notion of similarity solutions of mathematical models. The concept of similarity solutions of the hydrodynamical equations has a relatively well-defined meaning [Landau and Lifschitz, 1959]. In the simplest sense, it refers to solutions which depend on certain ratios of problem parameters. The most elementary examples involve one-dimensional time-dependent flows which are not characterized with either a time or distance scale. The solutions of the equations can be shown to depend on the ratio ( $x/t$ ) only, and not  $x$  and  $t$  separately, where  $x$  is the spatial variable, and  $t$  the time variable. The use of the term similarity is related to the same word in geometry.

After completing the work reported herein, an analytic similarity solution to the one-dimensional avalanche problem was discovered. It is a



similarity solution in the ordinary hydrodynamic sense. The details of this solution will be reported elsewhere. Its properties have not been fully investigated as of this date. In the remainder of this section, a discussion will be given which presents some of the results which led to the belief that this solution existed. The importance of this type of solution is that all possible parameter variations can be accounted for by properly scaling and interpreting a single computed solution.

The first step in a search for similarity solutions is to perform a detailed dimensional analysis. The results of that analysis were presented in Section 3.3.1 above. It was shown that the dependence of the solutions on the multiplicity of problem parameters could be represented by a single non-dimensional parameter, together with dimensional scaling.

The second step in attempting to discover a universal similarity solution is to construct simple, easily viewed diagnostics of the solution. The plotted outputs of the quantities in two dimensions as a function of time are too complicated to provide simple measures of the similarity of the solutions (except in the pattern recognition sense that the visual appearance of the plots is the same). Simple quantitative measures are required. The remainder of this section provides some of the simple diagnostics of the solution which were investigated.

The diagnostics presented below were investigated specifically to determine if the ACORN computation could be interpreted in terms of a single similarity solution. For the purposes of this investigation, a generalized sense of the words "similarity solution" was felt to be important. In this context, we need a generalized idea of when two solutions are the "same". The most general point of view is topological. We refer the reader to the book by Thom [1975] as an example of this generalized point of view. The impact on the investigation reported below was to allow a wider latitude in the investigation. In all further discussions in this section the word similarity will have a deliberately vague meaning to allow for these possible generalizations.

**ORIGINAL PAGE IS  
OF POOR QUALITY**

The result of the investigations is that all the ACORN computations appear to be interpretable in terms of a single similarity solution.

The simplest diagnostic of the evolution of the avalanche is the total number of electrons involved in the process. By integrating Equation (3.3.4) over all space, the following equation is obtained for the total number of electrons  $N$

$$\frac{dN}{dt} = \langle \beta \rangle N \quad , \quad (3.3.20)$$

where

$$\langle \beta \rangle = \frac{\int d^3x \beta n_-}{N} \quad , \quad (3.3.21)$$

is the density weighted average ionization parameter. The solution of Equation (3.3.20) is simply

$$N = N_0 \exp \left[ \int_0^t dt' \langle \beta(t') \rangle \right] \quad . \quad (3.3.22)$$

For early times, when self-fields are unimportant  $\langle \beta \rangle \approx \beta_0$  where  $\beta_0$  is the value of  $\beta$  in the ambient field  $F_0$ . It is sensible to plot the number  $N$  versus the dimensionless time  $\beta_0 t$ . Shown in Figure 3.3.3 is a composite graph on which the computed results for all eleven computations are shown. From this plot (in dimensionless variables) it may be seen that the solutions have a general trend. As the self-fields build up, the rate of avalanching decreases, giving a decreasing slope to the graph. The number of electrons involved shows a remarkably small scatter. The mean fit shown on the plot represents the average behavior. It is apparent that the boundaries of the envelope of points have a very similar appearance. The composite plot was generated to display this similarity. Shown in Figure 3.3.4 is a plot of points from four separate runs, with a distinct symbol for each computation. In this figure it is easy to discern the distinct smooth curves of the individual outputs. The curves are clearly similar.

What is meant by this similarity may be made explicit by the following recourse to a simple example. From Equation (3.3.20) it is expected that  $N$  is a unique function of time. Assume that the function is invertible and that the inverse is analytic. Then  $\langle \beta \rangle$ , which depends explicitly on  $t$ , may be expressed as a function of the density  $N$  (chain rule). Assuming  $\langle \beta \rangle$  to be an analytic function permits a Taylor series expansion about  $N = 0$ . The first term in the expansion is clearly  $\beta_0$ . By retaining powers through the first order, it is found that

$$\langle \beta \rangle = \beta_0 \left( 1 - \frac{N}{N_F} \right), \quad (3.3.23)$$

where  $N_F$  is defined by

$$\frac{\beta_0}{N_F} \equiv \left. \frac{d\langle \beta \rangle}{dN} \right|_{N=0}. \quad (3.3.24)$$

The minus sign has been introduced in Equation (3.3.23) to indicate that the curve in Figure 3.3.3 is turning down. With the approximation of Equation (3.3.23) (which is valid for sufficiently small  $N$ ), Equation (3.3.20) becomes

$$\frac{dN}{dt} = \beta_0 N - \frac{N^2}{N_F} \quad (3.3.25)$$

which will be recognized as the classical equation of population growth in the presence of competition [Davis, 1962]. The solution of Equation (3.3.25) is

$$N = \frac{N_0 e^{\beta_0 t}}{1 + \frac{N_0}{N_F} (e^{\beta_0 t} - 1)}, \quad (3.3.26)$$

ORIGINAL PAGE IS  
OF POOR QUALITY

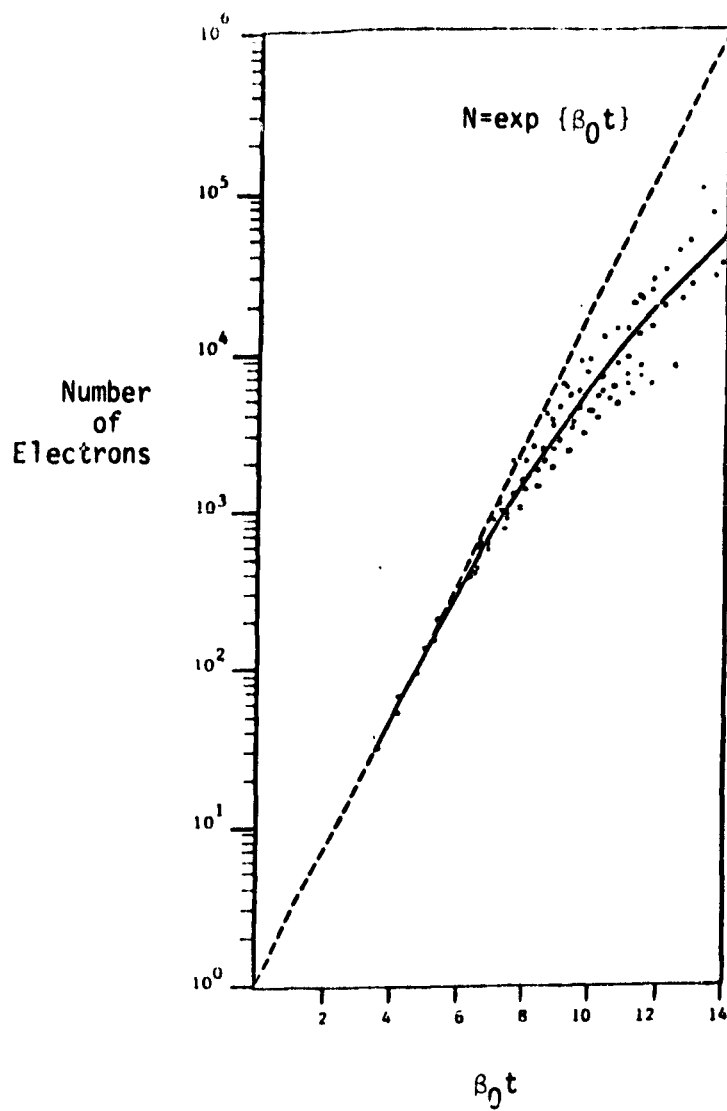


Figure 3.3.3. Composite Scatter Plot Displaying Separate Computations of the Number of Electrons Versus the Dimensionless Time  $\beta_0 t$ . See text for explanation.

ORIGINAL PAGE IS  
OF POOR QUALITY

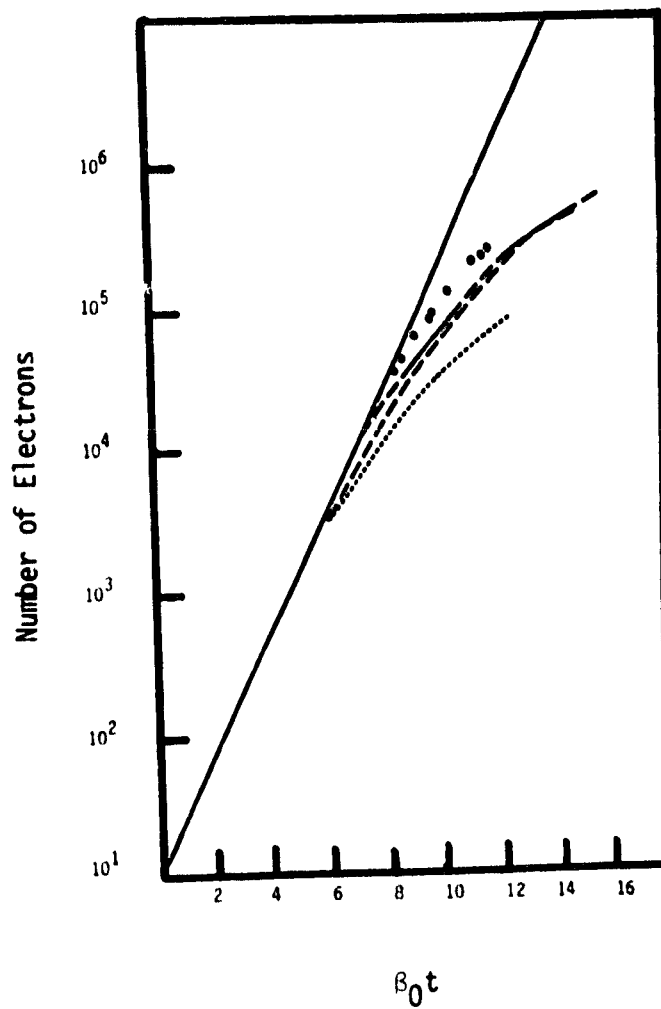


Figure 3.3.4. Plot of the Number of Electrons Versus  $\beta_0 t$  for Several Different ACORN Computations. See text for explanation.

ORIGINAL PAGE IS  
OF POOR QUALITY

where  $N_0$  is the population at  $t = 0$ . Figure 3.3.5 is a plot of Equation (3.3.26) for the condition that  $N_0 = 1$ , and the three cases  $N_F = 10^3, 10^5, 10^7$ . The solution saturates at a value  $N_F$  making the notation transparent. These curves clearly have the same form and are only shifted with respect to one another. Shifting can be accomplished by plotting  $N/N_0$  versus  $\beta_0 t$ , and choosing  $N_0$  such that  $N_0/N_F$  is a constant.

Equation (3.3.25) is only an approximate expression, valid for small  $N$ . Higher order terms will very likely alter the behavior. In fact, there are reasons to believe that  $N$  increases linearly with  $t$  for long times [Beers, et al., 1978], so that the expansion of Equation (3.3.23) is at best asymptotic. The illustration serves to clarify the ideas of similarity and does have some physical content for small enough  $N$ .

A second simple diagnostic also shows behavior suggestive of similarity. Let  $z$  denote the distance along the field measured from some reference position. Let the symbol  $\langle \rangle$  denote density weighted average values of quantities. For instance, the mean location of the negative charge is given by

$$\langle z \rangle = \frac{\int z n_-(x) d^3x}{N} \quad . \quad (3.3.27)$$

It follows from the equation of continuity for the electron density (Equation 3.3.4) that the following equation holds:

$$\frac{d \langle z \rangle}{dt} = \langle v_z \rangle + \{ \langle \beta z \rangle - \langle \beta \rangle \langle z \rangle \} \quad . \quad (3.3.28)$$

For early times, when self-fields are unimportant,  $\langle \beta z \rangle \approx \langle \beta \rangle \langle z \rangle$  because of the constant value of  $\beta$ . Thus, for the undistorted avalanche, with  $\langle v_z \rangle \approx \mu_0 E_0$ ,

ORIGINAL PAGE 18  
OF POOR QUALITY

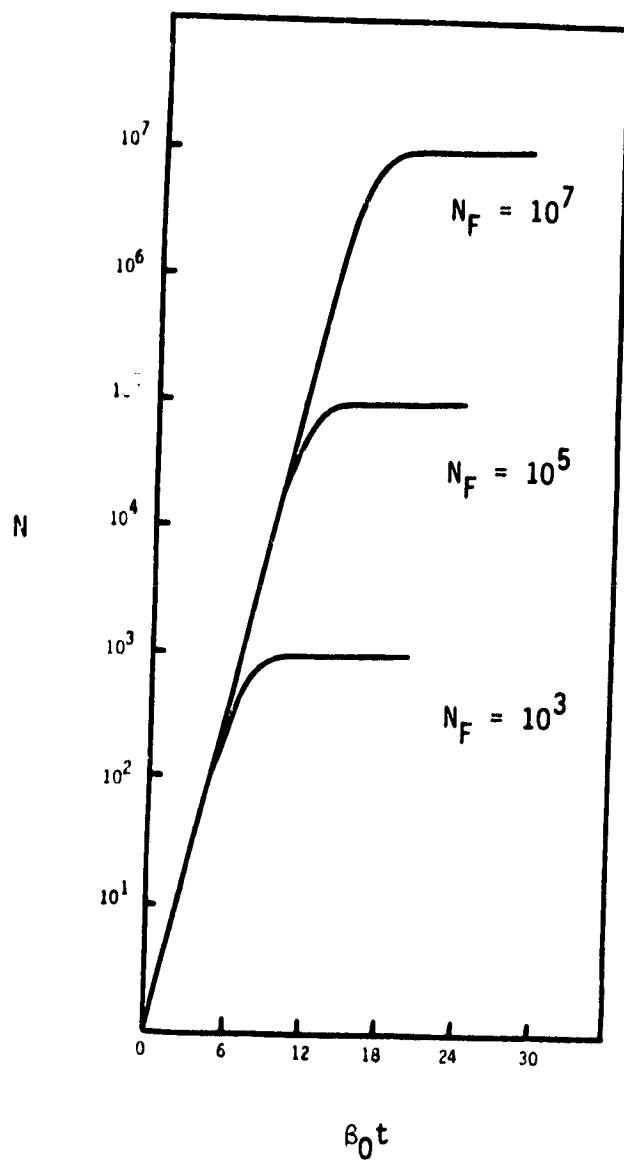


Figure 3.3.5. Plot of Equation (3.2.26), for  $N_0 = 1$ , and Several Values of  $N_F$ .

**ORIGINAL PAGE IS  
OF POOR QUALITY**

$$\langle z \rangle = \langle z \rangle_0 + (\mu_0 E_0 t) \quad (3.3.29)$$

or

$$\alpha_0 (\langle z \rangle - \langle z \rangle_0) = \beta_0 t \quad (3.3.30)$$

Departures from a straight line on a plot of  $\alpha_0 \langle z \rangle$  versus  $\beta_0 t$  will depict the integrated effect of the dynamics on the right-hand side of Equation (3.3.28).

Shown in Figure 3.3.6 is a composite plot constructed from all the computed solutions of the motion of the centroid of the electrons. Two branches of the solution are apparent on this graph, but most of the computed points are along a single curve. Shown on the figure is a constant acceleration fit of the data (i.e., quadratic in  $\beta t$ ). The value of the acceleration in dimensionless units  $\beta v_0$  is  $2.0 \times 10^{-2}$ . The most interesting feature is that the velocity is increasing, not decreasing. The enhancement of the field due to space charge is generating a faster drift with the field, faster than drift in the ambient field alone. The possibility of this occurrence was suggested in a previous publication [Beers et al., 1979].

Introduce the quantity  $\delta\beta$  by the equation

$$\delta\beta = \frac{\langle \beta z \rangle}{\langle z \rangle} - \langle \beta \rangle \quad (3.3.31)$$

Assuming that the initial value of  $\langle z \rangle$  vanishes for  $t = 0$ , the solution of Equation (3.3.28) is

$$\langle z \rangle (t) = \exp [B(t)] \int_0^t dt' \langle v_z \rangle (t') \exp [-B(t')] , \quad (3.3.32)$$

where

$$B(t') = \int_0^{t'} dt'' \delta\beta (t'') \quad (3.3.33)$$



ORIGINAL PAGE IS  
OF POOR QUALITY

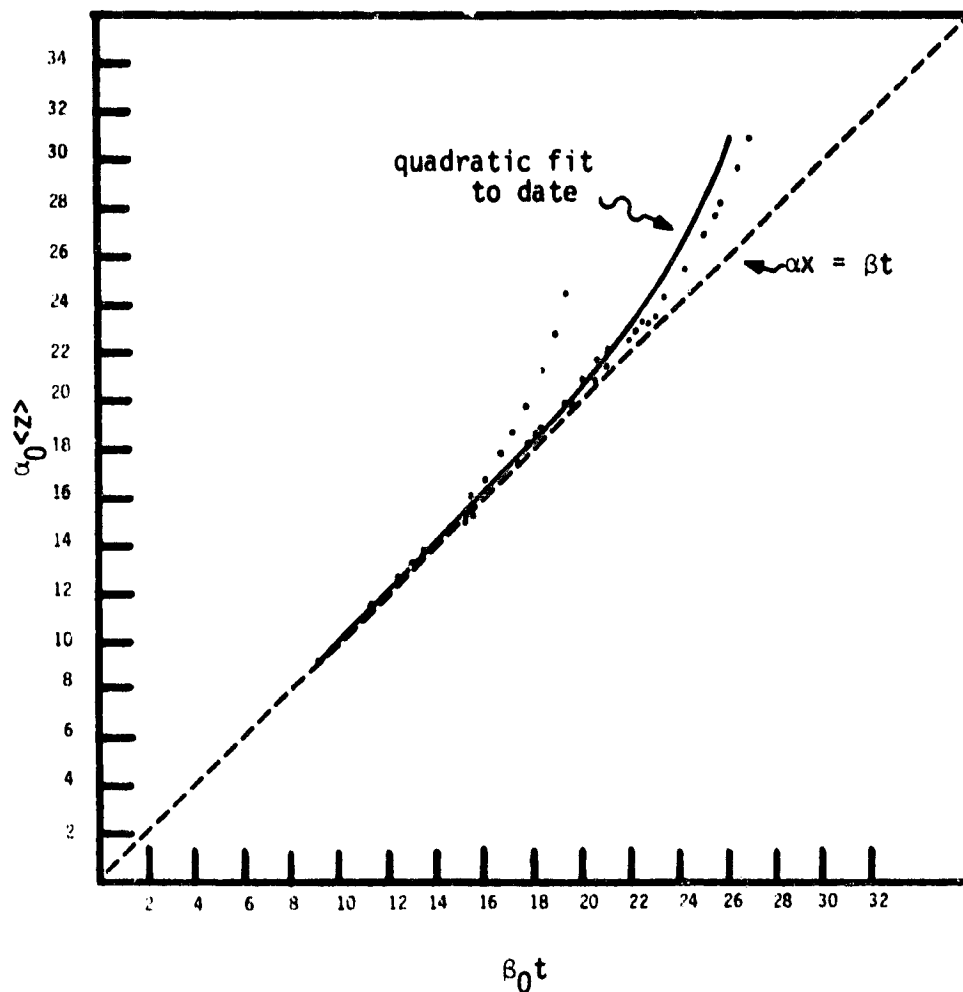


Figure 3.3.6. Location of the Centroid of Electrons as a Function of Time Plotted in Dimensionless Units. Composite of all ACORN Computations. Refer to text for explanation.

This form of the solution shows that the behavior seen in Figure 3.3.6 is rather remarkable. That is, the fit to the equation shows a quadratic dependence on time, while solution (3.3.32) shows explicitly an exponential. This demonstrates that either  $B(t)$  is very small, or that some other delicate cancellations occur. Of course, the solution (3.3.32) is implicit because  $\delta\beta$  depends on  $\langle z \rangle$ . This dependence may explain in general the weak time dependence displayed by the computed solutions.

Other evidence suggests however, that the delicate cancellation is real. Referring to Equation (3.3.23), it may be seen that  $\langle \beta \rangle$  depends on  $N$ . For short enough times,  $N$  depends exponentially on time as given in Equation (3.3.26). If this explicit time dependence for  $\langle \beta \rangle$  is introduced into Equation (3.3.28), then the right-hand side contains a term with exponential dependence, while the left-hand side is linear in time (from the computed solution). Thus, the other terms on the right-hand side of Equation (3.3.28) must also introduce exponential terms which provide a delicate cancellation to provide a linear behavior in  $t$ .

The significance of this point is that it is suggestive of a similarity solution. Because  $\langle v_z \rangle$  is not expected to depend exponentially on time, the simplest solution to the cancellation problem is obtained by demanding that  $\delta\beta$  be small, i.e.,

$$\langle \beta z \rangle - \langle z \rangle \approx 0. \quad (3.3.34)$$

If Equation (3.3.34) is approximately true, it implies a remarkable constraint on the solution. Recall that  $\beta$  is a very strong function of the electric field (and hence the charge density). Relatively small variations in the field distribution could make large differences in the moments occurring in Equation (3.3.34). It appears that the negative feedback in the dynamical equations adjusts the charge and field distribution so that Equation (3.3.34) is approximately true. Because  $\beta$  is such a strong function of  $E$ , it seems unlikely that there are many field

distributions which provide the minimization associated with this constraint. A natural interpretation is that the solution has moved to a stable equilibrium (in some sense) and continues in that state.

Further diagnostics of the evolution may be obtained from the charge distribution. Inspection of contour plots of the distribution of charge gives a strong impression of similarity. Visually, there is little to distinguish the contours for the individual computations from those previously presented [Beers, et al., 1979]. An attempt to quantify this similarity may be made by considering the multipole moments of the distribution. These are scalar diagnostics of how the charge is distributed in space. ACORN computes these quantities as part of the numerical package. It must be mentioned that they are computed in a moving frame. The procedure is as follows. The centroid of negative charge is first computed ( $\langle z \rangle$  in the above discussion). A similar computation is performed for the positive charge. The origin for the multipole expansion is then chosen to be at the midpoint between the two charge centroids.

In Section 3.2.1, a discussion of the dipole moment  $p$  of the undistorted avalanche was given. It was shown that  $p$  quickly tended to the limit  $p = 2Qa$ , where  $Q$  was the total charge of the electrons in the avalanche, and  $2a$  was the avalanche length. An inspection of the dipole moment as computed by ACORN shows that this behavior persists throughout the self-consistent phase of the evolution. A plot of the dipole moment in time shows an identical behavior to the behavior of the total number of electrons involved in the process (Figure 3.3.4). The dipole length shows a very small variation.

The behavior of the quadrupole moment has also been investigated. Utilizing the techniques of Section 3.2.1, it is possible to derive an exact expression for the quadrupole moment of the undistorted avalanche. Denoting this moment as  $q$ , it is found that

$$q = \frac{4Q}{\alpha_0^2} \left[ e^{-\beta_0 t} + \beta_0 t - 1 \right], \quad (3.3.35)$$

where  $Q$  is the total electronic charge,  $\alpha_0$  is the inverse ionization length, and  $\beta_0$  is the ionization rate. After a few generations, the term in brackets increases linearly with time. An interesting quantity to plot is the dimensionless ratio  $(q\alpha_0^2/4Q)$  as a function of the dimensionless time  $\beta_0 t$ .

Shown in Figure 3.3.7 is a plot of this dimensionless ratio as a function of  $\beta_0 t$ . The origin of time for each individual computational set was chosen to correspond to the origin for the number of electrons in the distribution. At first sight it may seem that there is little order in this figure. It must be remembered, however, that the quantity which is plotted is the ratio of two exponentially growing quantities. Small absolute errors in either of the quantities can lead to relatively large percentage errors in the ratio. A reasonable interpretation of this plot is that the quadrupole moments of the charge distributions are also very similar for different parameter choices. Generally they have the same behavior as given by Equation (3.3.35). It should also be mentioned that each individual set of points for a given computation varies smoothly with time.

No higher order moments were computed in the ACORN calculations, as they were not required for the convergence of the numerical algorithm.

All of the diagnostics discussed above support the statement made at the beginning of this section which noted that a visual inspection of the plotted output strongly suggested a great similarity of all solutions. A major portion of this similarity was deduced in Section 3.3.1 where the scaling properties of the solutions were discussed. It was determined that the problem could be reduced to solving a set of dimensionless equations depending on a single dimensionless parameter. The results of this section have shown that simple diagnostics go further than this and strongly imply that solutions having different values of the dimensionless problem parameter are also similar. It would appear that when properly interpreted, there is but a single problem described by ACORN.

ORIGINAL PAGE IS  
OF POOR QUALITY

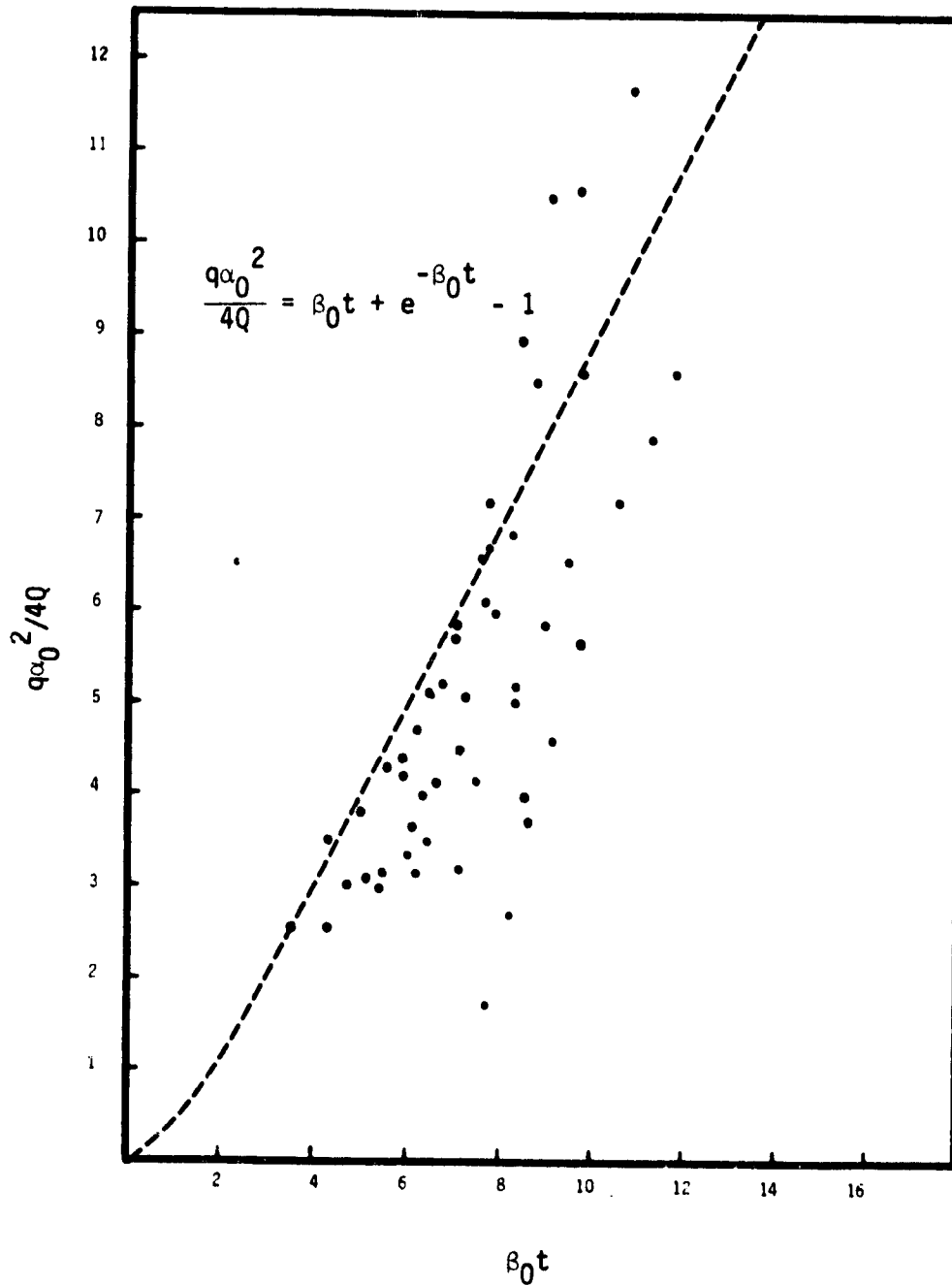


Figure 3.3.7. Dimensionless Quadrupole Moment  $q\alpha_0^2/4Q$   
Versus Dimensionless Time  $\beta_0 t$ . Composite  
for all ACORN Computations.

#### 4. INITIATION MECHANISMS

Because of mounting evidence that the majority of spacecraft dielectric discharges in space occur for low differential voltages [Stevens, 1980], it was decided to expend the majority of effort for this task investigating the effects of internal charge distribution. The results of this investigation were published. This paper, [Beers et al., 1981] reproduced here as Appendix 4, adequately discusses the effort and may be referred to for details. It is believed the results demonstrate that the internal charge distribution has an important bearing on the occurrence of discharge.

The behavior of avalanching and streamer formation as a function of the manifold material parameters follows from the computed results of section 3. Local field enhancement increases the probability of occurrence, as does a decrease in scattering probability. The quantitative change is provided by the computed results. No quantification of the decrease in scattering probability near various defects has been given. Field enhancement due to the internal charge distribution has been given in Appendix 4. Field enhancement near defects has not been quantified.

During the course of the research, it was noted that the classical literature on thermal breakdown failed to account for field distortion in the medium. A proper formulation of the problem was developed to account for the effect. A brief account of this work was published [O'Dwyer and Beers, 1980] and is reproduced herein as Appendix 5. The inclusion of space-charge distortion does not change the fact that thermal breakdown is a high temperature phenomenon. Consequently it is of little interest to the spacecraft discharge problem.

The overall conclusions from the initiation mechanisms study are that the conditions in space are conducive to low differential voltage breakdown and that buried charge is probably involved.

## 5. QUENCHING AND BLOWOFF MECHANISMS

Laboratory charging of spacecraft dielectrics with electron beams has led to an extensive data base on the subsequent breakdown. Two features of the observed process are: (i) the amount of charge cleaned off in the process is approximately proportional to the area of the sample [Balmain, 1979] for sample sizes up to  $1 \text{ m}^2$ ; and, (ii) the discharges are almost always accompanied by the release of electrons from the front of the dielectric into the vacuum. The electrons released quickly escape to the experiment chamber wall and manifest themselves as a return current to the sample substrate. The magnitude of these blowoff currents is large, involving as much as 50% of the total charge released there (the remainder existing via other current paths). In addition, the peak current scales approximately with a characteristic dimension of the sample [Balmain, 1979]. The first of these observations is normally called surface cleanoff. The second is described as the blowoff current. Certain theoretical aspects of these two phenomena are discussed below.

The fact that laboratory discharges appear to involve charge from most of the sample surface suggests that once a discharge has initiated, it is self-sustaining, and does not cease until the source of energy for the process (within the field due to the trapped charge) has been relaxed. It is of interest to ascertain whether the negative tip streamer described by ACORN has properties which are consistent with this behavior.

Before addressing this subject, it should be remembered that the negative streamer is not envisioned to be the discharge. Rather, a Markovian sequence of small streamers, initiated near the positive ends, is expected to provide the mechanism for discharge and propagation. Because a precise mathematical formulation of this process has not yet been given, the discussion of the quenching of the discharge given below must be viewed as speculative. Explicitly, the discussion is concerned with possible quenching mechanisms for the negative tip streamer described by ACORN. A conclusion

about the behavior of the negative streamer can become a conclusion about the behavior of the entire discharge only if it is the quenching behavior of the negative streamer which controls the propagation. If there are slower processes which control the stochastic initiation of subsequent streamers, then the above conclusion does not follow. Of course, if any mechanism exists which tends to quench the streamer itself, it does follow that the entire process is quenched.

Within a streamer, there are a number of processes which could be expected to lead to a quenching of the propagation. These processes are: diffusion, trapping, recombination, encountering a region of field reversal, encountering a macroscopic or microscopic material boundary, and global field decay. Each of these mechanisms is discussed in turn.

Diffusion is already incorporated into the numerical model implemented in ACORN. With the inclusion of this effect, an avalanche appears to evolve into a propagating, self-sustaining, ionization front. While the effects of avalanche are smeared out due to diffusion, the effect does not appear to lead to any mechanism which would stop the avalanche process.

Trapping is not expected to be a viable mechanism for quenching the avalanche process. Shown in Figure 5.1 are the ionization times for all the models which have been considered in earlier sections of the text. Typical trapping times are of the order of  $10^{-8}$  sec. [Hayashi, et al., 1975] or more, depending on whether shallow or deep trapping is considered. Thus, in order for trapping to be a competing mechanism with avalanche, the avalanche times must increase to values which are as large as the trapping time. From the figure, it is seen that this occurs for much smaller fields than those of interest. In fact, one may turn the argument around. If trapping times are sufficiently small as to compete with avalanche, then the avalanche will not initiate at all. Once it initiates trapping cannot be of concern.

This conclusion may be reached from a slightly different viewpoint. It was seen in earlier sections that once an avalanche initiates, it quickly



ORIGINAL PAGE IS  
OF POOR QUALITY

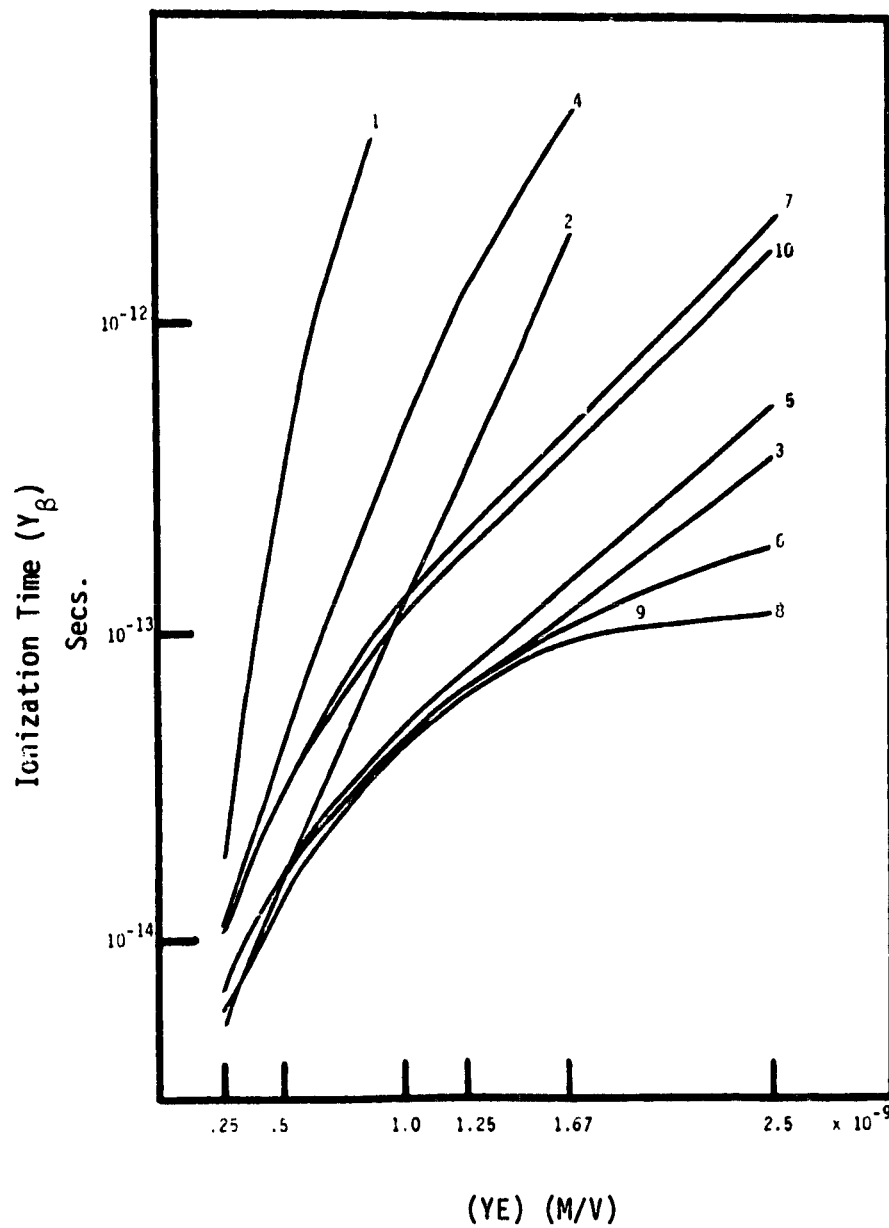


Figure 5.1. Ionization Time Versus Inverse of Electric Field for each of the ACORN Models of Table 3.1.1.

reaches a critical charge density given by  $\rho_c = \epsilon F_0 \alpha_0$ . Assuming no cancellation by positive charge, a purely negative charge leads to a critical number density  $N_c = \epsilon F_0 \alpha_0 / e$ . Shown in Figure 5.2 is a plot of this quantity for all the models considered in earlier sections. Typical trap densities are of the order of  $10^{15}/\text{cm}^3$ , with a maximum of perhaps  $10^{17}/\text{cm}^3$ . With the densities shown in Figure 5.2, it is clear that even if the trapping rate were very fast, all traps would quickly fill, and there would still be adequate charge in the conduction band to continue the avalanche process.

Recombination is somewhat more difficult to quantify. There are several reasons for this. The first is that recombination with the parent atom (so-called geminate recombination of Onsager [1938]) is somewhat difficult to observe. Second, most observations of recombination have been performed for relatively small carrier concentrations ( $\ll 10^{15}/\text{cm}^3$ ). In this regime, recombination is dominated by trapping processes. That is, recombination occurs between a mobile electron and a trapped hole, or vice versa. This trap controlled recombination tends to give rise to a kinetic theory term which is linear in the mobile electron density. At higher carrier densities, typical of those noted above, direct two body recombination is expected to dominate (the kinetic theory term is proportional to the product of the mobile electron and hole densities and increases quadratically with the carrier density). It is possible at the very high densities associated with Figure 3.2, that even higher order processes may become important. This has been observed in high dose irradiations of semi-conductors [Van Lint, et al., 1980]. Finally, all the recombination processes are sensitive to the electron distribution function. For the high fields considered, significant distortion of the distribution function takes place. This shift to a heated electron distribution function tends to make recombination less likely.

Even with all these caveats, it is probably still safe to say that recombination will not quench an avalanche once initiated. Assuming a term in the rate equation of the form  $r \cdot n \cdot m$ , where  $r$  is a rate per unit density,  $n$  is the mobile electron density, and  $m$  is some hole density (whether trapped or

ORIGINAL PAGE 18  
OF POOR QUALITY

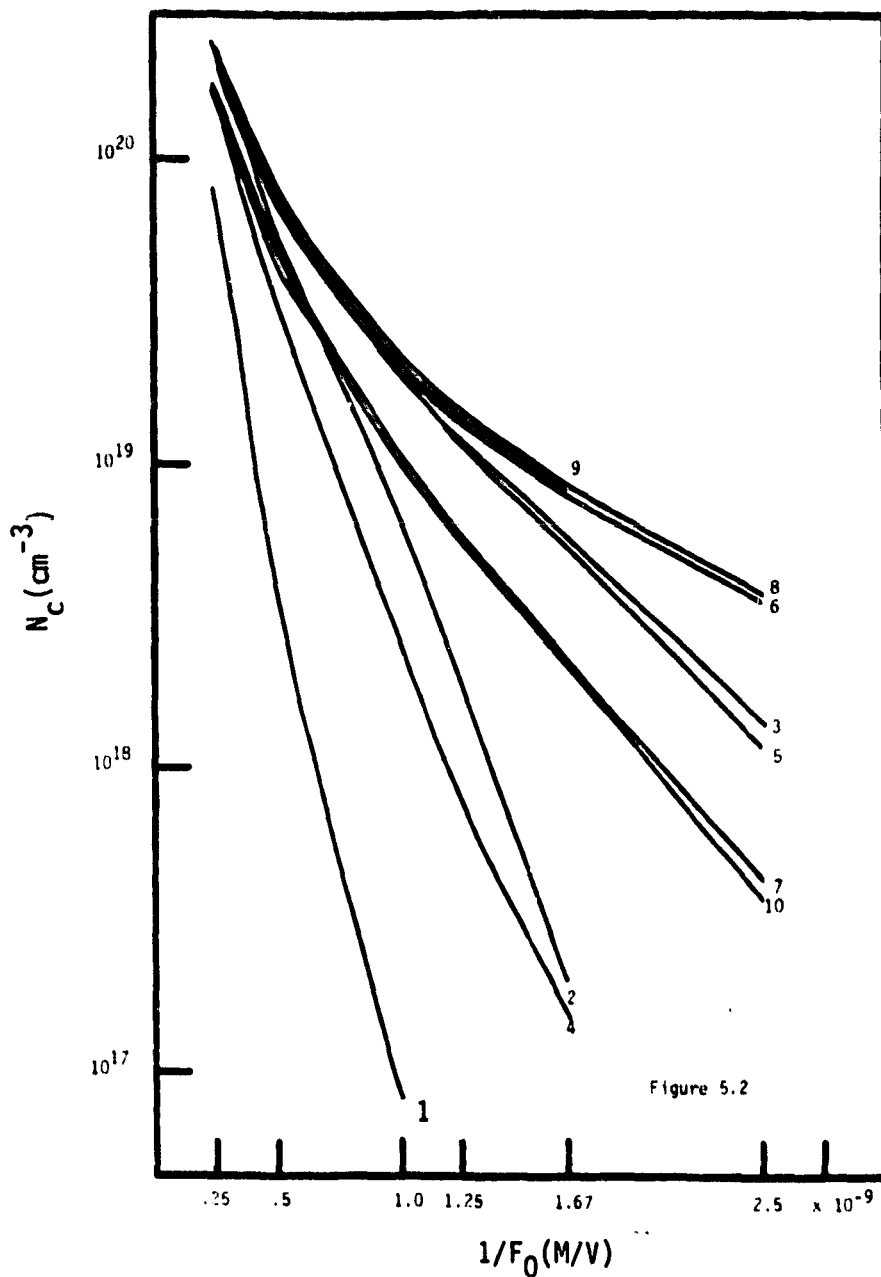


Figure 5.2. Critical Number Density  $N_c$  Versus Inverse of Ambient Electric Field. See text for definition of  $N_c$ . Numbered curves refer to material models defined in Table 3.1.1.

free), the rate  $r$  is related to a capture cross-section  $\sigma$  through a formula  $r = \langle \sigma v \rangle$ , where  $\langle \rangle$  indicates an ensemble average, and  $v$  is the electronic velocity. The largest quoted value for  $\sigma$  [A. Rose, 1963] is of the order  $10^{-13} \text{ cm}^2$ . This large value of the cross-section occurs at very low energies. At higher energies,  $\sigma$  falls off rapidly. The maximum value for the recombination rate  $r$  occurs at low energy. For electrons of near thermal velocity at room temperature, the mean speed is about  $10^7 \text{ cm/sec}$ . With these estimates of  $\sigma$  and  $v$ , the recombination rate has a maximum value of  $10^{-6} \text{ cm}^3/\text{sec}$ . Assuming a hole density of  $10^{18}/\text{cm}^3$ , gives a minimum recombination time of  $10^{-12} \text{ sec}$ . Even this worst case estimate gives a time which is larger than the characteristic avalanche times as noted in Figure 5.1. In practice, it is expected that the maximum recombination time is substantially larger. For example Gross [1978] quotes a value of  $r = 10^{-8} \text{ cm}^3/\text{sec}$  for Teflon.

Therefore recombination cannot quench the processes which are occurring in the active region of the avalanche, the ionization front. Once initiated, it will continue. In the body of the streamer, however, it might be possible for recombination to reduce the conductivity. In this region, the field drops substantially from ambient levels, and there are significant free carrier densities present. If nothing further happened, except for the propagation of the single ionization front, then the recombination process will take over and decrease the free carrier concentration. Further quantification of the importance of this process requires a precise formulation of the discharge in terms of a succession of small streamers.

The question of whether a region of field reversal will impact the negative streamer formation has a straightforward answer. It is topologically impossible for the field reversal region to impact the evolution once initiated. The reader is referred to Figure 3 of Appendix 4 which shows the field configuration near the front surface of a dielectric irradiated by a space-like electron environment. It explicitly shows the field reversal of the postulated mechanism [Meulenbergh, 1976]. To the right of the zero of the field, the electric field intensity is negative. Electrons and subsequent

streamers in this region will therefore drift to the right and never encounter the zero crossing. Similarly, to the left of crossing, the field is positive and electrons and streamers will move to the left in this region and never encounter the zero crossing. The point is simple. Electrons are trying to escape the region of trapped electron density. There is no way to configure the boundary conditions so that drifting electrons will encounter a region of field reversal.

The most difficult processes to quantify are those associated with encountering a physical boundary, whether macroscopic or microscopic. For this reason, the following discussion is primarily intuitive and heuristic. Clearly if the negative streamer encounters a conductor, then the avalanching process will cease. Subsequently, the region of space which has been left with mobile carriers will rearrange itself so that the surface of this region is equipotential with the conductor which was encountered. For the conductivities computed in Section 3, this happens very rapidly,  $\sim 10^{-13}$  sec. The primary process has been stopped, but the net effect has been to project an "effective" needle-like conductor into the dielectric. Assuming the potential has been maintained, and the positive tip is nearer the cathode, the field continues to be enhanced at the positive tip. If nothing further happens, the process has ended. A repetition of the avalanche mechanism must be invoked for further spreading of the process. Further statements must await a formulation of this mechanism of breakdown.

On reaching a vacuum boundary, it is also clear that the avalanching process must cease. The disposition of the avalanching electron front thereafter is not quite so clear. Two things could happen. The front could reach the surface and encounter a potential barrier which stops the electrons at the surface. Alternatively, the potential barrier could be sufficiently small that the electrons are energetic enough to penetrate the barrier and escape to free space. Of course, the experimental evidence suggests that the latter occurs. Theoretical arguments to support this conclusion are more difficult to muster. The electrons have at most a few eV of energy above the

conduction band edge of the solid. The relevant barrier is that of the work function, or electron affinity. It typically has a value much less than the work function of metals. Values of 1-2 eV at most may be expected. The major uncertainty concerns the effect of the deeply trapped space charge (the internal electric field) on this value. It is not absolutely apparent that all aspects of this field have been accounted for by merely computing the bulk electronic distribution function in the field. Indeed enhanced secondary emission of charged dielectrics has been reported from time to time suggesting that some lowering of the work function barrier may occur.

In any case, the barrier is at most about the same energy as a characteristic energy of the bulk electron distribution function. One therefore expects a significant fraction of the electrons in the front to escape. The exact escape ratio depends on the details of the distribution function and the electron affinity. A detailed formulation and calculation is outside the scope of this effort.

The effect of the above is that the avalanche ceases, a short burst of electrons is emitted into the vacuum, and an enhanced field conducting region is left behind. Further evolution depends on a succession mechanism for avalanches.

The effects of microscopic discontinuities have not yet been investigated.

The dependence of the solutions on global field decay follows from the discussion of Section 3 and the trapping and recombination discussion of this section. From the scaling laws of Section 3, the characteristic time for avalanching is  $\beta_0^{-1}$ . The quantity increases exponentially with a decrease in field. If sufficient charge has been released so that the bulk field is decreased significantly below the initiation field, then the trapping and recombination times can begin to dominate, thus providing the required quenching. It should be mentioned that an exact quantitative relation cannot be given

within the present format for the field at which this occurs. As the field decreases, and trapping and recombination become dominant, the assumptions which were used to solve the transport equation for electrons become invalid. That is, it was explicitly assumed in the formulation that the field was sufficiently large that the quasi-free electron approximation could be used. Transitions to localized states were to be treated as a perturbation. The limit of interest requires that trapping and recombination become dominant. In this limit, it is the conduction band motion which is a perturbation on the trapped states (sometimes called hopping conduction, or trap modulated drift). The effect is that significant ionization shuts off even faster than implied by the exponential behavior. What remains clear is that this mechanism will turn off the discharge, but only after a significant fraction of the charge has been lost from the insulator.

A review of the paper by Leadon and Wilkenfeld [1978] leads to the belief that magnetic forces are probably not important in the blowoff process. A review of the numerical values presented therein is sufficient to come to this conclusion. In order to obtain a magnetic force even remotely close to the ambient electric field, the following parameters were chosen; electron drift velocity in the dielectric,  $10^9$  cm/sec; peak discharge current,  $6 \times 10^3$  Amps, and distance from punch through channel,  $10^{-3}$  meters. With these parameters, the electric field equivalent of the force is  $10^5$  V/cm.

These values are probably not appropriate. The drift velocity used is approximately two orders of magnitude too high when compared to those computed from SEMC, and measured under a very wide variety of conditions. The discharge time (10 ns) assumed is significantly shorter than observed for the assumed sample size (10 cm). A value closer to  $10^3$  ns [Balmain and Hirt, 1980] is more reasonable. Thus, the assumed peak current is probably two orders of magnitude too high. Finally, the magnetic force falls off inversely with the distance from the discharge channel, so that 1 cm from the channel, the force is reduced another order of magnitude. Since it is impossible to emit the amount of the blowoff current which has been measured ( $\sim 50$  A) for samples of this size from a spot  $10^{-3}$  m in radius (see discussion below about space-charge

limiting), it is necessary to look at larger distances from the punch-through. These considerations imply that the importance of the effect is an estimate of at least five orders of magnitude too high for the example presented. It is concluded that the mechanism is unimportant.

More generally, if these forces were important, then their effect would be strongly dependent on sample size (since the discharge current is). It is difficult to conceive of circumstances which would allow the scaling of this force (it decreases with current) in such a fashion as to always dominate the electric field force. More generally, magnetic forces are seldom of importance in transport processes unless both electric fields are shorted and inertial effects dominate.

Two other mechanisms can be envisioned for the blowoff process. The first of these is the termination of an avalanche at the surface, or, more generally, the punch through of a discharge to the surface, with the subsequent emission of electrons. It is important to distinguish between large scale or macro-discharges and small scale or micro-discharges in considering this mechanism. While it is possible that this mechanism is important for micro-discharges, it seems very unlikely that it is responsible for macro-discharges.

The reasoning is based on space-charge limiting. The large discharges which have been observed cannot possibly have been emitted from a small area characteristic of a surface punch through. Under space-charge limited emission conditions, the maximum current which can flow ( $I$ ) for an applied voltage drop  $V$  is given by the Langmuir-Child law  $I = GV^{3/2}$  where  $G$  is the perveance of the emitting system. For the purposes here, a detailed discussion of  $G$  is not required. Instead, we assume a  $10\text{ cm}^2$  sample which has a grounded grid  $10\text{ cm}$  from the front surface of the dielectric. The perveance in this case is  $G = 33\text{ mA cm}^{-2}\text{ kV}^{-3/2}$ . For a  $20\text{ kV}$  potential drop, this gives a maximum space charge limited current of  $30\text{ Amps}$ . This estimate is based on the assumption of uniform emission from the entire surface. The total allowed



current will scale roughly as the actual emitting area. Thus, a small punch through with an area of  $10^{-2} \text{ cm}^2$  (which is large for a punch through), can emit nearly four orders of magnitude less current than is observed. We do not pursue the quantitative aspects of this line of thought further. It is apparent that a few small punch through channels cannot emit enough current to account for the observations of current scaling for macro-discharges.

By contrast, micro-discharges with very small total blowoff currents could be sustained by this very same mechanism. A surface directed avalanche/streamer can arrive at the surface, and the free electrons can be ejected from the surface. This was discussed earlier in this section. It seems quite likely that this type of small scale charge emission occurs routinely in charged dielectrics. The details of this mechanism should be developed for describing small scale scintillation (probably without damage) of charged spacecraft dielectrics.

The final mechanism which has been considered is the diffusion and release of free electrons generated in a subsurface propagating arc discharge. The idea is quite simple. Based on the conceptual model of a stochastic sequence of avalanches, it is expected that streamers of the type described by ACORN will propagate through the subsurface trapped charge layer, with the direction of propagation parallel to surface. Evidence of this type of subsurface propagation has been given by Balmain [1979] from observing damage paths in the material subsequent to breakdown. These discharge channels are expected to branch out into a tree, which is similar in form to the damage patterns. Filamentary processes are therefore expected to lie under the entire surface area.

Each of the filaments may be described by a conducting channel of the type computed by ACORN. In these channels, a large density (see Figure 5.2) of free electron carriers is generated. These electrons will diffuse outward away from the channel and a portion of them will further drift to the surface, where they will subsequently escape.

It is to be determined whether this mechanism is quantitatively reasonable. The mechanisms which could prevent the electrons from reaching

the surface are trapping and recombination. Because the holes are relatively immobile, and the diffusion is away from the regions of large concentrations of holes, recombination is not expected to be important. Trapping is included in the following estimate.

Assume that a quantity  $n_0/\text{cm}^2$  electrons are released at depth  $d$  below the surface in a planar configuration. The process of escape to the surface may then be followed with elementary diffusion in the presence of absorption (trapping). Let  $\tau$  be the time constant for trapping, and  $D$  be the diffusion coefficient. Define a characteristic distance  $L$  by the equation

$$L = \sqrt{D\tau} \quad (5.1)$$

For each electron released at a depth  $d$  below the surface, the fraction  $(n/n_0)$  which reach the surface is

$$\frac{n}{n_0} = \exp \left[ -\frac{d}{L} \right] \quad (5.2)$$

Some numbers are instructive. From the high field computations of Section 3.1,  $D$  has a value of about  $10^{-4} \text{ m}^2/\text{sec}$ . Assuming a trapping time of  $10^{-8} \text{ secs}$  [Hayashi et al., 1975] gives a characteristic length of  $10^{-6} \text{ meters}$ . Typical depths of the charge layer are a few microns, so that the exponential in Equation (5.2) is not extremely small. Since a copious supply of electrons will be generated in the discharge channels, the fraction reaching the surface will be more than adequate to account for the observed amount of charge released in the discharge.

The time  $T$  required for electrons released a distance  $d$  below the surface to reach the surface is given by

$$T = d^2/D \quad (5.3)$$

Choosing  $d = 10^{-6}$  m gives  $T = 10^{-8}$  secs. Compared to the time scales of macro-discharges, this is quite fast. The rate of formation of discharge channels (which would control the release rate of diffusing electrons) would therefore control the current reaching the surface. The model is consistent with the blowoff current having the same pulse shape as the propagating subsurface current. The scaling with area, which has been observed, is consistent with this process if the subsurface discharge has the anticipated scaling behavior (peak current proportional to length).

The conclusion is that diffusion to the surface of electrons freed from a subsurface discharge is a very likely mechanism for the blowoff current production. Note that emission is expected over most of the surface area in this mechanism. The released current is not so severely limited by space-charge considerations, and is comparable with observations.

## 6. SUMMARY

A description of continuing work on the development of a detailed model of arc discharge dynamics has been given. The work described is centered around an extensive parameter study which was performed with the SEMC/CASCAD/ACORN family of computer codes. The salient results of this effort are summarized as follows:

- Code modifications were incorporated into the SEMC/CASCAD/ACORN family which permit reasonable code to code interface. Adequate output routines were also included in the package.
- Dimensional analysis and an extensive computational study with the SEMC code have provided a characterization of the single electron distribution function and associated transport coefficients over a wide range of material models.
- Analytical approximations for single electron induced undistorted avalanches were compared to an extensive set of computations of the same phenomenon using the CASCAD code. The problem parameters were those obtained from SEMC computations. It was noted that self-fields become important when only a small number of particles are involved in the avalanche. The transition to a continuum description for the self-consistent further evolution must therefore be interpreted as an ensemble averaged description.
- An extensive series of computations of the self-consistent evolution of electron avalanche/streamer formation suggests that this evolution can be described by a self-similar solution of the macroscopic equations. The scaling dependence of the solutions on almost all of the parameters has been given.

- A model for low voltage differential breakdown in dielectrics was given. The electrons from the environment penetrate the dielectric and give rise to a trapped charge layer in the dielectric. This layer gives rise to large internal electric fields near the surface which cannot be reduced by enhanced secondary emission. These fields can become large enough to induce breakdown. The space environment gives rise to the field configuration of the proposed mechanism. This is in strong contrast to monoenergetic laboratory simulations.
- The likely quenching mechanisms for terminating a discharge appear to be associated with encountering a vacuum boundary and/or global field collapse due to a release of sufficient charge.
- The most likely mechanism for large blowoff current appears to be diffusion to the surface of free carriers released in a subsurface discharge.

## REFERENCES

- Abramowitz, M. and Segun, J.A., Editors, Handbook of Mathematical Functions, Dover Publications, Inc., New York, New York, 1968.
- Balmain, K.G. and Hirt, W., Dielectric Surface Discharges: Dependence on Incident Electron Flux, *IEEE Transactions on Nuclear Science*, NS-27, 6, 1770, 1980.
- Balmain, K.G., Surface Discharge Arc Propagation and Damage of Spacecraft Dielectrics, Proceedings of the E.S.A. Symposium on Spacecraft Materials, December 1979.
- Balmain, K.G. and Dubois, G.R., Surface Discharges on Teflon, Mylar and Kapton, *IEEE Transactions on Nuclear Science*, NS-26, 5146, 1979.
- Baraff, G.A., Distribution Functions and Ionization Rates for Hot Electrons in Semiconductors, *Physical Review*, 128, 2507, 1962.
- Bates, D.R., Editor, Atomic and Molecular Processes, Academic Press, New York 1962.
- Beers, B.L., Pine, V.W., and Ives, S.T., Internal Breakdown of Charged Spacecraft Dielectrics, *IEEE Transactions on Nuclear Science*, NS-28, 6, 4529, 1981.
- Beers, B.L., Pine, V.W. and Ives, S.T., Theoretical Properties of Streamers in Solid Dielectrics, 1981 Annual Report, Conference on Electrical Insulation and Dielectric Phenomena, IEEE Electrical Insulation Society, 1981.
- Beers, B.L., Pine, V.W., Hwang, H.C., Bloomberg, H.W., Lin, D.L., Schmidt, M.J. and Strickland, D.J., First Principles Numerical Model of Avalanche-Induced Arc Discharges in Electron-Irradiated Spacecraft Dielectrics, NASA Final Report, Science Applications, Inc., Report No. SAI-102-79-002.
- Davis, H.T., Introduction to Nonlinear Differential and Integral Equations, by Dover Publications, Inc., New York, New York, 1962.
- Gross, B., Charge Storage and Transport in Solid Dielectrics, paper presented at Conference on Electrical Insulation and Dielectric Phenomena, IEEE Electrical Insulation Society, 1978.
- Hayashi, K., Yoshino, K. and Inuishi, Y., *Japanese Journal of Applied Physics*, 14, 39, 1975.
- Landau, L.D. and Lifshitz, F.M., Fluid Mechanics, Addison-Wesley, Reading, Massachusetts, 1959.
- Leadon, R. and Wilkenfeld, J., Model for Breakdown Process in Dielectric Discharges, paper presented in Spacecraft Charging Technology - 1978, NASA Conference Publication 2071, AFGL-TR-79-0082.

Lin, D.L. and Beers, B.L., Stochastic Treatment of Electron Multiplication Without Scattering in Dielectrics, *Journal of Applied Physics*, 52, 5, 3575, May 1981.

Lin, D.L., Electron Multiplication in Solids, *Physical Review*, B20, 5238, 1979.

Meulenbergh, Jr., A., Evidence for a New Discharge Mechanism for Dielectrics in a Plasma, in Spacecraft Charging by Magnetospheric Plasmas, *Progress in Astronautics Aeronautics*, A. Rosen, Editor, 47, 237, 1976.

Onsager, L., Initial Recombination of Ions, *Physical Review*, 54, 554, 1938.

Pine, V.W., Operational Aspects of the Computer Codes: SEMC, CASCAD AND ACORN, NASA Report, Beers Associates, Inc., Report No. NAS3-22530, August 1981.

Rose, A., Concepts in Photoconductivity and Allied Problems, John Wiley & Sons, New York, 1963.

Stevens, N.J., Analytical Modeling of Satellites in Geosynchronous Environment, in Spacecraft Charging Technology - 1980, NASA Conference Publication 2181, AFGL-TR-81-0270.

Thom, R., Structural Stability and Morphogenesis, translation by D.H. Fowler, Benjamin, Reading, Massachusetts, 1975.

Van Lint, V.A.J., Flanagan, T.M., Leadon, R.E., Naber, J.A. and Rogers, V.C., Mechanisms of Radiation Effects in Electronic Materials, Volume 1, John Wiley & Sons, New York, 1980.

## A P P E N D I X 1

Reproduced From:

Lin, D.L., Electron Multiplication in Solids, Physical Review  
B20, 5238, 1979



ORIGINAL PAGE IS  
OF POOR QUALITY

## Electron multiplication in solids

Dong L. Lin

Science Applications Incorporated, 8330 Old Courthouse Road, Suite 510, Vienna, Virginia 22180

(Received 9 July 1979)

Treating collisions as Markov processes, a theory is developed for the calculation of electron multiplication in solids. The electron mean free paths for acoustic-phonon scattering, optical-phonon emission, and pair production processes are assumed to be independent of the energy of the electron. The number of ionization events per mean free path is a universal function of dimensionless energy ratios. Several types of phonon scatterings are studied. In the case of isotropic scattering, comparison of the present work with the results obtained by numerically solving the Boltzmann equation indicates that good agreement is found only in fast-multiplication cases. The discrepancy noted in slow-multiplication cases is believed to be due to either the less stringent requirements or the mild singularity of the transition probabilities in the numerical approach to solving the Boltzmann equation.

### 1. INTRODUCTION

Under the stress of a very strong electric field, semiconductors and dielectrics tend to exhibit avalanche breakdown. A quantitative measurement of the charge multiplication in  $p$ - $n$  junctions of Si and Ge was carried out and its implication on the ionization rate per unit length, as a function of the applied electric field, was analyzed two decades ago.<sup>1</sup> The fundamental processes for charge multiplication in solids were assumed to be analogous to that (Townsend's  $\beta$  mechanism<sup>2</sup>) of gas discharge. The ionization rate is an important parameter which brings out the details of the microscopic solid-state properties from the macroscopic characteristics of breakdown measurements. Methods have been developed to calculate this parameter, most of them involving the solution of the Boltzmann equation in a high electric field. Thus, neglecting the then-unknown band structure of silicon, Wolff<sup>3</sup> expanded the electron distribution function in terms of Legendre polynomials, kept the first two terms, and solved the Boltzmann equation in a steady state. Baraff<sup>4</sup> employed the concept of collision density and derived an integral equation by Laplace-transforming the Boltzmann equation which he then solved numerically. To solve the Boltzmann equation at high fields is generally difficult, as pointed out by Wannier.<sup>5</sup> On the other hand, Shockley<sup>6</sup> considered the collision processes as probabilistic processes with exponential probability distribution and, treating only the electrons which survive any collision, directly obtained the ionization rates in the low-field and high-field limits. Although the validity of some assumptions made by Shockley was questioned at that time, the concept of exponential probability is particularly attractive in its simplicity. It appears that for the calculation of

ionization rates, one may avoid solving the Boltzmann equation by treating all processes as Markov processes and following the motion of the electron in a completely stochastic way.

In this paper, we will address the calculation of ionization rates in semiconductors or dielectrics where band-structure details can be neglected. A strong electric field  $\mathcal{E}$  is applied to a thick slab of material. The electron whose track we will follow starts with zero energy in the conduction band. We assume that there are three energy ranges in each of which only one single-electron process is possible. Thus from zero to  $\hbar\omega$  (the energy of the only optical phonon), only acoustic-phonon scattering is possible; between  $\hbar\omega$  and  $E_i$  (the ionization threshold to produce an electron-hole pair), the electron can only emit the optical phonon, assuming no optical phonons to be present so that the absorption of optical phonons is negligible; above  $E_i$ , electron excitation from the valence band is the only interaction the electron has with its environment. We also assume that the mean free paths of these three fundamental processes are independent of the electron energy. Furthermore, these three mean free paths are assumed for simplicity to have the same value  $\lambda$ . These assumptions are in line with previous works.<sup>3,4,6</sup> Most of them can be relaxed if one so wishes; the involved modifications of the equations, to be derived below, either are trivial or can be carried out with minor effort.

The main quantity we are interested in is the mean ionization distance for an electron starting with zero kinetic energy at  $z = 0$  ( $z$  is the depth coordinate). An electron, emitting  $n$  optical phonons, will reach  $E_i$  at location  $z = (E_i + n\hbar\omega)/e\mathcal{E}$ . Since  $z$  and  $n$  are two random variables, the mean distance  $\bar{z}$  per mean free path is related to the mean number of optical-phonon emissions,  $\bar{n}$ , by

$$X = F_1 / e\delta\lambda + \bar{n}(\delta\lambda - e\delta\lambda) \quad (1)$$

Setting  $X = F_1 / e\delta\lambda$  and  $R = \delta\lambda - F_1$ , the mean number of electron-hole pairs produced by a single electron in traveling a mean free path  $\lambda$  is given by

$$N_{pair} = (V + \bar{n}R\lambda + 1)^{-1} \quad (2)$$

The 1 on the right-hand side takes care of the extra mean distance  $\lambda$ , the electron has to travel, after reaching  $F_1$  in order to produce a pair. The exact value of this extra mean distance is not important, but however. Here we assume  $\lambda_1 = \lambda$ .

Equation (2) indicates that  $N_{pair}$  is a universal function of  $X$  and  $R$  since  $\bar{n}$ , as will be shown later, depends only on  $X$  and  $R$ .

The concept described here could be applied to the calculation of the average energy of hot electrons emerging from a slab of given thickness  $z_0$ . The proper equation reads

$$F = e\delta z_0 - \bar{n}\hbar\omega \quad (3)$$

and  $\bar{n}$  could be obtained exactly in the same way, as described in Sec. II. The only change is to replace  $y = \Delta y$  in the arguments by  $y$ . Though Monte Carlo results<sup>7</sup> do exist, the suggested approach here gives an exact answer.

## II. THEORY

Let  $\lambda$  be the mean free path of a collision (a Markov process). The no-collision probability for an electron in traveling a distance  $z$  is  $e^{-z/\lambda}$  and the probability of one collision in  $dz$  is  $dz/\lambda$ . The mean collision distance is given by

$$\langle z \rangle = \int_0^\infty \frac{z e^{-z/\lambda} dz}{\lambda} = \lambda \quad (4)$$

the mean free path of this process.

At some reference level, an electron is released with both kinetic and potential energies zero. Under the influence of a constant electric field  $\delta$ , this electron behaves like a particle of some inertial mass in a gravitational field. Now, if this electron experiences an acoustic (elastic) collision, it simply adjusts the direction of its velocity with magnitude unchanged. If an optical-phonon emission occurs, the electron not only changes the velocity deflection but also loses some quantum kinetic energy (the quantum energy  $\hbar\omega$  of the optical phonon). Since in a conservative field, there is a one-to-one correspondence between kinetic energy and potential energy, once the reference level of zero potential is chosen, the fact that the electron loses  $\hbar\omega$  kinetic energy will be equivalent to pushing this electron a distance  $\hbar\omega/e\delta$  closer to the reference level, as shown in Fig. 1.

The probability of having a collision is controlled

by the exponential function of the length of the trajectory this electron travels after the latest collision.

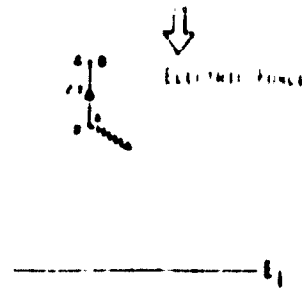


FIG. 1. Electron at A emits an optical phonon and its location is consequently put at B,  $\Delta z = \hbar\omega/e\delta\lambda$ .

by the exponential function of the length of the trajectory this electron travels after the latest collision.

For a Markov process, the history of the electron before a collision is completely wiped out when a collision occurs. In other words, the angular distribution of the cross section of a collision is independent of the direction of this incident electron. A few examples are in order:

(a) Forward scattering. The electron can only travel in the direction of the electric force. There is no elastic collision in this case because the direction is fixed.

(b) Two-direction scattering. The electron can move either along or against the electric field. Movement in either direction can cause collision with the consequence of, say, half chance of the electron going along and half chance of going against the electric field.

(c) Isotropic scattering. The cross section is isotropic and thus of Markov type.

In general, we can assume the angular distribution of the probability to be  $P(\theta)$  no matter what direction the electron is moving in immediately before a collision.  $\theta$  is the angle the velocity vector makes with the horizontal line as shown in Fig. 2. The electron is at a location  $y_1$  ( $y = z/\lambda$ ) below the reference level. Let  $T(y_1, y_1)dy_1$  be the probability distribution that the electron, suffering a collision at  $y_1$ , will not have any collision before reaching the height  $y_1$  below the reference level and having a collision in  $dy_1$  at  $y_1$ . The collision here could be acoustic or optical. This probability is computable from classical mechanics, as can be done

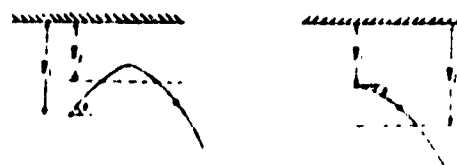


FIG. 2. Electron as a projectile.

following the results of the Appendix. It is easy to prove that  $\int_0^{v_0} T(v_2, v_1) M v_2 dv_2 = 1$  if one realizes that, for a given projectile angle, the probability of having a collision regardless of how far the electron travels is unity, i.e.,  $\int_0^{v_0} e^{-v_1/v_2} dv_2/v_2 = 1$ . Once  $P(\theta)$  is assigned and  $T(v_2, v_1)$  is computed, the ionization rate can be obtained as follows.

Let

$$N(v_1) = 1 - \int_0^{v_0} T(v_2, v_1) M v_2 dv_2 = \int_{v_0}^{\infty} T(v_2, v_1) dv_2$$

be the probability that an electron suffering a collision at  $v_1$  will not have any collision before reaching  $v_0$  ( $\sim X$ ), the ionization threshold for producing an electron-hole pair. Let  $\Delta v$  be the width of the acoustic-scattering region, i.e.,

$$\Delta v = c\delta\Delta z/c\delta\lambda = \hbar\omega/c\delta\lambda = RX.$$

We can then compute, by the technique of regrouping, the probability of having  $n$  optical-phonon emissions, regardless of the number of scatter-

ings due to acoustic phonons.

The electron released at zero kinetic energy at the potential reference level reaches  $v_1$  either without any collision or with at least one collision (acoustic or optical). In other words,

$$1 = N(0) + \int_0^{v_0} 1 \times T(v_1, 0) M v_1 dv_1. \quad (5)$$

After breaking up the integration limits into the acoustic and optical regions, the 1 on the right-hand side can be replaced by

$$N(v_1) + \int_0^{v_0} T(v_2, v_1) M v_2 dv_2$$

when  $v_1$  is in the acoustic scattering region, or by

$$N(v_1 - \Delta v) + \int_0^{v_0} T(v_2, v_1 - \Delta v) M v_2 dv_2$$

when  $v_1$  is in the optical emission region:

$$\begin{aligned} 1 = N(0) + \int_0^{v_0} N(v_1) T(v_1, 0) M v_1 dv_1 + \int_0^{v_0} dv_1 \int_0^{v_0} dv_2 T(v_2, v_1) T(v_1, 0) + \int_{\Delta v}^{v_0} dv_1 N(v_1 - \Delta v) T(v_1, 0) \\ + \int_{\Delta v}^{v_0} dv_1 \int_0^{v_0} dv_2 T(v_2, v_1 - \Delta v) T(v_1, 0). \end{aligned} \quad (6)$$

If  $(n_a, n_o)$  denotes the numbers of acoustic and optical scatterings, then the first term in Eq. (6) is  $(0, 0)$ , the second  $(1, 0)$ , and the fourth  $(0, 1)$ . For the third and the last, we need to break up the integration  $\int_0^{v_0}$  and then substitute the appropriate equation for 1 as before. This procedure could be repeated indefinitely. Collecting the terms with  $(n_a, 0)$  for  $n_a = 0, 1, 2, 3, \dots, \infty$  gives

$$\begin{aligned} N(0) + \int_0^{v_0} dv_1 N(v_1) T(v_1, 0) \\ + \int_0^{v_0} dv_1 \int_0^{v_0} dv_2 N(v_2) T(v_2, v_1) T(v_1, 0) + \dots \\ = N(0) + \int_0^{v_0} dv_1 \tilde{N}(v_1) T(v_1, 0) = \tilde{N}(0), \end{aligned} \quad (7)$$

where  $\tilde{N}(v_1)$  satisfies the following inhomogeneous integral equation of the second kind:

$$\tilde{N}(v_1) = N(v_1) + \int_0^{v_0} dv_2 \tilde{N}(v_2) T(v_2, v_1). \quad (8)$$

We can interpret  $\tilde{N}(v)$  as the renormalized (by interaction with acoustic phonons) version of the

bare quantity  $N(v)$ .

For one optical-phonon emission, all the terms of the type  $(n_a, 1)$ ,  $n_a = 0, 1, 2, \dots$  need to be collected and regrouped. After two regroupings and one relabeling, the probability of one optical emission is given by

$$\int_{\Delta v}^{v_0} dv_1 \tilde{N}(v_1 - \Delta v) \tilde{T}(v_1, 0), \quad (9)$$

where  $\tilde{T}(v_2, v_1)$  also satisfies an integral equation,

$$\tilde{T}(v_2, v_1) = T(v_2, v_1) + \int_0^{v_0} dv_3 T(v_2, v_3) \tilde{T}(v_3, v_1). \quad (10)$$

Again, due to the presence of the acoustic-scattering region, the bare transition probability density  $T(v_2, v_1)$  is renormalized to  $\tilde{T}(v_2, v_1)$ .

A similar procedure leads to the following probability for two optical-phonon emissions,

$$\int_{\Delta v}^{v_0} dv_1 \int_{\Delta v}^{v_0} dv_2 \tilde{N}(v_1 - \Delta v) \tilde{T}(v_2, v_1 - \Delta v) \tilde{T}(v_1, 0). \quad (11)$$

The rule for writing the probability of any num-

ber of optical-phonon emissions can be obtained by examining Eq. (11).  $\hat{T}(y_1, 0)$  indicates that the electron is released at  $y = 0$ , making all possible interactions with the acoustic phonons, and reaches  $y_1$  in the optical emission region. Emitting an optical phonon at  $y_1$  and thereby changing its location to  $y_1 + \Delta y$ , the electron encounters all possible, including zero, numbers of acoustic-phonon scatterings before the next optical phonon emission at  $y_2$  in the optical emission region, as described by  $\hat{T}(y_2, y_1 + \Delta y)$ . The optical-phonon emission at  $y_2$  pushes the location of the electron to  $y_2 + \Delta y$ . Between this new position and the pair-

production threshold no optical emission occurs while any number of acoustic scatterings may take place. This is represented by  $\hat{N}(y_2 + \Delta y)$ . Reading equations like Eq. (11) is completely equivalent to describing the physical processes they represent.

It is guaranteed, from the way the above probabilities are derived, that the sum of all probabilities equals unity.

The average number of optical phonon emissions is given by the sum of the products of the number of optical phonons emitted and the corresponding probability.

$$\begin{aligned} n = & 0\hat{N}(0) + 1 \int_{-\infty}^0 dy_1 \hat{N}(y_1 - \Delta y) \hat{T}(y_1, 0) + 2 \int_{-\infty}^0 dy_1 \hat{N}(y_1 - \Delta y) \int_{-\infty}^0 dy_2 \hat{T}(y_2, y_1 - \Delta y) \hat{T}(y_2, 0) \\ & + 3 \int_{-\infty}^0 dy_1 \hat{N}(y_1 - \Delta y) \int_{-\infty}^0 dy_2 \hat{T}(y_2, y_1 - \Delta y) \int_{-\infty}^0 dy_3 \hat{T}(y_3, y_2 - \Delta y) \hat{T}(y_3, 0) + \dots \end{aligned} \quad (12)$$

Laying down the probabilities with weights (the number of phonons emitted) as in Fig. 3, and summing vertically for each column, one obtains a function  $G$  satisfying

$$G(y_1) = \hat{T}(y_1, 0) + \int_{-\infty}^0 dy_2 \hat{T}(y_2, y_1 - \Delta y) G(y_2) \quad (13)$$

for each column. When all the columns are summed, the final expression for the average number of optical-phonon emissions is given by

$$\bar{n} = \int_{-\infty}^0 dy \hat{N}(y - \Delta y) H(y), \quad (14)$$

where

$$H(y_1) = G(y_1) + \int_{-\infty}^0 dy_2 \hat{T}(y_2, y_1 - \Delta y) H(y_2). \quad (15)$$

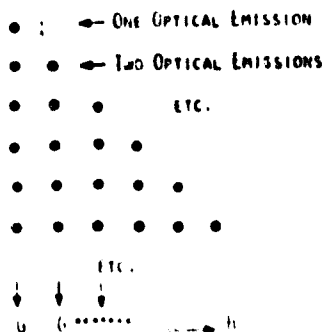


FIG. 3. Summing a column gives  $G$ . Summing all  $G$ 's gives  $H$ .

Equation (14) indicates  $\bar{n}$  is a function of  $y_0$ , which is equivalent to the energy ratio  $X \approx E_1 / e\delta\lambda$ , and  $\Delta y$ , another energy ratio,  $\Delta y / e\delta\lambda$  ( $\approx RX$ ). Given  $R$  and  $X$ ,  $\bar{N}_{opt}$  is uniquely determined by Eq. (2).

### III. RESULTS AND DISCUSSION

As mentioned in Sec. II, there are three interesting cases of scatterings: forward scattering, two-direction scattering, and isotropic scattering. The first case provides a check of the formulation described above against an algebraic approach to be published elsewhere.<sup>8</sup> The second case gives a hint of how the backward scattering (against the electric force) would change the mean ionization distance, while the complication of calculating the trajectory length is kept to a minimum. The third case is that of the real physical situation which has been discussed by others in the literature.

Case (1): forward scattering.

$$T(y_2, y_1) = \begin{cases} 0 & \text{for } y_2 < y_1 \text{ or } y_1 < y_2 < \Delta y \\ \exp[-(y_2 - \max(y_1, \Delta y))] & \text{otherwise.} \end{cases} \quad (16)$$

Backward scattering ( $y_2 < y_1$ ) is forbidden in this case. The  $N(y)$  corresponding to this transition probability is given by  $\exp[\max(y, \Delta y) - y_0]$ . Using the formulation of Sec. II, one obtains  $e^{RX} - 1$ , and  $e^{2RX} + (1 - RX)e^{RX} - 2$  for the average number of optical-phonon emissions in the respective cases of  $R = \frac{1}{2}$  and  $\frac{1}{4}$ . These results agree with that of the simple algebraic approach.<sup>8</sup> For smaller  $R$ 's

of the type  $1/(m+1)$  with integer  $m$ , numerical evaluations in a self-consistent way of the integral equations in Sec. II yield the same  $h$  as that of the algebraic solution.\* For the analytic confirmation of the equivalence of these two different approaches, a conjecture,  $h_{\text{iso}} = [K(m+1) - m]e^{m\Delta}$  for  $R=1$ ,  $(m+1)$ , needs to be proven; the  $h(y)$  is defined as  $H(y) = h(y)e^{y/\Delta}$  and  $h_{\text{iso}}$  is  $h(y)$  for  $m\Delta y \leq y \leq y_0$ . The definition of  $K(m)$  can be found in Ref. 8. That this conjecture is true for  $m=1$  and 2 has been checked.

Case (ii): two-direction scattering with equal probabilities.

$$T(y_2, y_1) = \frac{1}{2} \exp(-|y_2 - y_1|) + \frac{1}{2} \exp[-(y_1 + y_2)]. \quad (17)$$

$N(y) = e^{-y/\Delta} \cosh(y)$  in this case. Shown in Fig. 4 are the transition probabilities for various  $y_1$ . Note that an electron, after having a collision at a given location, may move against the external electric force (backward scattering) and have another collision somewhere upstream in the electric field, further delaying the time at which it will reach the ionization threshold. Consequently, the mean ionization distance for this case is somewhat longer than for case (i) above. In Fig. 5, the ionization events per mean free path ( $\bar{N}_{\text{pair}}$ ) of these two cases for  $R=0.05$  are compared in a semilog scale. The one-half chance to scatter backward does change  $\bar{N}_{\text{pair}}$  substantially for low electric fields (large  $E_1/e\Delta\lambda$ ).

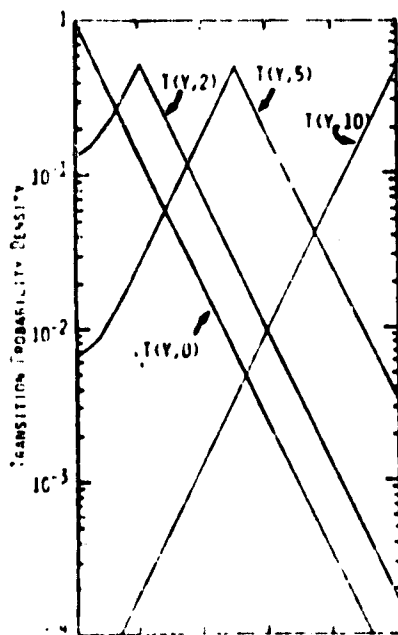


FIG. 4.  $T(y_2, y_1)$  for two-direction scattering with equal probabilities. Here  $\lambda = l_1/e\Delta = 10$ .

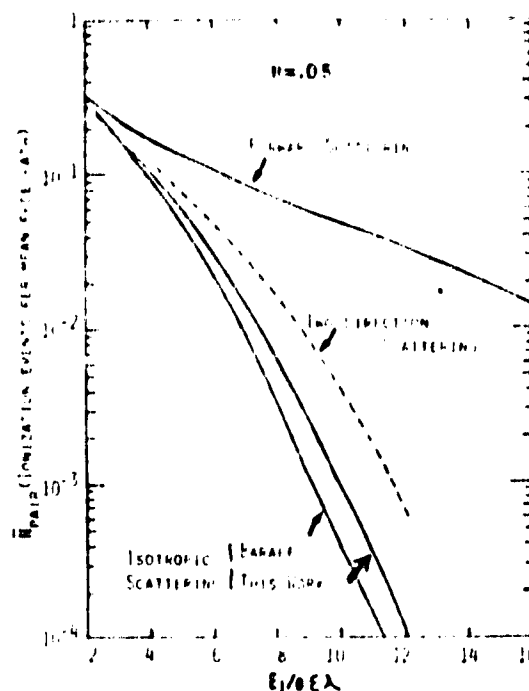


FIG. 5. Ionization events per mean free path for various types of scattering;  $R_0/E_1 = 0.05$ .

Case (iii): general scattering.

$$T(y_2, y_1) dy_2 = \frac{1}{2} \sum_{n=1}^R P(\theta) d(c^{-S_1(y_2, y_1, \theta)} + c^{-S_2(y_2, y_1, \theta)}) \quad (18)$$

The functions  $S_1(y_2, y_1, \theta)$  and  $S_2(y_2, y_1, \theta)$ , as can be found in the Appendix, are the arc lengths of the electron from  $y_1$  to the points on the trajectory at which the height is  $y_2$ .  $\theta$  is the projectile angle and  $P(\theta)$  the corresponding probability [ $P(\theta) = \text{const}$  for isotropic scattering]. Trivially,

$$N(y_1) = \frac{1}{2} \sum_{n=1}^R P(\theta) (c^{-S_1(y_0, y_1, \theta)} + c^{-S_2(y_0, y_1, \theta)}). \quad (19)$$

There are three important observations concerning Eq. (18). The first is that the angular integration appears as a multiplicative factor whereas in Baraff's formulation<sup>4</sup> it shows up in the exponent. The second is about the behavior of  $T(y_2, y_1)$  at some seemingly singular points. For example, at  $\cos^2 \theta = y_2/y_1$ , both terms on the right-hand side of Eq. (18) are divergent. They sum up to a finite value because  $S_1 = S_2$  when  $\cos^2 \theta = y_2/y_1$ . Another example is when  $\cos \theta = 0$  so that the denominator in the logarithmic function of  $S_2(y_2, y_1, \theta)$  in Eq. (A2) becomes zero. The  $\cos^2 \theta$  factor in front of this logarithmic function eliminates this

singular behavior. The good behavior of  $T(v_j, v_j)$  is sort of physically clear from the definition of  $T(v_j, v_j)$  itself: given a scattering at  $v_j$ , the probability of the next scattering within a strip  $dv_j$  at  $v_j$  should be finite because the segment of the trajectory inside this strip shrinks to zero at least as fast as  $dv_j$  does. Baraff's approximate expression for  $T$  does contain a singularity at  $v_j = v_j$ . The third observation involves the normalization of  $T(v_j, v_j)$ : Equation (1b) automatically satisfies the requirement of normalization because it is formulated in a purely probabilistic way.

An equivalent way of carrying out the calculations indicated in Sec. II is to actually compute the probability of  $m$  optical phonon emissions for  $m = 0, 1, 2, \dots$ . Once  $\bar{N}$  and  $\bar{T}$  are known, these probabilities are just simple integrals. The important advantage of this is to check and see if the sum of all probabilities equals unity, a very stringent constraint on the accuracy of both the most fundamental function  $T(v_j, v_j)$  itself and all the numerical procedures involved. In other words, once  $T(v_j, v_j)$  is set, a probability distribution is obtained which has to be summed up to unity to be correct. This requirement has been obeyed to guarantee the correctness of the computed results.

In actual calculations, a steady state will be reached, as correctly observed by Baraff,<sup>4</sup> in which the ratio of adjacent probabilities of emit-

ting  $m$  and  $m+1$  optical phonons approaches a constant. This constant, called  $\gamma$ , is strictly controlled by  $T(v_j, v_j)$  itself and may be computed by using either the eigenvalue method or iterative procedures. Using this constant, the probability at the onset of the steady state, and the sum of the probabilities before reaching the steady state, one can compute the total probability which should be unity if everything is right.

In Fig. 6 we show the probability distributions of case (ii) and case (iii) for  $R = 0.05$  and  $X = 6$ . The steady state is determined when the fractional change of the probability ratio  $\gamma$  is less than  $10^{-5}$  (in some cases  $10^{-6}$ ).

The result of the present work for the isotropic-scattering case is presented in Fig. 5 for  $R = 0.05$ . Also shown in the figure is a curve of Baraff for identical assumptions. The difference is about a factor of 2 at  $X = 10$  where, on the average, an ionization event occurs every thousand mean free paths (slow charge multiplication). The discrepancy gradually disappears as  $X$  is decreased. Comparison of Baraff's work and the present approach for  $R = 0.01$  shows excellent agreement for  $X$  from 2 to 14: the mean ionization distance in this case is generally less than 100 mean free paths (fast charge multiplication). It is noted that in the slow-multiplication cases the steady states always possess probability ratios very close to 1, i.e.,  $\gamma \approx 1$ . Since the equation for the mean ioni-

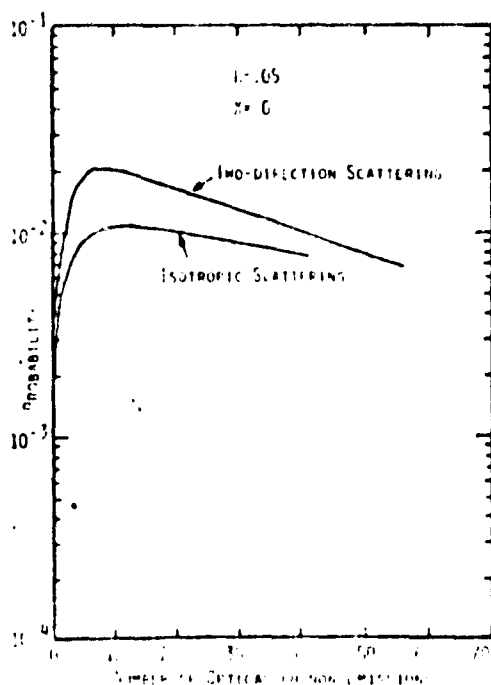


FIG. 6. Probability distributions of two different scattering functions for same  $R$  and  $X$ . The sum of each probability distribution equals unity.

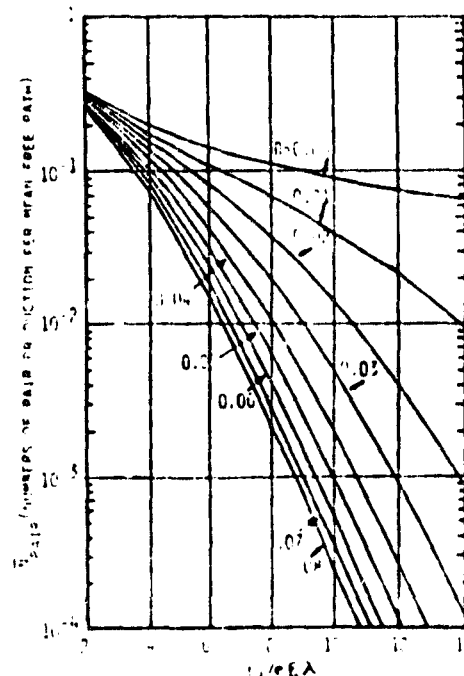


FIG. 7. Number of pairs produced per mean free path as a function of  $E_1/\epsilon E_A$  for various values of  $R = h\omega/E_1$ .

TABLE I.  $N_{\text{par}}$  for  $R=0.01-0.05$ . For  $R=0$ ,  $N_{\text{par}} = (1-\gamma)^{-1}$ ,  $n=h$  stands for  $\gamma = 10^{-h}$ .

| $R \backslash X$ | 1        | 2        | 3        | 4        | 5        | 6        | 7        | 8        | 9        | 10       | 11       | 12       | 13       | 14       |
|------------------|----------|----------|----------|----------|----------|----------|----------|----------|----------|----------|----------|----------|----------|----------|
| 0.01             | 4.0(-1)  | 3.27(-1) | 2.34(-1) | 1.76(-1) | 1.37(-1) | 1.09(-1) | 8.52(-2) | 6.66(-2) | 5.14(-2) | 3.96(-2) | 2.99(-2) | 2.19(-2) | 1.67(-2) | 1.00(-2) |
| 0.02             | 4.02(-1) | 3.11(-1) | 2.14(-1) | 1.54(-1) | 1.12(-1) | 7.95(-2) | 5.49(-2) | 3.63(-2) | 2.29(-2) | 1.37(-2) | 7.73(-3) | 4.11(-3) | 2.07(-3) | 9.96(-4) |
| 0.03             | 4.04(-1) | 3.05(-1) | 2.04(-1) | 1.35(-1) | 9.02(-2) | 5.75(-2) | 3.45(-2) | 1.93(-2) | 1.06(-2) | 4.96(-3) | 2.36(-3) | 9.13(-4) | 3.2(-4)  | 1.15(-4) |
| 0.04             | 4.05(-1) | 2.96(-1) | 1.90(-1) | 1.14(-1) | 7.27(-2) | 4.16(-2) | 2.20(-2) | 1.07(-2) | 4.76(-3) | 1.99(-2) | 7.57(-4) | 2.9(-4)  | 1.05(-4) | 3.5(-5)  |
| 0.05             | 4.01(-1) | 2.88(-1) | 1.77(-1) | 1.03(-1) | 5.89(-2) | 3.06(-2) | 1.45(-2) | 6.30(-3) | 2.56(-3) | 9.74(-4) | 3.57(-4) | 1.21(-4) | 4.42(-5) | 1.52(-5) |
| 0.06             | 4.02(-1) | 2.80(-1) | 1.66(-1) | 9.35(-2) | 4.82(-2) | 2.31(-2) | 1.00(-2) | 4.79(-3) | 1.92(-3) | 5.56(-4) | 1.96(-4) | 5.79(-5) | 2.02(-5) | 7.0(-6)  |
| 0.07             | 4.04(-1) | 2.72(-1) | 1.55(-1) | 8.29(-2) | 4.06(-2) | 1.79(-2) | 7.31(-3) | 2.79(-3) | 1.02(-3) | 3.59(-4) | 1.24(-4) | 3.61(-5) | 1.14(-5) | 4.02(-6) |
| 0.08             | 4.05(-1) | 2.64(-1) | 1.45(-1) | 7.37(-2) | 3.36(-2) | 1.43(-2) | 5.57(-3) | 2.65(-3) | 7.21(-4) | 2.54(-4) | 5.73(-5) | 2.55(-5) | 7.47(-6) | 1.97(-6) |

ization distance involves terms proportional to  $1/(1-\gamma)$  and  $1/(1-\gamma)^2$ , the result is very sensitive to  $1-\gamma$  when  $\gamma$  is near 1. The  $\gamma$  by the present calculation for  $R=0.05$  and  $X=10$ , for example, is 0.99951 and the sum of all probabilities is a satisfactory 1.0012.

The results of the calculations of  $N_{\text{par}}$  are shown in Fig. 7. Table I gives the computed values. The agreement between these results and Baraff's work is generally better for large  $N_{\text{par}}$  (fast multiplication) than for small  $N_{\text{par}}$  (slow multiplication). As described above, this may be due to the different requirements in getting  $\gamma$ 's or the mild singularity in Baraff's expression of the approximate transition probability density  $T(E_p, E_p)$ . The overall agreement is considered good in viewing the very different approaches used.

Shockley's  $N_{\text{par}}$  for the high-field limit conceptually corresponds to our  $h=0$ . In his simple model, the high-field limit corresponds to the case of very hot electrons whose energies are always greater than  $E_p$ . In our model, those hot electrons cannot produce any optical phonon, thus  $h=0$ . The argument for obtaining low-field limit in his model is not applicable to the special situation of  $\lambda_p/\lambda=0$ . Even if we choose  $\lambda_p/\lambda=1$ , the formula for  $N_{\text{par}}$  in this simple model reads  $N_{\text{par}} = e^{-X}/RX$ , which does not correspond to any of our curves.

#### IV. CONCLUSION

A theory is developed for the calculation of the mean ionization distance in solids. The foundation of this formalism is the same as that of the Boltzmann equation, namely, concepts of probability. This shortcut approach clearly relates the physics to the equations and has versatility in applications. A simple application to the isotropic-scattering case produces results that generally agree with that obtained by numerically solving the Boltzmann equation.

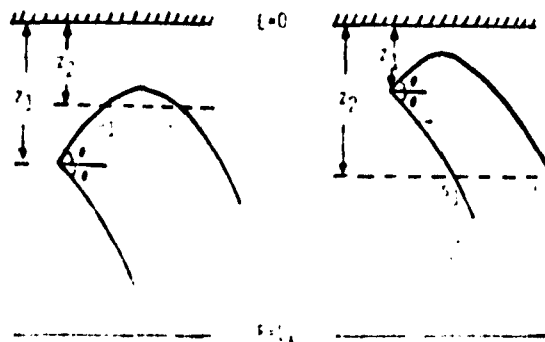


FIG. 8. Geometry of the projectile.

## APPENDIX

This appendix gives the formula for the length of the electron trajectory under the action of a constant external electric force. The ceiling where the kinetic energy of the electron is zero is defined as  $z = 0$ . The coordinate  $z$  is measured

downward (along the direction of the force) and therefore  $eS_z = \frac{1}{2}mv^2$ . The electron at  $z_1$  is projected at angles  $\pm\theta$  ( $\theta$  positive) with respect to the horizon, as shown in Fig. 8. By classical mechanics, the trajectory lengths from the point  $z_1$  to the intersections with a horizontal line at height  $z_2$  are given by

$$S_1(z_2, z_1, \theta) = z_1 \left[ \sin\theta + \cos^2\theta \ln \left( \frac{1 + \sin\theta}{(z_2/z_1)^{1/2} + (z_2/z_1 - \cos^2\theta)^{1/2}} \right) - \left( \frac{z_2}{z_1} \right)^{1/2} \left( \frac{z_2}{z_1} - \cos^2\theta \right)^{1/2} \right], \quad (A1)$$

$$S_2(z_2, z_1, \theta) = z_1 \left[ \sin\theta + \cos^2\theta \ln \left( \frac{1 + \sin\theta}{(z_2/z_1)^{1/2} - (z_2/z_1 - \cos^2\theta)^{1/2}} \right) + \left( \frac{z_2}{z_1} \right)^{1/2} \left( \frac{z_2}{z_1} - \cos^2\theta \right)^{1/2} \right]. \quad (A2)$$

If these lengths and the  $z$  coordinate are scaled by  $\lambda$  and  $y$  is defined as  $z/\lambda$ , the dimensionless

trajectory lengths  $S_1(y_2, y_1, \theta)$  and  $S_2(y_2, y_1, \theta)$  are obtained. They are used in Eq. (18).

<sup>1</sup>K. G. McKay and E. B. McAfee, Phys. Rev. **91**, 1079 (1953); K. G. McKay, Phys. Rev. **94**, 877 (1954).

<sup>2</sup>L. B. Loeb, *Fundamental Processes of Electric Discharge in Gases* (Wiley, New York, 1939).

<sup>3</sup>P. A. Wolff, Phys. Rev. **95**, 1416 (1954).

<sup>4</sup>G. A. Baraff, Phys. Rev. **126**, 2507 (1962); **133**, A26 (1964).

<sup>5</sup>G. H. Wannier, Bell Syst. Tech. J. **32**, 170 (1953).

<sup>6</sup>W. Shockley, Solid State Electron. **2**, 25 (1961).

<sup>7</sup>S. Baidyaroy, M. A. Lampert, B. Zee, and R. U. Martenelli, J. Appl. Phys. **48**, 1272 (1977).

<sup>8</sup>D. L. Lin and B. L. Beers, J. Appl. Phys. (to be published).

ORIGINAL PAGE IS  
OF POOR QUALITY



**ORIGINAL PAGE IS  
OF POOR QUALITY**

A P P E N D I X    2

Reproduced From:

Lin, D.L. and Beers, B.L., Stochastic Treatment of Electron  
Multiplication Without Scattering in Dielectrics, Journal of  
Applied Physics, 52, 5, 3575, 1981.

# Stochastic treatment of electron multiplication without scattering in dielectrics

D. L. Lin and B. L. Beers

Radiation and Electromagnetics Division, Science Applications, Inc. 8330, Old Courthouse Road, Suite 510, Vienna, Virginia 22180

ORIGINAL PAGE IS  
OF POOR QUALITY

(Received 27 July 1980; accepted for publication 14 October 1980)

By treating the emission of optical phonons as a Markov process, a simple analytic method is developed for calculating the electronic ionization rate per unit length for dielectrics. The effects of scattering from acoustic and optical phonons are neglected. The treatment obtains universal functions in recursive form, the theory depending on only two dimensionless energy ratios. A comparison of the present work with other numerical approaches indicates that the effect of scattering becomes important only when the electric potential energy drop in a mean free path for optical-phonon emission is less than about 25% of the ionization potential. A comparison with Monte Carlo results is also given for Teflon.

PACS numbers: 77.50. + p, 52.80. - s

## I. INTRODUCTION

Interest in calculating ionization coefficients  $\alpha$ , in semiconductors and dielectrics dates back about three decades. McKay<sup>1</sup> derived a curve of  $\alpha$ , versus applied electric field from experimental data. Wolff<sup>2</sup> developed a method for computing  $\alpha$ , by expanding the electron distribution function in terms of Legendre polynomials, keeping the first two terms in solving the Boltzmann transport equation in the steady state. This approximation is justified at high electric field strengths. Shockley<sup>3</sup> conjectured that the steady-state electron distribution function must have a spike in the direction of the electric field. By neglecting all other electrons not in this spike, he was able to obtain an expression for  $\alpha$ , such that the logarithm of  $\alpha$ , was inversely proportional to the electric field. This approach is reasonable for low electric fields. Baraff,<sup>4</sup> in an effort to unify the work of Wolff<sup>2</sup> and Shockley,<sup>3</sup> numerically solved the Boltzmann equation. He obtained an important plot of the quantity  $\alpha/\lambda$  versus the quantity  $E_i/e\epsilon\lambda$  for various values of the parameter  $\hbar\omega/E_i$ . In these expressions, the symbol  $\lambda$  is the optical mean free path,  $E_i$  is the energy gap between the valence and conduction bands,  $\hbar\omega$  is the energy of the optical phonon, and  $\epsilon$  is the external electric field. Further work by Baraff<sup>5</sup> concentrated on the high-field case. A spherical harmonics expansion was introduced and a truncation procedure utilized to obtain a closed system of equations. A consideration of temperature effects was later given by Okuto and Crowell,<sup>6</sup> and Crowell and Sze.<sup>7</sup> An alternate approach, involving the concept of Markov processes, was studied by Lin.<sup>8</sup> The results of this approach agree with those of Baraff<sup>4</sup> for the quantity  $\alpha/\lambda$  at small values of  $E_i/e\epsilon\lambda$ , but disagree by a factor of two for larger values of  $E_i/e\epsilon\lambda$ . Monte Carlo studies of hot electron distributions in thin insulating films were reported by Baidyaroy *et al.*<sup>9</sup> From these investigations an interesting scaling law for the average electron energy of the steady-state distribution was numerically obtained.

To date, the calculations of ionization coefficients have

centered around the solution of the Boltzmann equation and concomitant electron distribution function. Though the effects of scattering are properly included in this approach, the numerical methods required to solve the Boltzmann equation may hinder one from gaining a direct insight into the problem. In this paper, the problem will be approached from a different point of view.

Just as the Boltzmann equation is derived by the concept of probability (via cross sections), so it will be assumed that the motion of an electron is a stochastic process. The two approaches are connected by the common concept of the mean free path for the underlying interactions. The cross section multiplied by the number density of scatterers gives the inverse mean free path of transport theory. For a stochastic process, the mean free path is defined in the usual fashion as the mean distance of free trajectories. The probability distribution of free paths is assumed to be of exponential form as described in Sec. II.

To simplify the problem, the effect of scattering is neglected, an assumption which is justified for large electric fields. This simplification, however, does not eliminate the essential aspect of electron multiplication in the phenomena of dielectric breakdown. By comparing the present results with those of Baraff<sup>4,5</sup> (in which scattering is included), one can assess the importance of scattering at various strengths of the external electric field.

## II. THEORY

If  $\lambda$  is the constant mean free path between collisions, the probability of no collision occurring for an electron traveling a distance  $x$  is  $\exp(-x/\lambda)$  and the probability of one collision in  $dx$  is  $dx/\lambda$ . The mean distance  $\bar{x}$  between collisions is given by the expression

$$\bar{x} = \int_0^{\infty} x e^{-x/\lambda} dx / \lambda = \lambda, \quad (1)$$

thus providing a consistent definition of  $\lambda$ .

In the following, we will treat the collisions as stochastic events and calculate the ionization coefficient (for the case that the scattering effect is neglected) by regarding the

<sup>8</sup>Presently at Bell Laboratories, Holmdel, New Jersey 07733.

<sup>9</sup>Presently at Beers Associates, Inc., Reston, Virginia 22090.

effect of the collisions as the events of a Markov process.

Thus an electron is released with zero energy, gains energy from the constant electric field  $\epsilon$ , and loses an amount of energy  $\hbar\omega$  by emitting an optical phonon of energy  $\hbar\omega$  after transversing a constant mean-free-path  $\lambda$ . The question to be addressed analytically is, "What is the mean distance required for the electron to reach the ionization energy  $E_i$ ?"

Shockley's<sup>3</sup> conjecture about the aforementioned spike is based on the Markov concept in a trivial way, as follows. The number of electrons, per unit volume, which have survived the transport to energy  $E_i$  without collisions, is proportional to  $\exp(-E_i/\epsilon\epsilon\lambda)$ , where the quantity  $E_i/\epsilon\epsilon\lambda$  is the distance traveled by the electron to reach energy  $E_i$ . These are the electrons which can "ionize" electrons in the valence band, i.e., promote them to the conduction band. The number of ionizations in a unit length is therefore proportional to  $\exp(-E_i/\epsilon\epsilon\lambda)$ :

$$\alpha_i = c \exp(-E_i/\epsilon\epsilon\lambda). \quad (2)$$

The results of the present analysis, on the other hand, indicate a more complicated dependence on  $(E_i/\epsilon\epsilon\lambda)$ .

To simplify the analysis, choose the ionization energy  $E_i$  such that the relation  $E_i = (n+1)\hbar\omega$  holds, and let the quantity  $\lambda Z_i$  denote the mean distance that an electron will need to travel in order to reach the energy  $E_i$ , given that the electron was released at the origin with an energy  $E = \hbar\omega$ .

There are three basic quantities involved in this problem: (1) the quantum energy of the optical phonon  $\hbar\omega$ , (2) the ionization energy  $E_i$ , and (3) the electric potential energy drop in a mean-free-path  $\epsilon\epsilon\lambda$ . Two independent dimensionless energy ratios can be constructed:

$$R \equiv \hbar\omega/E_i \text{ and } X \equiv E_i/\epsilon\epsilon\lambda.$$

An important distance parameter of relevance to the problem is the distance that an electron must travel in order to gain from the electric field an increment of energy equal to that of an optical phonon. This distance is given by the expression  $\hbar\omega/\epsilon\epsilon$ . Moreover, by choosing the mean-free-path  $\lambda$  as the unit of length, as is done in the following, this distance may be expressed as a dimensionless ratio  $RX$ , also denoted by  $\Delta Z$ . The probability that no collision occurs for an electron traveling a distance  $\Delta Z$  is  $\exp(-RX)$ . The notation  $\alpha \equiv \exp(-RX)$  and  $\beta \equiv RX$  is used in the following development.

Figure 1 illustrates the evolution of the state of an electron beginning with energy  $\hbar\omega$  at the origin as it travels a distance  $\Delta Z$  in the applied field. If no phonon is emitted (an event with probability  $\alpha$ ), it will move to the state  $(l+1)$ . Emitting only one phonon, with probability  $\alpha\beta$ , it will return to the state  $l$ . To end up in the state  $j$  ( $j \neq 1$ ), the electron must emit  $(l-j+1)$  phonons. The probability for this event is  $\alpha P(l,j)$ , where  $P(l,j) \equiv \beta^{l-j+1}/(l-j+1)!$ . The probabilities for multiple emission processes are calculated via simple integrations using the underlying probability assumption stated at the beginning of this section. Finally, the electron has the remaining probability to emit  $l$  phonons and drop down to state 1. The probability for this event is not  $\alpha P(l,1)$  because in the elastic region optical-phonon emission is forbidden. The distance factor  $Z_i$  ( $l < n+1$ ) is connected by a sequence

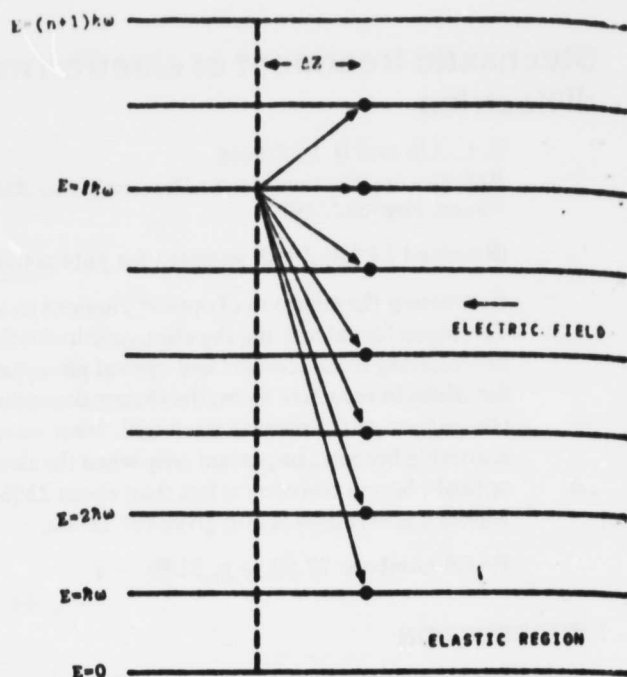


FIG. 1. All possible states of an electron released with energy  $\hbar\omega$  at origin.

of appropriate probabilities to the distance factors  $Z_i + \Delta Z$  where  $k$  takes on the values  $k = (l+1), l, \dots, 1$ . Thus  $Z_0$  is related to  $Z_1$  by the equation  $Z_0 = Z_1 + \Delta Z$ . The general relation is given by the equation

$$Z_l = \alpha(Z_{l+1} + \Delta Z) + \alpha \sum_{j=2}^l P(l,j)(Z_j + \Delta Z) + \left[1 - \alpha - \alpha \sum_{j=2}^l P(l,j)\right](Z_1 + \Delta Z). \quad (3)$$

Because the goal is to calculate  $Z_0$ , it is natural to eliminate the intermediate quantities  $Z_i$  in the above relations by introducing a series of kernels  $K(l)$  which satisfy the equation

$$Z_l = Z_0 - K(l)\Delta Z. \quad (4)$$

It is apparent that the first of these,  $K(1)$  has a value of unity,  $K(1) = 1$ . By substituting the defining relation of Eq. (4) into Eq. (3), a recursive equation for the kernel is obtained. This equation is

$$\alpha K(l+1) = 1 + K(l) - \alpha \sum_{j=2}^l P(l,j)K(j) - \left(1 - \alpha - \alpha \sum_{j=2}^l P(l,j)\right)K(1). \quad (5)$$

This equation, together with the initialization condition  $K(1) = 1$ , determines all of the kernels  $K(l)$ . By inspection, the first few are given by

$$K(2) = \alpha^{-1} + 1; \\ k(3) = \alpha^{-2} + (1 - \beta)\alpha^{-1} + 1.$$

It should be noted that Eq. (5) depends only on the two dimensionless energy ratios  $R$  and  $X$  because  $\alpha$  and  $P(l,j)$  are functions of  $R$  and  $X$ .

Even though the kernels  $K(l)$  are known by solving Eq. (5), the various values of  $Z_i$  ( $i = 1, 2, \dots, n+1$ ) cannot immediately be obtained from Eq. (4) because the quantity  $Z_0$  is still

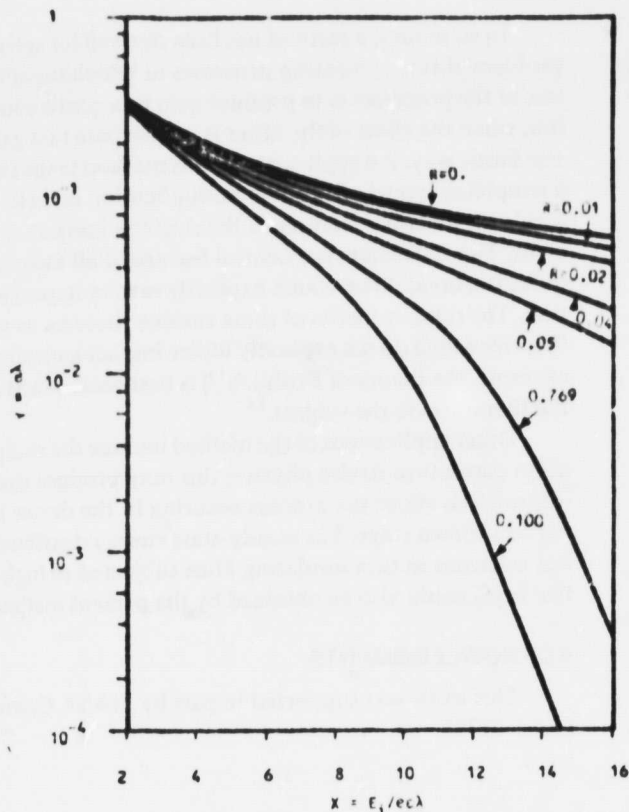


FIG. 2. Ionization coefficient as a function of electric field for various  $R$ .  $Y$  is the number of electron-hole pairs produced in a mean free path;  $X$  is the energy ratio of ionization energy to electric potential-energy drop in a mean free path.

unknown. It is possible, however, to compute the special distance  $Z_{n+1}$  by other means, as is described below. The quantity  $Z_0$  may then be obtained by an application of Eq. (4). For electron energies greater than the ionization threshold  $E_i = (n+1)\hbar\omega$ , the electron of interest can raise a valence-band electron into the conduction band (collision ionization). This occurs in travelling a mean free ionization path  $\lambda_i$  which is assumed to be much smaller than  $\lambda$ . With this assumption, the relation  $Z_{n+1} = \lambda_i/\lambda$  is immediately obtained. Setting  $l = n+1$  in Eq. (4) then determines  $Z_0$  as a function of  $R$  and  $X$ .

With the mean-free-path  $\lambda$  chosen as the unit of length, the ionization coefficient (denoted by  $Y$ ) is given by  $Y = 1/Z_0$ . Thus, the number of ionization events  $Y$  in a mean-free-path  $\lambda$  is a function of the two energy ratios

$$R = \hbar\omega/E_i$$

and

$$X = E_i/e\epsilon\lambda.$$

### III. DISCUSSIONS AND CONCLUSION

Calculations have been carried out for various values of the parameter  $R = \hbar\omega/E_i$ . These results are shown in Fig. 2 for the condition that  $\lambda_i = \lambda$ . The curve for  $R = 0$  ( $n = \infty$ ) is obtained by special considerations. In this limit (zero optical-phonon energy), the electron does not lose any energy via the emission process so that the relation  $Z_0\lambda = E_i/e\epsilon + \lambda_i$

holds. This relation implies that  $Y$  is given by the expression

$$Y = 1/(1 + X) \text{ for } \lambda_i = \lambda. \quad (6)$$

The curves of Fig. 2 as generated by the present analysis do not have the simple behavior implied by Eq. (2) (a straight line on a semilog plot), except for the case when  $R = 0.5$ . This complicated behavior is expected because there are terms of the type  $\exp(mRX)$  ( $m = 1, 2, \dots, n+1$ ) in the equation determining  $K(n+1)$ . It is only for the condition that  $m = n+1$  that  $\exp(mRX) = \exp(Y)$ , the behavior of Eq. (2).

Comparison with Baraff's<sup>4</sup> and Lin's<sup>5</sup> results, in which an isotropic scattering effect is included, shows that the present results agree with theirs only for small values of  $X$  ( $X \leq 4$ ). In this regime, the electric field is so high that the direction of the electron after an isotropic scattering reverts almost immediately to the direction of the applied field. On the other hand, for large  $X$  (small electric field), the scattering effect should be very important. Indeed, the present results deviate significantly from theirs under these conditions. The difference is shown in Fig. 3 for a value of  $R = 0.02$ .

The curves in Fig. 2 are the same in general form as those from more realistic calculations<sup>4,5</sup>; thus increasing the ratio of the optical-phonon energy ( $\hbar\omega$ ) to the ionization threshold energy ( $E_i$ ) rapidly decreases the number of ionizations per mean free path. Though the isotropic scattering effect must be included in describing the actual physical situ-

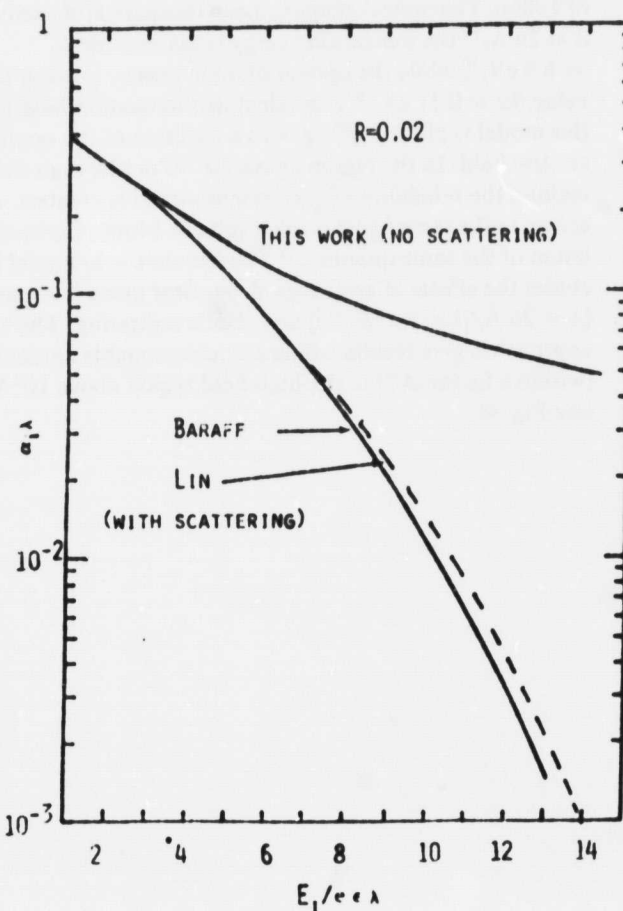


FIG. 3. Ionization events per mean free path as a function of electric field  $\epsilon$ .



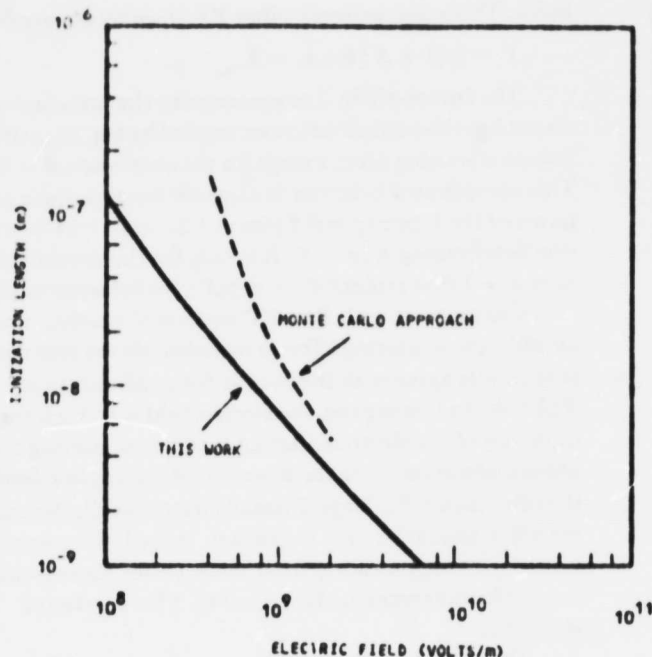


FIG. 4. Ionization length as a function of external electric field<sup>1</sup> for  $\text{CF}_2$ .

ation, the essential features of electron multiplication in dielectrics is contained in, and described by, the present simple approach.

The above approach has been applied to a crude model of Teflon. The optical-phonon mean free path is chosen to be  $\lambda = 26 \text{ \AA}$ ,<sup>10</sup> the ionization energy is taken to be  $E_i = 6.5 \text{ eV}$ ,<sup>10</sup> while the optical-phonon energy is given the value  $\hbar\omega = 0.11 \text{ eV}$ .<sup>10</sup> The calculated ionization length for this model is plotted in Fig. 4 as a function of the applied electric field. In the region above  $10^9 \text{ V/m}$  (the high-field region), the reliability of the present model is greatest. Also shown in the same figure is the result of a Monte Carlo calculation of the same quantity.<sup>11</sup> The Monte Carlo model includes the effects of an energy-dependent mean free path<sup>12</sup> [ $\lambda = 26 \text{ \AA} / (1 - \hbar\omega/E)^{1/2}$ ] and elastic scattering. The two approaches give results which are in reasonable agreement (within a factor of 2) in the high-field region above  $10^9 \text{ V/m}$  (see Fig. 4).

In summary, a method has been derived for solving the problem of two competing processes in which the effect of one of the processes is to produce gain in a continuous fashion, while the effect of the other is to dissipate that gain in a stochastic way. An application of this method to the study of a simplified model of electron multiplication in dielectrics yields the essential features of the electron ionization coefficient. This coefficient is a central feature of all theories of dielectric breakdown which explicitly invoke impact ionization. The relative merits of these various theories, as well as theories which do not explicitly utilize impact ionization (for example, the theory of Fröhlich<sup>13</sup>) is best ascertained from the literature on the subject.<sup>14</sup>

Other applications of the method include the analysis of noise currents in device physics; this may produce useful information about the process occurring in the device in the prebreakdown stage. The steady-state energy distribution of hot electrons in thin insulating films subjected to high-electric fields could also be obtained by the present method.

#### ACKNOWLEDGMENTS

This work was supported in part by NASA Contract No. 3-21378.

<sup>1</sup>K. G. McKay, Phys. Rev. **94**, 877 (1954).

<sup>2</sup>P. A. Wolff, Phys. Rev. **95**, 1415 (1954).

<sup>3</sup>W. Shockley, Solid-State Electron. **2**, 35 (1961).

<sup>4</sup>G. A. Baraff, Phys. Rev. **128**, 2507 (1962).

<sup>5</sup>G. A. Baraff, Phys. Rev. **133**, A26 (1964).

<sup>6</sup>Y. Okuto and C. R. Crowell, Phys. Rev. **B 8**, 3076 (1972).

<sup>7</sup>C. R. Crowell and S. M. Sze, Appl. Phys. Lett. **9**, 242 (1966).

<sup>8</sup>D. L. Lin, Phys. Rev. **B 20**, 5238 (1979).

<sup>9</sup>S. Baidyaroy, M. A. Lampert, B. Zee, and R. U. Martinelli, J. Appl. Phys. **47**, 2103 (1976); **48**, 1272 (1977).

<sup>10</sup>B. L. Beers, V. W. Pine, H. C. Hwang, H. W. Bloomberg, D. L. Lin, M. J. Schmidt, and D. J. Strickland, First Principles Numerical Model of Avalanche-Induced Arc Discharges in Electron-Irradiated Spacecraft Dielectrics, SAI Report Number SAI-102-79-002 (unpublished).

<sup>11</sup>V. W. Pine (private communication).

<sup>12</sup>F. Seitz, Phys. Rev. **73**, 549 (1948).

<sup>13</sup>H. Fröhlich, Proc. R. Soc. London, Ser. A **188**, 521 (1947).

<sup>14</sup>See, for example, J. J. O'Dwyer, *The Theory of Electrical Conduction and Breakdown in Solid Dielectrics* (Clarendon, Oxford, 1973).

ORIGINAL PAGE IS  
OF POOR QUALITY

### A P P E N D I X 3

#### Reproduced From:

Beers, B.L., Pine, V.W. and Ives, S.T., Theoretical Properties of Streamers in Solid Dielectrics, 1981 Annual Report, 390, Conference on Electrical Insulation and Dielectric Phenomena, IEEE Electrical Insulation Society, 1981.

**ORIGINAL PAGE IS  
OF POOR QUALITY**

**THEORETICAL PROPERTIES OF STREAMERS  
IN SOLID DIELECTRICS\***

B.L. Beers, V.W. Fine, and S.T. Ives

Beers Associates, Inc.  
Post Office Box 2549  
Reston, Virginia, 22090

**INTRODUCTION**

A model has previously been described (1,2) which provides for the self-consistent numerical description of the spatially and temporally coherent evolution of electron avalanches in solid dielectrics. Various features of the propagating negative tip of the avalanche have been presented (1), and speculations were offered about the possible importance of recurring processes at the positive tip leading to cathode directed streamer formation and subsequent breakdown (2). An extensive set of numerical calculations has now been performed within this model framework. The purpose of the calculations was to explore the dependence of important calculational features on the input parameters of the model. A preliminary description of the results of this parameter study is given in this note. The research is part of an ongoing program to understand the charging and discharging properties of electron beam irradiated solid dielectrics.

**MATERIAL PARAMETERS AND TRANSPORT COEFFICIENTS**

The transport coefficients to be used as parameters for the macroscopic description of the avalanche must first be obtained. In the reported approach (1), these parameters are obtained by solving the Boltzmann transport equation for the single electron distribution function. The solution is obtained by a single-scattering Monte Carlo approach as implemented in the computer code

\* Work supported by the National Aeronautics and Space Administration, Lewis Research Center under Contract Number NAS3-22530.

SEMO (1). The required input data are a model of the electron scattering processes (a material model) and the applied electric field strength.

For the purpose of this parameter study, a very simple material model was chosen. Three scattering processes were considered; scattering from acoustic phonons; emission of optical phonons; and excitation of interband transitions (collision ionization). The mean free path  $\lambda_{el}$  for acoustic phonon scattering was taken to be constant. The optical phonon spectrum was represented with a single optical phonon of energy  $\hbar\omega_0$ . The energy dependence of the mean free path for optical phonon emission is that given by Seitz (3), while the scale is set with a variable parameter  $\lambda_0$ . Interband transitions are described with a threshold  $E_I$  for electron-hole creation together with a constant mean free path  $\lambda_I$  above the threshold. Scattering from acoustic phonons was taken to be isotropic, while both inelastic processes were assumed to occur without angular deflection.

A material model is therefore described with the following set of parameters:

$$\{q, m^*, \epsilon_r, \lambda_{el}, \lambda_0, \lambda_I, \hbar\omega_0, E_I\},$$

where  $q$  is the electronic charge,  $m^*$  the effective mass of the electron, and  $\epsilon_r$  the relative dielectric constant of the material. The remaining problem parameter is the impressed electric field  $E$ . The set of quantities  $\{m^*, \lambda_{el}, E_I\}$  was chosen as the fundamental dimensional set, and the Boltzman equation was brought to non-dimensional form. The resulting equation is totally independent of  $\epsilon_r$ . The following five dimensionless parameters characterize the resulting equation:  $\Lambda_0 = \lambda_0/\lambda_{el}$ ;  $R = \hbar\omega_0/E_I$ ;  $X = E_I/(qE\lambda_{el})$ ;  $\Lambda_I = \lambda_I/\lambda_{el}$ ;  $\Omega = q/(q\lambda_{el}^2)^{1/2}$ . In fact, the linear problem is independent of  $\Omega$ . For this parameter study, the dependence on the variable  $\Lambda_I$  was suppressed. A value of  $\lambda_I$  was chosen sufficiently small that ionization occurs practically instantaneously once the threshold is reached. This is a good physical assumption, and is in accord with other researchers (4,5,6). The parameter  $X$  is taken to be a measure of the electric field. Up to scaling by the fundamental dimensional set, a material model is therefore specified by a pair of values  $\{\Lambda_0, R\}$ .

Computations of the transport coefficients were



performed with values of  $\lambda_0$  in the range from [1, 25] and values of  $R$  in the range from  $[4 \times 10^{-3}, 2 \times 10^{-1}]$ . Both the diffusion coefficient and the mobility were found to be rather insensitive to the values  $R$  and  $\lambda_0$  in the high field limit ( $X$  in the range of [2, 30]) which is the parameter regime of concern for this note. Both  $D$  and  $\mu$  vary as a function of the field strength. In dimensionless units,  $D$  increases from 0.1 to 0.2 as  $X$  is decreased from 30 to 2, corresponding to electron heating for the higher field values. Similarly,  $\mu$  decreases from 2.2 to 0.6 over the same parameter range, exhibiting the anticipated trend toward saturation of the drift velocity at high fields. The mean energy (effective temperature) shows a slightly greater variation with the parameters  $\lambda_0, R$ , indicating that the coefficient in the Einstein relation depends more strongly on these parameters than  $\mu$  or  $D$  individually. The mean energy varies by about a factor of five from the lowest fields to the highest, with dimensionless values in the range  $[3 \times 10^{-2}, 1.8 \times 10^{-1}]$  depending on the values of  $\lambda_0, R$ .

The quantity most sensitive to the parameter values (and the field) is the ionization length, or its inverse  $\alpha$  (the first Townsend coefficient). Shown in figure 1 are plots of  $\alpha$  (in units of  $\lambda_{el}^{-1}$ ) as a function of  $X$  for 10 different scattering sets. Given the rough independence of  $\mu$  and  $D$  on the parameters  $\lambda_0$  and  $R$ , the quantity  $\alpha$  is the quantity which characterizes a material model for the macroscopic description discussed below. The general features of the curves in figure 1 may be understood from previous semi-analytical work (4, 5,6).

#### STREAMER EVOLUTION

The macroscopic model of the self-consistent evolution of electron avalanche requires specification of the parameters  $\mu$ ,  $D$  and  $\alpha$  (1,2). A universal value of  $D$  was chosen, given its weak dependence on both material model and field. A universal fit of the mobility as a function of field strength was chosen because of its weak dependence on material model. Finally, the ionization coefficient  $\alpha$  was fit with the usual form

$$\alpha = \alpha_0 \exp(-E_0/E)$$

where  $\alpha_0$  and  $E_0$  are the fitting parameters which depend

on  $A_0$  and  $R$ . This functional form provides a rather good representation of the data of figure 1.

The initial conditions for integrating the continuity equations were determined as follows. A primary electron avalanche was developed in a Monte Carlo fashion using the distribution of ionizations obtained from SEMC. (1). The evolution was stopped when the self-field of the avalanche obtained a value of 50% of the applied field. The resulting charge distribution was used as the starting point for the macroscopic description. Inspection of these distributions has shown them to be entirely consistent with simple analytical representations of the primary undistorted avalanche (7).

The macroscopic equations describing the evolution of the avalanche may be brought to dimensionless form(1). Solutions depend on two dimensionless parameters which have been chosen to be  $\zeta_1 = (D_0/\mu E)$  and  $\zeta_2 = (q_0 e^2/\epsilon E)$ . The first parameter may be reexpressed as the ratio of the mean electron energy to the energy extracted from the field in an ionization length. The second is the ratio of two electric fields; that due a single electron located one ionization length distant, and the ambient field. Larger values of  $\zeta_1$  correspond to diffusion being relatively more important than drift, while smaller values correspond to the opposite condition. The quantity  $\zeta_2$  is a measure of the strength of the external field in terms of the fundamental Coulomb separation field. For the model parameters associated with figure 1,  $\zeta_1$  varies in the range of  $[4 \times 10^{-4}, 3 \times 10^{-1}]$  while  $\zeta_2$  varies in the range  $[5 \times 10^{-6}, 7 \times 10^{-1}]$ .

Both parameters show wide variation for the model values chosen for this study. For the models and field levels associated with figure 1, a scatter plot of the actual values of  $\zeta_1$  and  $\zeta_2$  was generated. On a log-log plot, the values displayed a remarkable trend. Essentially all the values lie within a narrow band of a straight line on the plot. The straight line has a slope of roughly 1.5, corresponding to a constant value of the quantity  $\zeta_3 = (\zeta_2/\zeta_1^{3/2})$ . Computation of  $\zeta_3$  for the various model values shows that it varies by less than one order of magnitude (corresponding to the band width) over this wide range of model values. It is possible to examine the solutions of the equations as a function of a single parameter (say  $\zeta_1$ ) with the remaining parameter determined by the constancy of  $\zeta_3$ .

ORIGINAL PAGE IS  
OF POOR QUALITY

394

( $\tau_2 = \tau_1^{3/2}$ ). This greatly reduces the number of computations required to explore the parameter space. This scaling law is not understood at present. It should be noted, however, that  $\tau_2$  is the dimensionless parameter which occurs when estimating the strength of the self-field in the undistorted avalanche alluded to above (7). The significance of this coincidence of parameters is also not understood.

Though strongly indicative, the above scaling discussion is oversimplified as it only concerns itself with the overall dimensional aspects of the problem. In fact, the transport coefficients  $\mu$  and  $\alpha$  have a rather strong dependence on the field, and vary significantly in space and time during the evolution of the streamer. The parameters determining this variation add further dimensionless variables to the problem. The possibility that the dependence associated with this coefficient variation in a single problem might have a major impact on the form of the solutions lead to an initial choice of computations based primarily on distinctive functional forms for the transport coefficients. Referring to figure 1, it was decided to compute the evolution for the ionization curves associated with model numbers 2, 9 and 10, computations being performed over the span of field values in the figure. Unfortunately, this choice lead to a series of computations in which the dimensionless parameter  $\tau_2$  only varied by two orders of magnitude,  $\tau_1 \in [2 \times 10^{-2}, 4 \times 10^{-1}]$ ,  $\tau_2 \in [10^{-2}, 8 \times 10^{-1}]$  rather than over the full range implied by the previous discussion. Exploration of some of the smaller values of  $\tau_2$  awaits future work.

It follows from the defining equations that the total number of electrons in the streamer grows exponentially as  $\langle n \rangle \propto \langle n \rangle_0 e^{\langle \alpha \rangle t}$ , where  $\langle \cdot \rangle$  indicates an electron density weighted average of the ionization rate. The quantity  $\langle \alpha \rangle$  provides the simplest diagnostic on the distribution of electrons and fields during the avalanche. Shown in figure 2 are the results of eleven separate computations of the growth of the number of electrons as a function of  $\beta t$ . The solid line is a best fit to the set of all points in this composite figure. Individual data points are indicated to show the spread. The figure suggests very strongly that seemingly different computations are in fact very much the same when viewed in appropriate dimensionless variables.

ORIGINAL PAGE IS  
OF POOR QUALITY

195

Another parameter which provides a diagnostic of the evolution is the peak charge density (or the maximum field enhancement). In dimensionless units, the anticipated peak charge density is given by  $\epsilon_0^{-1}$ . Indeed, for each of the separate computations noted above, this value is attained as a saturation value. Finally, the position of the centroid of negative charge as a function of time may be followed in dimensionless units. These points also lie roughly on the same curve, with the same degree of scatter as in figure 2. The resulting drift velocity is being accelerated at a rate of  $1.4 \times 10^{-2}$  (in dimensionless units  $v_D(t)$ ).

The above diagnostics, together with detailed examination of the evolution of the various computations very strongly suggest that the evolution of negative-tip streamers tends to a similarity solution over a large range of problem parameter values. This type of behavior may be expected from systems exhibiting negative feedback.

- (1) B.L. Beers, V.W. Pine, H.C. Hwang, and H.W. Bloomberg, I.E.E.E. TRANS. NUC. SCI. NS-26, 5127 (December, 1979).
- (2) B.L. Beers, H.C. Hwang, and H.W. Bloomberg, 1979 Annual Report, CEIDP (1979), p. 212.
- (3) F. Seitz, Phys. Rev. 73, 549 (1948).
- (4) G.A. Baraff, Phys. Rev. 128, 2507 (1962), Phys. Rev. 133, A26 (1964).
- (5) D.L. Lin, Phys. Rev. B20, 5238 (1979).
- (6) D.L. Lin and B.L. Beers, J. Appl. Phys., (to be published).
- (7) H. Raether, Electron Avalanches and Breakdown in Gases, Butterworth, Washington, (1964).

ORIGINAL PAGE IS  
OF POOR QUALITY

396

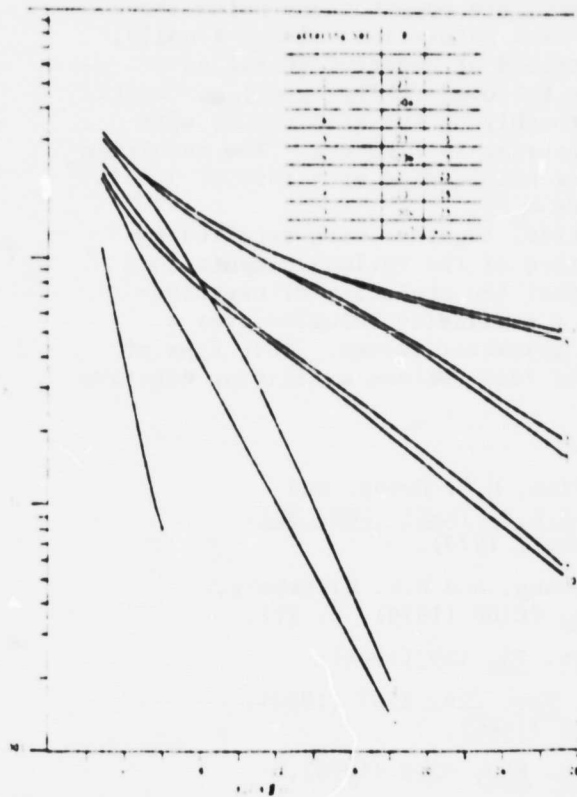


Figure 1

Plot of the inverse ionization length  $\lambda$  (in units of  $\lambda_{el}^{-1}$ ) versus the dimensionless field variables  $E_I(q\lambda_{el})$  for ten different material models (see text for discussion of material model).

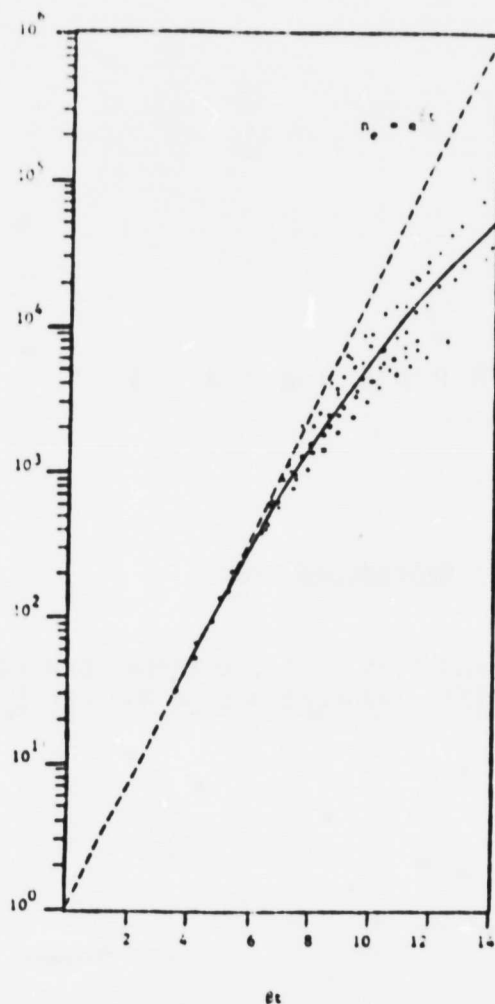


Figure 2

Plot of the number of electrons in the streamer simulation as a function of the dimensionless time  $Rt$ . The plot is a composite of eleven distinct computations for different problem parameters.

ORIGINAL PAGE IS  
OF POOR QUALITY

#### A P P E N D I X 4

Reproduced From:

Beers, B.L., Pine, V.W. and Ives, S.T., Internal Breakdown of Charged  
Spacecraft Dielectrics, IEEE Transactions on Nuclear Science, NS-28,  
6, 4529, 1981.



# INTERNAL BREAKDOWN OF CHARGED SPACECRAFT DIELECTRICS\*

B.L. Beers, V.W. Pine, and S.T. Ives

BEERS ASSOCIATES, INC.  
Post Office Box 2549  
Reston, Virginia 22090

ORIGINAL PAGE IS  
OF POOR QUALITY

## ABSTRACT

The primary purpose of this paper is to suggest that low differential voltage, small energy discharges associated with internal buried charge may be a dominant mechanism by which stored electrostatic energy is released from dielectrics on board orbiting spacecraft. The evidence from space as given by Stevens<sup>1</sup> is noted. Laboratory experimental evidence of Frederickson<sup>2</sup> is invoked to demonstrate that discharges occur under circumstances with no external potential drop. Previous calculations<sup>3,4</sup> are then reviewed which indicate that significant internal electric fields can exist in dielectrics charged with multiple-kilovolt electron beams under conditions involving little or no external potential drop. The internal discharge mechanism of Meulenberg<sup>5</sup> is recalled, and new calculations suggesting that the space environment is conducive to the formation of the conditions required by this mechanism are presented. Experimental procedures for checking the suggestions of the paper are developed.

## BACKGROUND

Early in the history of concern with the spacecraft charging problem, Meulenberg<sup>5</sup> proposed a mechanism for break-down in electron irradiated dielectrics which is critically dependent of the character of the electric fields very near to the surface of the material. For a variety of reasons, subsequent experimental work did not concentrate on the conditions required for this mechanism. Most work was directed to configurations resulting in large surface to substrate differential potentials. For these charging conditions, very severe and distinctive discharges were observed.<sup>6,7,8,9,10</sup> The conditions of the reported experiments (referred to as "Standard" herein) are those associated with a monoenergetic electron beam incident on a sample with a grounded substrate. For sufficiently large beam energy and/or current, discharges were universally observed. The area scaling relationships that were expected and observed<sup>7</sup> suggested extremely large amplitude, long pulse width discharges for the large areas typical of spacecraft. Reports<sup>10</sup> of the observation of these monster discharges under "standard" conditions lead to the realization that if this type of experiment were indicative of space conditions, then the spacecraft charging problem was extremely severe. Direct measurements<sup>10,11</sup> of the electric and magnetic fields associated with these large discharges directly supported the idea developed earlier that these large current discharges were associated with a space-charge "blow-off" current.

Within the past year, the idea that the

discharges associated with these "standard" simulations may be significantly different from those which occur in space began to evolve.

Recent experimental work by Frederickson<sup>2</sup> has shown that most types of common spacecraft dielectrics undergo spontaneous internal breakdown when irradiated by high-energy electrons ( $\sim 1$  MeV). By internal breakdown, we mean that the experimental configuration is such that there are no external potential drops across the dielectric sample -- breakdown must be caused by field internal to the dielectric. While these results are no particular surprise to workers in the area, and earlier work<sup>12</sup> has shown similar effects in more complicated configurations, Frederickson's results do establish the presence of the effect beyond doubt. The results also establish the fact that any program designed to ascertain breakdown criteria for spacecraft dielectrics must consider far more detail than has heretofore been assumed. In particular, the measurement of external potential differences under a variety of charging conditions is clearly sufficient to characterize the onset of breakdown.

In his paper, Frederickson<sup>2</sup> explicitly notes that the generic features which characterize the accumulation of charge for MeV electron irradiations are no different than those which characterize multiple keV electron irradiations. The implication of this statement is clear. Irradiations with multiple-keV electron spectra characteristics of the spacecraft charging environment can be expected to lead to breakdown even when external potential differences are small. Supporting evidence for this viewpoint is also becoming available from space. Stevens<sup>1</sup> has pointed out that SCATHA data indicate that breakdowns are occurring on-orbit, despite the fact that only small differential voltages are being observed. The appearance of small, relatively benign discharges, under the conditions of small differential potentials suggests that the "standard" simulations are giving rise to qualitatively dissimilar discharges caused by a different mechanism. The internal breakdown observed by Frederickson<sup>2</sup> and proposed by Meulenberg<sup>5</sup> is certainly a candidate mechanism. The conditions required for this mechanism in a space-like environment are explored below.

## CONCEPTUAL MODEL

Previous papers<sup>3,4</sup> on the subject of internal charge distributions in dielectrics subject to spacecraft charging type environments have provided the computational frame work for understanding the dielectric conditions of importance for internal breakdown. Indeed, it was explicitly noted in these publications that low-differential voltage internal breakdowns were a real possibility.

The non-charging beam introduced in Reference 3 is a convenient device for understanding the essential features of internal field buildup. A

\* Work sponsored by the National Aeronautics and Space Administration, Lewis Research Center under Contract Number NAS3-22530.



non-charging beam for a particular material is a beam for which the surface emits precisely one electron for each electron incident on the material. Assuming that the emitted electrons are primarily secondaries (emitted from a region very near the surface ( $\sim 50 \text{ \AA}$ )), and that the primary electrons penetrate substantially deeper than the secondary emission region, it is apparent that the primary deposition leads to a charge separation in the material. This region of separated charge contains an internal electric field (even though there is no external potential). For conceptual purposes, assume all secondary charge is emitted from the precise geometric surface, and that all primary charge is deposited at a single depth  $d$ . Let  $\sigma$  be the conductivity in the region from the surface to a depth  $d$  (assumed for simplicity to be uniform). The internal electric field is given by the well-known expression:

$$E = - (1 - \exp(-\frac{\sigma}{\epsilon} t)) \frac{J}{\sigma},$$

where  $J$  is the beam current density, and  $\epsilon$  the permittivity of the medium.

Essentially all qualitative features of the internal charge and field buildup may be ascertained from this expression. The magnitude of the internal field is limited only by the conductivity of the irradiated region. Writing the conductivity as  $\sigma_0 + \sigma_p$ , where  $\sigma_0$  is the ambient conductivity in the unirradiated material, and  $\sigma_p$  is radiation-induced conductivity (RIC), the various regions may be explored depending on whether  $\sigma_0$  or  $\sigma_p$  is dominant. We will only consider the circumstances in which  $\sigma_p$  is dominant, because most materials of practical interest exhibit this dominance at levels of current characteristic of exoatmospheric environment.

If  $\sigma_p$  is linear in dose rate, the internal field will saturate at a maximum material dependent value, which may or may not be above the breakdown strength for the given material. If  $\sigma_p$  is sub-linear in dose (as it almost surely is for high enough dose rates and/or doses), then the field may be driven arbitrarily high by increasing the driving current. Breakdown is guaranteed for sufficiently high current level.

Examination of the range-energy relationship for electrons shows that the mean energy loss over the range of the electron decreases with increasing primary electron energy. It follows that the mean volumetric dose throughout the deposition region decreases for increasing electron energy. Thus, for a given material, and given current level, an increase in the energy of the primary electrons will lead to an increase in the internal field.

Both the above statements are easily quantified within a computational model of the type previously given.<sup>2,3</sup> We prefer to explore the possibilities for achieving the above conditions. A single monoenergetic beam can be non-charging as noted in Reference 3. For a given material, only a single incident energy can satisfy the conditions, so the possibility for varying the second parameter (depth) is not available in this configuration. The simplest way to achieve non-charging with a given monoenergetic electron beam is to provide a second source of irradiation which produces a copious supply of secondaries. Possibilities for the second source are: low energy electron beam, ion beam, photons. The third choice is less desirable for materials which are photoconductive for the wavelengths of interest, as it introduces yet another variable into the problem. Once the basic effect is quantified, of course, it will be important to include sunlight for full environmental simulation.

Having chosen a surface neutralizer, the basic experimental program involves varying the energy and current density of the penetrating beam until breakdown occurs. The location of the breakdown threshold as a function of deposited charge and beam energy should provide an excellent empirical criterion for internal breakdown. Combining such experiments with computations for the configuration will permit the identification of internal conditions at breakdown, as has already been shown.<sup>1</sup> It might be speculated that breakdown will occur when internal fields reach levels of a few times  $10^7 \text{ V/m}$  - the breakdown levels found by Fredrickson.<sup>1</sup>

The point of this section is very simple. There exist free floating front surface charging configurations such that no potential drop is developed between the surface and substrate for which significant internal fields are developed. These large fields are near the front surface. If large enough, they can lead to breakdown in this region.

## RESULTS

A number of calculations have been performed to compare the internal charge and field conditions in a typical dielectric due to a monoenergetic electron beam to those due to a space-like electron distribution. The space-like electron environment which was chosen for simulation was an isotropic Maxwellian with a temperature of 11.5 keV. This environment was taken to represent the hot electron portion of a double Maxwellian fit to the electron distribution function during a severe substorm.<sup>13</sup> The electron transport model for determining conditions interior to the dielectric has previously been described.<sup>3</sup> The model is one-dimensional. To specify the charging, the incident electron distribution function is required as a function of the surface voltage. For true space-like conditions, this specification requires the solution of the coupled Poisson-Vlasov problem for the dielectric/space craft configuration of interest. This type of solution can be obtained using the NASCAP<sup>14</sup> computer code.

For the purposes of this study a much simpler approach was chosen. Two distinct realizable configurations admitting analytic solutions were chosen. The variation from one solution to the other is believed adequate to be indicative of the type of change which might be expected were the details of the actual distribution function to be used. The first configuration is that of a semi-infinite surface, a one dimensional problem in which the pertinent dimension is the distance from the surface. The equations describing this simple situation are well-known. For an isotropic Maxwellian at infinity, the incident distribution is due to an unperturbed Maxwellian in the directions parallel to the surface, and a shifted cutoff Maxwellian in the direction perpendicular to the surface. This represents a shift in both energy and angle as a function of surface voltage. For larger surface voltages, the incident flux is more nearly mono-directional. The second configuration is that which is familiar from spherical probe theory. That is, the surface is uniform and spherical and the object size is small compared to the plasma Debye length. The incident flux in this case is that due to a shifted and cutoff Maxwellian in the total energy. The flux remains isotropic as a function of the surface voltage.

The sample chosen for computation was a 2 mil thick Kapton. The computations were performed with the following normal materials parameters: relative dielectric constant, 3.45; density  $1.23 \text{ g/cm}^3$ ; prompt conductivity coefficient,  $K_p = 1.16 \times 10^{-17} \text{ mho/m/rad/sec}$ ; dark field dependent conductivity given by the

data of Adamo, et.al.;<sup>15</sup> secondary yield proportional to surface dose according to the model of Burke, Wall and Frederickson,<sup>16</sup> using the data compilation of Burke.<sup>17</sup> Three computations were performed; one using a 20 keV mono-energetic normally incident beam (labelled MONO); one using the surface flux taken from the one-dimensional model noted above (labelled MAX); and one using the surface flux taken from spherical probe theory noted above (labelled SPT). For the latter two cases, the distribution at infinity is the 11.5 keV isotropic Maxwellian noted above. All three computations were performed with a unperturbed current density of 0.8 nA/cm<sup>2</sup>, representing a severe charging environment.

As anticipated, the substantially higher secondary yield associated with the distribution of electrons (particularly the angular distribution) leads to substantially lower surface voltages for the space-like environment than for the mono-energetic charging situation. It should be noted that at saturation, the rather high field dependent conductivity of Kapton makes the bulk leakage current the dominant contribution to the equilibrium current. Because of this fact, the equilibrium voltage for a monoenergetic source is a very weak function of the beam energy at the given current density. Similar charging curves may be expected for smaller beam energies, and the choice of 20 keV may be viewed as representative. The relatively small difference between the two cases with space-like environments may be attributed to the differences in secondary yield for the two. The secondary yield obtained from the SPT flux is higher, leading to a lower surface voltage. Overall, the figure displays the well-known fact that space-like distributions give rise to substantially lower charging voltages than those obtained from mono-energetic charging simulations. Inclusion of an ionic current makes this difference even larger.

Shown in Figure 2 is the location of the mean penetration of the charge in the dielectric (the charge centroid) as a function of time. The monoenergetic results are similar to those previously presented.<sup>4</sup> The results for the space-like environment show a very weak dependence on both model and time. The major feature of the figure is the substantially deeper penetration associated with the space-like environment, showing the importance of the higher energy electrons. Shown in Figure 3 are the fields internal to the dielectric for the three charging conditions at a time near saturation of the external potential. The bulk fields (to the right) show the variation (from model to model) expected due to the variation in surface voltage shown in Figure 1. The higher the surface voltage, the higher the bulk fields (distances in the dielectric beyond the penetration of the electrons). What might not have been anticipated is that the space-like environment leads to higher fields near the front surface of the dielectric, with the dependence on surface voltage reversed. The higher the surface voltage, the lower the front surface fields. The differences in this region are quite strong, being almost a factor of three between the monoenergetic and spherical probe theory simulations.

Consideration of the charging in the framework of the Meulenber<sup>5</sup> bilayer suggests that the behavior of Figure 3 is precisely what one would expect. Layer secondary yields are in the same order as the order of the front face fields. With similar amounts of buried charge, the field in this region must vary with the surface positive charge. Shown in Figure 4 is a comparison of the internal charge density at the same time as Figure 3. The internal charge distribution

for the two space-like simulations is virtually identical and not distinguished on the figure. On the distance scale of the figure, the surface positive charge would appear as a delta function and is not included in the display. The space-like environment shows the substantially deeper penetration suggested by Figure 2, and gives rise to the greater depth over which the electric field varies as shown in Figure 3. Over most of the range of depths, the deposited charge densities are very similar, being a few thousand coulombs/m<sup>3</sup> (few times 10<sup>16</sup> electrons/cm<sup>3</sup>). The space-like environment does not give rise to the strong charge enhancement very near the front face seen for the monoenergetic simulation (which is in part artificial, and reduced, by the front positive charge density). The total negative charge deposited in both cases is very similar.

Several further calculations were performed to examine the dependence of the space-like simulation results on the problem parameters. The transient conductivity coefficient  $K_p$  was allowed to be 10 times bigger and 10 times smaller than the nominal value, representing the range of typical values of  $K_p$ . The dark field dependent conductivity was allowed to be 10 times larger, representing a typical "fix" to the charging problem. The secondary yield was allowed to be a factor of 2.7 times larger than nominal, representing both a possible "fix", and also a large contribution to secondary yield due to ionic environment. (For much larger values of  $\delta$ , the material will charge positively). All calculations were performed using the spherical probe theory incident environment discussed for the previous results. Only one parameter is varied from nominal for each calculation.

Shown in Figure 5 is the surface charging voltage versus time for the nominal case (NOM) and the four variations noted above. Variation in  $K_p$  give rise to only minor variations in the final charging voltage as shown. Rearrangement of the charge in the deposition region has little effect on this variable. Of course, an increase in  $\sigma_0$ , or  $\delta$  gives rise to a substantial reduction in surface voltage. That an increase of  $\sigma_0$  by a factor of 10 only gives rise to a voltage reduction of a factor of two reflects the sharp field dependence of the dark conductivity in Kapton. The much slower charging for the case of a larger secondary yield is precisely as expected. However, even in this case, it is the sharp field dependence of the conductivity which turns off the charging.

In Figure 6 are shown the internal electric fields at saturation for the same parameter variation. The variations in  $K_p$  give rise to variations in the field only in the deposition region. While it might seem surprising that the bulk fields are identical when there are variations in surface voltage as shown in Figure 5, a little reflection should convince the reader that Figures 5 and 6 are both correct. Rearrangement of the charge in the deposition does effect the surface voltage but does not affect the bulk field. Within the deposition region the variations with  $K_p$  are those expected from previous work.<sup>3</sup> Smaller  $K_p$  values of  $K_p$  give rise to larger values of the front face field.

Increasing the bulk dark conductivity is effective in decreasing both the bulk fields and fields in the deposition region. This is expected. By contrast, increasing the secondary yield leads to a decrease in the bulk fields and an increase in the field near the front surface. This situation was discussed above, and is expected within the framework of Meulenber bilayer.<sup>5</sup>

One should also note the behavior of bulk fields for the large  $\sigma_0$  and large  $\delta$  cases. Note that

the bulk field for the later is larger despite the fact that the surface voltage is lower. This is a consequence of the fact that a substantial amount of charge is deposited at depths which are comparable to the sample thickness (50 microns on the figure). Thus, for thin samples in a space-like environment, the surface voltage is not an accurate diagnostic for the bulk fields. Shown in Figure 7 is the charge density associated with the fields of Figure 6. These profiles are consistent with the above discussion.

#### DISCUSSION

The Meulenberg<sup>5</sup> idea that an internal discharge may be initiated in the deposition layer of electron charged dielectric has been invoked. Evidence<sup>2</sup> has been given which shows that internal discharges do occur. Space observations have been noted which suggest that breakdown conditions in space are different from those in "standard" laboratory simulations. A conceptual model was presented which demonstrated that large internal fields could develop with no differential potential. An experimental procedure for realizing these conditions was noted. These conditions obviously favor an internal breakdown mechanism. New calculations were reported which demonstrated that space-like simulations give rise to conditions which favor the internal breakdown mechanism; decreased bulk fields, increased deposition region fields; similar charge densities. Materials parameter variations were explored for the space-like simulation. The resulting changes in internal fields are easily understandable in terms of the general theoretical model. Increased conductivity is an effective deterrent to discharge. Enhanced secondary emission is not, and favors internal discharge.

#### REFERENCES

1. N.J. Stevens, "Utilization of Charging Control Guidelines in Geosynchronous Satellite Design Studies", Spacecraft Charging Technology - 1980, to be published.
2. A.R. Frederickson, "Bulk Charging and Breakdown in Electron Irradiation Polymers", Reference 1, idem. to be published.
3. B.L. Beers, H.C. Hwang, D.L. Lin and V.W. Pine, "Electron Transport Model of Dielectric Charging", in Spacecraft Charging Technology - 1978, AFGL-TR-79-0082, page 209 (1979).
4. B.L. Beers and V.W. Pine, "Electron Beam Charged Dielectrics - Internal Charge Distribution", Reference 1, idem.
5. A. Meulenberg, Jr., "Evidence for a New Discharge Mechanism for Dielectrics in a Plasma", in Spacecraft Charging by Magnetospheric Plasmas, Vol. 47, Progress in Astronautics Aeronautics, A. Rosen, editor, 1976, p. 237.
6. N.J. Stevens, F.D. Berkopec, J.V. Staskus, R.A. Blech, and N.J. Narcisco, "Testing of Typical Spacecraft Materials in a Simulated Substorm Environment", in "Proceedings of the Spacecraft Charging Technology Conference," C.P. Pike and R.R. Loveall, editors, Air Force Surveys in Geophysics, No. 364, AFGL-TR-77-0051, NASA TMX- 73537, 24 February 1977, p. 431.
7. K.G. Balmain, and G.R. Dubois, "Surface Discharges on Teflon, Mylar, and Kapton," IEEE Trans. Nuc. Sci. NS-26, 5146 (1979).
8. R.C. Hazelton, R.J. Churchill, and E.J. Yadlowsky, "Measurements of Particle Emission from Discharge Sites in Teflon Irradiated by High Energy Electron Beams," IEEE Trans. Nuc. Sci. NS-26, 5141 (1979).
9. J.E. Nanevicz and R.C. Adamo, "Spacecraft Charging Studies of Voltage Breakdown Processes on Spacecraft Thermal Control Mirrors," ref. 5, idem. p. 225.
10. T.M. Flanagan, R. Denson, C.E. Mallon, M.J. Treadaway, and E.P. Wenaas, "Effect of Laboratory Simulation Parameters on Spacecraft Dielectric Discharges," IEEE Trans. Nuc. Sci. NS-26, 5134 (1979).
11. J.E. Nanevicz, R.C. Adamo, and B.L. Beers, "Characterization of Electromagnetic Signals Generated by Breakdown of Spacecraft Insulating Materials" in Spacecraft Charging Technology - 1978, AFGL-TR-79-0082, p. 868.
12. E.P. Wenaas, M.J. Treadaway, T.M. Flanagan, C.F. Mallon, and R. Denson, "High Energy Electron-Induced Discharges in Printed Circuit Boards," IEEE Trans. Nuc. Sci. NS-26, 5152 (1979).
13. H.B. Garrett, "Spacecraft Charging - A Review," in Space Systems and Their Interactions with Earth's Space Environment, Progress in Astronautics and Aeronautics, Vol. 71, p. 167, (1980).
14. I. Katz, J.J. Cassidy, M.J. Mandell, G.W. Schnuelle, P.G. Steen and J.C. Roche, "The Capabilities of the NASA Charging Analyzer Program," ref. 3, idem. p. 101.
15. R.C. Adamo, J.E. Nanevicz and N. Grier, "Conductivity Effects in High-Voltage Spacecraft Insulation Materials," ref. 6, idem. p. 669.
16. E.A. Burke, J.A. Wall, A.R. Frederickson; Radiation-Induced Low Energy Electron Emission from Metals, IEEE Trans. Nuc. Sci., NS-19, 193 (1971).
17. E.A. Burke, "Secondary Emission from Polymers," IEEE Trans. Nuc. Sci., NS-27, 1760 (1980).

ORIGINAL PAGE IS  
OF POOR QUALITY



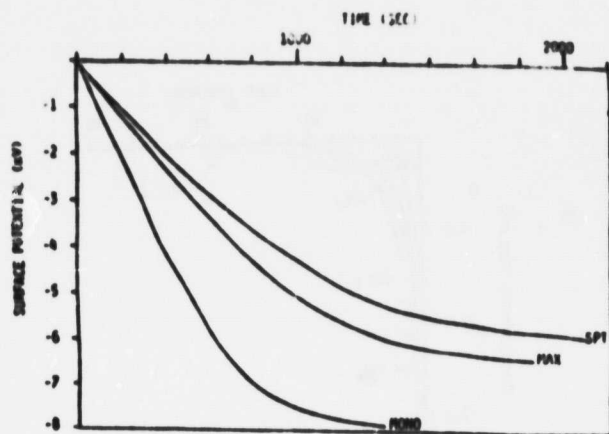


Figure 1.

Surface Potential vs. Time for Three Charging Environments (see text for conditions).

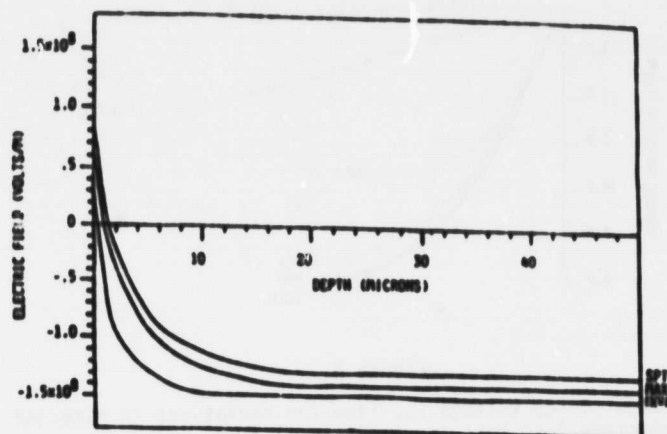


Figure 3.

Saturation Electric Field Profile Internal to Dielectric for Three Charging Environments (see text for conditions).

ORIGINAL PAGE IS  
OF POOR QUALITY.

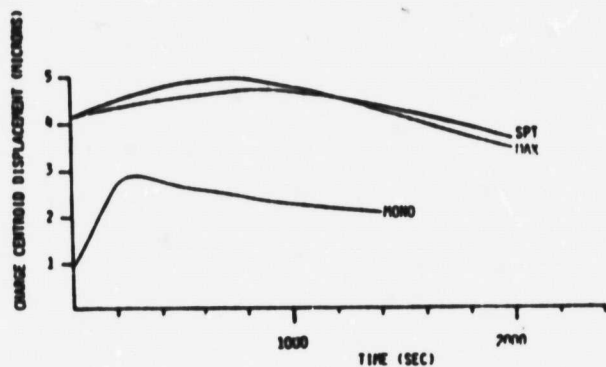


Figure 2.

Charge Centroid vs. Time for Three Charging Environments (see text for conditions).

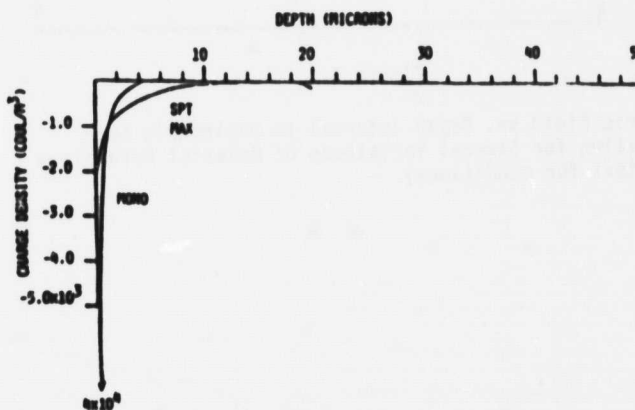


Figure 4.

Charge Density vs. Depth Internal to Dielectric for Three Charging Environments (see text for conditions).

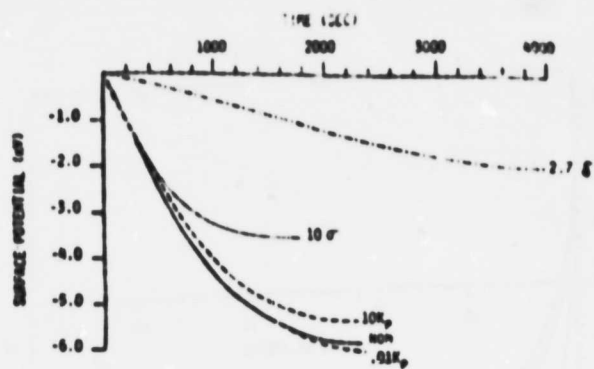


Figure 5.

Surface Charge Voltage vs. Time for Variations in Material Parameters (see text for conditions).

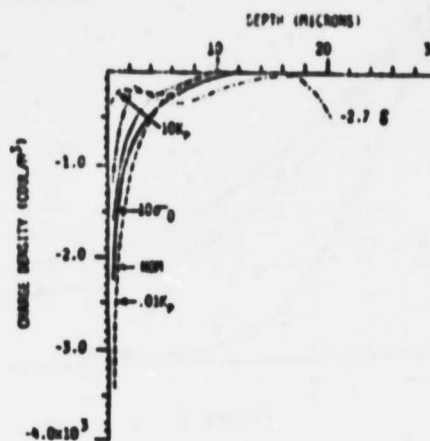


Figure 7.

Charge Density vs. Depth Internal to Dielectric Near Saturation for Several Variations of Material Parameters (see text for conditions).

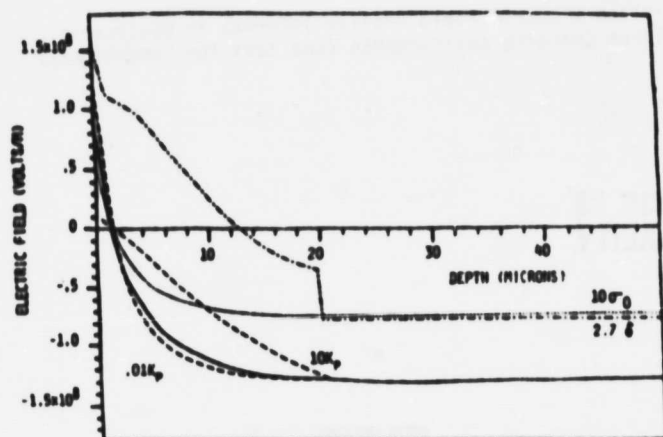


Figure 6.

Electric Field vs. Depth Internal to Dielectric Near Saturation for Several Variations of Material Parameters (see text for conditions).

ORIGINAL PAGE IS  
OF POOR QUALITY

ORIGINAL PAGE IS  
OF POOR QUALITY

#### A P P E N D I X 5

O'Dwyer, J.J. and Beers, B.L., Thermal Breakdown in Dielectrics, 1981 Annual Report, 193, Conference on Electrical Insulation and Dielectric Phenomena, IEEE Electrical Insulation Society, 1981.

ORIGINAL PAGE IS  
OF POOR QUALITY

THEMAL BREAKDOWN IN DIELECTRICS

J. J. O'Dwyer  
Physics Department  
SUNY Oswego, NY 13126

B. L. Beers  
Beers Associates, Inc.  
P.O. Box 2548, Reston, VA 22090

1. Introduction. The basic equations governing thermal breakdown are the heat flow equation

$$C \frac{\partial T}{\partial t} - \text{div} (\kappa \text{ grad } T) = \kappa E^2 \quad (1)$$

and the equation of current continuity

$$\text{div} (\hat{E}) = 0 \quad (2)$$

where the symbols have their usual meanings. The conservation of energy is expressed by Eq. 1, and it is therefore necessary. Equation 2 requires that the dielectric relaxation time  $\epsilon/\sigma$  be much smaller than time intervals considered in the integration of Eq. 1. This condition holds for the examples worked below.

If the electrical conductivity,  $\sigma$ , is not temperature dependent, then the electric field,  $E$ , at any point is determined only by the electrode geometry and the applied voltage. The problem then reduces to that treated in the classic paper by Copple, Hartree, Porter, and Tyson(1) who calculated the transient current for plane parallel electrodes. However, a temperature dependent electrical conductivity is itself a cause of variation in the electric field strength in order to satisfy Eq. 2. This effect has been investigated by Wintle(2) who derived steady state solutions to the equations by analytic methods for special functional forms of the temperature dependence of the electrical and thermal conductivities. In the following we develop transient solutions to the

ORIGINAL PAGE IS  
OF POOR QUALITY

124

equations for thermal and electrical conductivity functions given by

$$\kappa = \kappa_0/T \quad (3)$$

$$\sigma = \sigma_0 \exp(-A/\kappa T) \quad (4)$$

respectively, where  $\kappa_0$ ,  $\sigma_0$ , and  $A$  are constant parameters of the dielectric. These functions are typical of the behavior of alkali halides.

2. Plane Parallel Electrodes. For plane parallel electrodes with the  $z$  coordinate normal to the electrode surfaces, 1 and 2 become with the use of 3 and 4

$$C \frac{\partial T}{\partial t} - \frac{\partial}{\partial z} \left( \kappa_0 \frac{\partial T}{\partial z} \right) = \sigma_0 E^2 \exp(-A/\kappa T) \quad (5)$$

$$j = \sigma E \exp(-A/\kappa T) \quad (6)$$

where  $j$  is the current density. Application of a step function voltage  $V_0$  at  $t = 0$  gives the condition

$$\int_0^d E dz = V_0 \quad \text{for } t > 0 \quad (7)$$

where  $d$  is the electrode separation. Assuming electrodes of large heat capacity gives

$$\left. \begin{aligned} T &= T_0 \quad \text{for } z = 0 \\ &\text{and } z = d \end{aligned} \right\} \quad (8)$$

where  $T_0$  is the ambient temperature.

Solution of the partial differential equation under the conditions 6, 7, and 8a yields the functions  $T(z,t)$  and  $E(z,t)$  which are both symmetric about the mid plane of the dielectric slab. We can therefore replace 8 by

$$\left. \begin{aligned} T &= T_0 \quad \text{for } z = 0 \\ \partial T / \partial z &= 0 \quad \text{for } z = d/2 \end{aligned} \right\} \quad (8a)$$

Finally  $j(t) = \sigma(z,t) E(z,t)$  is not a function of  $z$ , and



can be calculated from 6.

For computations, the following values were taken:  $\kappa_0 = 2000 \text{ W/m}$ ,  $\sigma_0 = 60 \Omega^{-1} \text{ m}^{-1}$ ,  $A = 0.86 \text{ eV}$ ,  $C = 2 \times 10^6 \text{ J/m}^3 \text{ C}^\circ$ ,  $T_0 = 800 \text{ K}$ , and  $d = 5 \text{ mm}$ . Fig. 1 shows the computed current density as a function of time for various applied voltages with the critical voltage apparently about 2.1 kV. Fig. 2 shows the distribution of temperature and electric field within the dielectric after steady conditions have been attained. The field strength at the center ( $z=2.5 \text{ mm}$ ) is about half the average field strength, while near the electrodes it is about four times the average. This suggests the possibility that thermal effects might so distort the field as to produce purely electrical breakdown near the electrodes. The center temperature is about  $150 \text{ C}^\circ$  above the ambient, and this is much higher than the temperature increase expected from the constant field case.

2. Cylindrical Electrodes. For cylindrical geometry with inner and outer electrode radii  $r_1$  and  $r_2$  respectively Eq. 5 is replaced by

$$C \frac{\partial T}{\partial t} - \frac{1}{r} \frac{\partial}{\partial r} \left( r \frac{\kappa_0}{T} \frac{\partial T}{\partial r} \right) = \sigma_0 E^2 \exp(-A/kT) \quad (9)$$

Application of a step function voltage  $V_0$  at  $t = 0$  gives

$$\int_{r_1}^{r_2} E \, dr = V_0 \quad \text{for } t > 0 \quad (10)$$

if the outer electrode is maintained at ambient temperature and the inner one allowed to take up the temperature of the adjacent portion of the dielectric, the boundary conditions become

$$\left. \begin{aligned} T &= T_0 \quad \text{for } r = r_2 \\ \partial T / \partial r &= 0 \quad \text{for } r = r_1 \end{aligned} \right\} \quad (11)$$

Solution of the partial differential equation shows an instability in the current density similar to that shown in Fig. 1. The temperature distribution rises monotonically from ambient near the outer electrode to a maximum near the inner electrode. However, the electric field

distribution shows an interesting development depending on the electrode radii. Figs. 3 and 4 show the electric field as a function of radial distance for an applied voltage of 1.25kV and electrode separations of 5mm. In both cases the applied voltage is slightly in excess of critical voltage. Fig. 3 illustrates the change in field distribution with time when the ratio  $r_2/r_1 = 2$ . At zero time the field non-uniformity is determined by geometry only; after 5s thermal effects plus geometry make the field nearly uniform, and after 10s thermal effects dominate so that the field is large near the outer electrode and small near the central one. Fig. 4 illustrates the different situation that prevails when  $r_2/r_1 = 6$ . In this case, thermal effects make a contribution to the field distortion, but do not overcome the strong geometric contribution.

#### References

1. C. Copple, D. R. Hartree, A. Porter, and H. Tyson, *Proc. IEE*, Vol. 85, p. 56; 1939.
2. H. J. Wintle, *J. Appl. Phys.*, (in press).

#### Acknowledgment

This work was supported in part by National Aeronautics and Space Administration under Contract #NAS 3-22530.

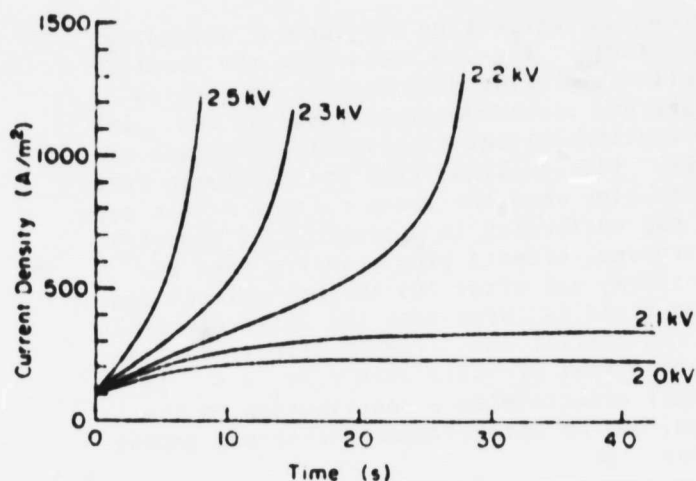


Fig. 1. Current transients for plane parallel electrodes at 5 mm spacing and for parameters quoted in the text. The various potential differences are marked.

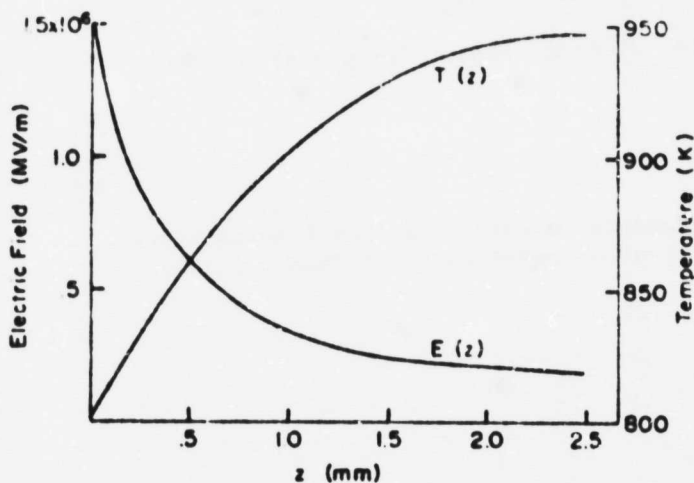


Fig. 2. Variation of temperature and electric field between plane parallel electrodes at 5 mm spacing and 2.1 kV potential difference after attainment of steady conditions.

198

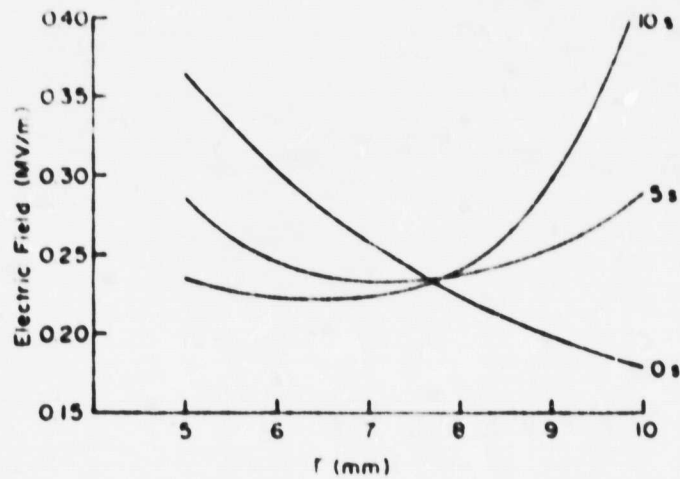


Fig. 3. Variation of electric field between cylindrical electrodes (5 mm and 10 mm radii) 10 s after application of 1.25 kV potential difference.

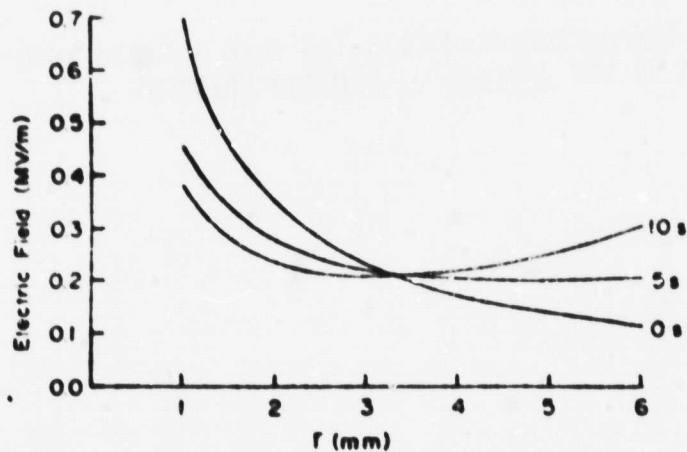


Fig. 4. Variation of electric field between cylindrical electrodes (1 mm and 6 mm radii) 10 s after application of 1.25 kV potential difference.

## A P P E N D I X 6

Reproduced From:

O'Dwyer, J.J., Space Charge Enhanced Emission into a Dielectric Solid,  
paper to be published in the Journal of Applied Physics.

Space Charge Enhanced Emission  
into a Dielectric Solid

ORIGINAL PAGE IS  
OF POOR QUALITY

by J. J. O'Dwyer  
S.U.N.Y. Oswego, NY 13126

Abstract. Collision ionization may occur in a dielectric solid that is subjected to a large electric field, and the positive and negative species produced then constitute space charge within the dielectric. Emission from an electrode into the dielectric can be increased by substantial heterocharge density adjacent to the electrode. It is the purpose of the current work to estimate both the dielectric conduction parameters and the electrode configurations that would be required for significantly enhanced emission.

1. Introduction. We consider steady state current conduction by both electrons and holes in a dielectric in which a strong electric field is causing collision ionization. The conduction current density is given by

$$\vec{j} = n e \mu_n \vec{E} + p e \mu_p \vec{E} \quad (1)$$

where  $n$  and  $p$  are the electron and hole densities, and  $\mu_p$  the corresponding mobilities. The electric field is  $\vec{E}$  and the electron charge is  $e$ . The spatial variation of  $\vec{E}$  is governed by Poisson's equation

$$\vec{\nabla} \cdot \vec{E} = (p - n) e / \epsilon \quad (2)$$

where  $\epsilon$  is the permittivity of the dielectric. The collision ionization

rate per unit time is assumed to be given by

$$\left. \frac{\partial n}{\partial t} \right|_I = \left. \frac{\partial p}{\partial t} \right|_I = n \alpha \mu_n E \exp (-H/E) \quad (3)$$

ORIGINAL PAGE IS  
OF POOR QUALITY

where  $\alpha$  is an inverse length and  $H$  an electric field characteristic of the dielectric. If diffusion and recombination are assumed to be negligible, the equations governing steady state electron and hole density are

$$\begin{aligned} \operatorname{div} (n \mu_n \vec{E}) - n \alpha \mu_n E \exp (-H/E) &= 0 \\ \operatorname{div} (p \mu_p \vec{E}) - n \alpha \mu_p E \exp (-H/E) &= 0 \end{aligned} \quad \} (4)$$

The basic problem is then the solution of the system of equations (1), (2), and (4) for given electrode geometry and electrode emission characteristics.

In a real dielectric, electrode emission probably begins from an asperity and the emitted charge begins to spread as it enters the dielectric. If the electrodes were, for example, parallel planes, then the emitted charge density would be large only at points within a region that spreads from the asperity towards the other electrode. In this case the charge density pattern is not related to the electrode symmetry, and the problem is insoluble without additional assumptions. In order to propose a soluble problem that retains at least some elements of the real situation, we write the equations in a form suitable for spherical geometry with emission taking place from the electrode of smaller radius. In these circumstances there are now two different reasons for enhancement of the electric field in the dielectric. In the first place the spherical geometry results in a higher electric

field near the electrode of smaller radius; secondly, the field near this electrode is further increased by local heterocharge. In the following calculations we separate these effects by quoting a geometric field enhancement factor, and a total field enhancement factor.

2. Computations for Spherical Geometry. Using the spherical form for the divergence and writing the results in the form of finite difference equations, we have from (1), (2), and (4)

$$\Delta E = - \left[ \frac{1}{\epsilon \mu_p} E \left\{ j - j_n \left( 1 + \frac{\mu_p}{\mu_n} \right) \right\} + \frac{2E}{r} \right] \Delta r \quad (5)$$

$$\Delta j_n = \left[ \alpha \exp (-H/E) - \frac{2}{r} \right] j_n \Delta r \quad (6)$$

In addition the total current density obeys the equation

$$\Delta j = - \frac{2}{j} j \Delta r \quad (7)$$

The boundary conditions used with these equations are:

- (1) At the anode  $j = j_n$ , meaning that this electrode is blocking to hole emission
- (2) At the cathode  $j_n = j_n (E_{\text{cath}})$  where the functional form used in the following computations was that for Fowler-Nordheim emission (see e.g. O'Dwyer<sup>1</sup>).

Numerical solution then consists of integrating the equations from the anode to the cathode and imposing the Fowler-Nordheim boundary condition. If the ratio of the electrode radii is greatly in excess of unity, then the first order expressions for the divergence in equations (5), (6), and (7) lead to geometric factors on the field and current densities that are too low. We therefore drop the spherical geometry requirement and



specify the electrode system by its geometric enhancement factor and the interelectrode distance.

The following values were used for various parameters during the computations:

$$\epsilon = 3 \times 10^{-11} \text{ F/m} \quad (\text{corresponding to } \epsilon_r \sim 3.4)$$

$$H = 10^9 \text{ V/m}$$

$$\alpha \text{ Range } 2 \times 10^7 \text{ to } 5 \times 10^8 \text{ m}^{-1}$$

$$\mu_p \text{ Range } 3 \times 10^{-14} \text{ to } 3 \times 10^{-12} \text{ m}^2/\text{Vs}$$

$$\mu_n \text{ Does not enter computation if } \mu_n \gg \mu_p$$

The electrode separation was taken at 90 $\mu$ m unless otherwise noted, and the cathode work function at 2.5eV in the Fowler-Nordheim formula.

Fig 1. shows the current-voltage characteristics for a geometric field enhancement factor of 22. In every case there is a current controlled instability with a certain critical voltage beyond which a negative resistance region corresponds to an unstable current-voltage relation. All curves are marked with the total field enhancement factor that pertains at the critical voltage, and they show that the space charge enhances the field by an additional factor of about 2 to 3 over the geometric enhancement, the exact value depending on the collision ionization coefficient and the hole mobility. Fig 2. shows the same characteristics for an interelectrode spacing of 290 $\mu$ m and geometric field enhancement factor of 165; once again the space charge enhances the field by an additional factor of about 2 to 4.

Fig 3. shows the effect caused by variation of the geometric field enhancement factor while keeping the hole mobility, the electrode sep-

aration, and the collision ionization coefficient constant. The critical current density is relatively unchanged while the critical voltage is lower for larger field enhancement factors. The space charge enhances the field by an additional factor of about 2.5 to 5 over the geometric enhancement, the exact value depending on the electrode geometry. Fig 4. shows the effect of changing the electrode separation while maintaining the other parameters constant. Increased electrode separation results in larger space charge field enhancement, and larger critical voltage but does not change the critical current density. In both Figs 3 and 4 the current density is that near the cathode; this is in contrast to the previous diagrams where the current density refers to the anode.

3. Discussion. Some general conclusions emerge from the computations, showing the effect of varying certain parameters while keeping the others constant.

- (a) An increase in the collision ionization coefficient (all other parameters remaining constant) causes a marked reduction in the space-charge field enhancement factor. The critical current density is not substantially altered.
- (b) An increase in the hole mobility (all other parameters remaining constant) causes a marked increase in the critical current density, together with slight increases in both the critical voltage and the space-charge field enhancement factor.
- (c) An increase in the geometric field enhancement factor (all other parameters remaining constant) caused a marked decrease in the critical voltage, while not substantially altering the critical current density.

- (d) An increase in the electrode separation (all other parameters remaining constant) causes a marked increase in the critical voltage but a decrease in the mean field strength. The critical current is not substantially altered.

In summary it appears that the most critical parameter for the possible existence of collision ionization space charge field enhancement is the hole mobility. For a cathode of radius  $10\mu\text{m}$ , the hole mobility should be of order  $10^{-13} \text{ m}^2/\text{Vs}$  or lower for the effect to occur at reasonable values of current density and voltage. Published results<sup>2, 3</sup> indicate values of this order for polyethylene, but it is not clear that a comparison can readily be made. The computations above consider the holes as the less mobile of the two species involved in collision ionization, and the experimental results on charge carrier mobilities do not relate to the products of collision ionization. Given a sufficiently low hole mobility, the existence of space charge enhancement at a given value of mean field strength is facilitated by the following factors:

- (a) a large collision ionization coefficient
- (b) a large geometric field enhancement factor
- (c) a large electrode separation

In simple terms this means that avalanches of many generations from sharp asperities are most effective in promoting space charge enhanced emission - a fact that could have been seen without detailed computing. The major conclusion, therefore, remains as the estimate of the order of magnitude for the hole mobility ( $< 10^{-13} \text{ m}^2/\text{Vs}$ ) required to produce significant space charge.

Finally a word should be said about the expected effect of tem-

perature. The parameters most affected by a temperature change would probably be  $H$  and  $\mu_p$ , both of which would be expected to increase with increasing temperature. This should cause higher values for both the critical current density and the critical field strength, with the exact details depending on the form of the temperature variation for the parameters in question.

ORIGINAL PAGE IS  
OF POOR QUALITY

### References

1. J. J. O'Dwyer, "The Theory of Electrical Conduction and Breakdown in Solid Dielectrics", (Oxford University Press 1973), p. 77.
2. E. H. Martin and J. Hirsch, J. Appl. Phys. 43, 1001 (1972).
3. K. Hayashi, K. Yoshino, and Y. Inuishi, Jap. J. Appl. Phys. 14, 39 (1975).

ORIGINAL PAGE IS  
OF POOR QUALITY

Captions to Diagrams

Fig 1. Current-voltage characteristics for a geometric field enhancement factor of 22 and an electrode spacing of  $50\mu\text{m}$ . The total field enhancement factors at the critical point are marked on the curves. The collision ionization coefficients refer to the curves above them. The hole mobilities are denoted as follows:

————  $\mu_p = 3 \times 10^{-12} \text{ m}^2/\text{Vs}$

-----  $\mu_p = 3 \times 10^{-13} \text{ m}^2/\text{Vs}$

.....  $\mu_p = 3 \times 10^{-14} \text{ m}^2/\text{Vs}$

Fig 2. Current-voltage characteristics for a geometric field enhancement factor of 165 and an electrode spacing of  $290\mu\text{m}$ . The total field enhancement factors at the critical point are marked on the curves. The collision ionization coefficients refer to the curves above them. The hole mobilities are denoted as follows:

————  $\mu_p = 3 \times 10^{-12} \text{ m}^2/\text{Vs}$

-----  $\mu_p = 3 \times 10^{-13} \text{ m}^2/\text{Vs}$

.....  $\mu_p = 3 \times 10^{-14} \text{ m}^2/\text{Vs}$

Fig 3. Current-voltage characteristics for a range of geometric field enhancement factors leading to the total field enhancement factors marked on the diagram. In all cases the electrode separation was  $90\mu\text{m}$ , the collision ionization coefficient  $10^8 \text{ m}^{-1}$ , and the mobility  $3 \times 10^{-14} \text{ m}^2/\text{Vs}$ .

Fig 4. Current-voltage characteristics for two different electrode separations and the same geometric field enhancement factor of 22. The total field enhancement factors at the critical point are marked on the curves. In both cases the collision ionization coefficient was  $10^8 \text{ m}^{-1}$ , and the hole mobility  $3 \times 10^{-14} \text{ m}^2/\text{Vs}$ .

Fig. 1

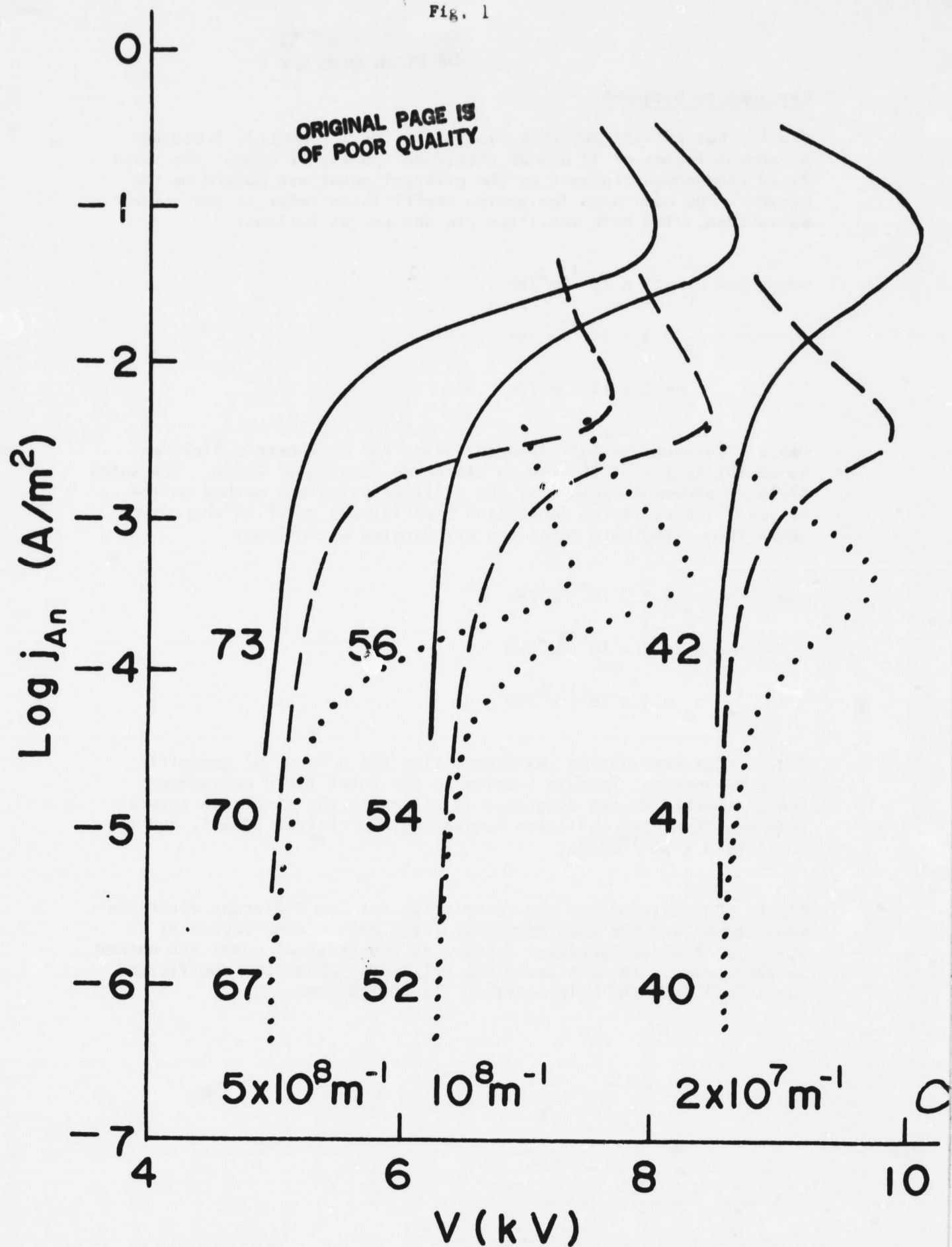


Fig. 2

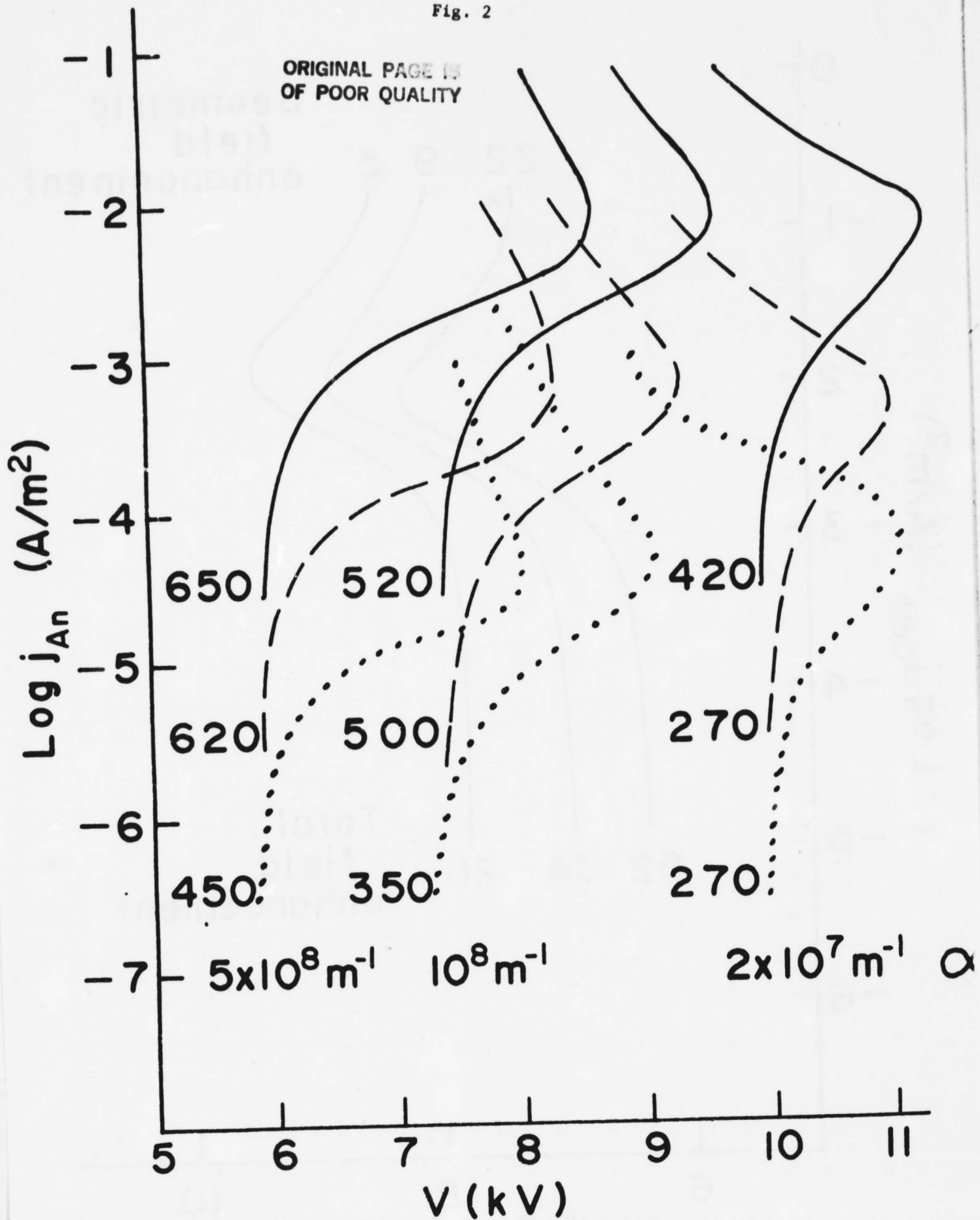




Fig. 3

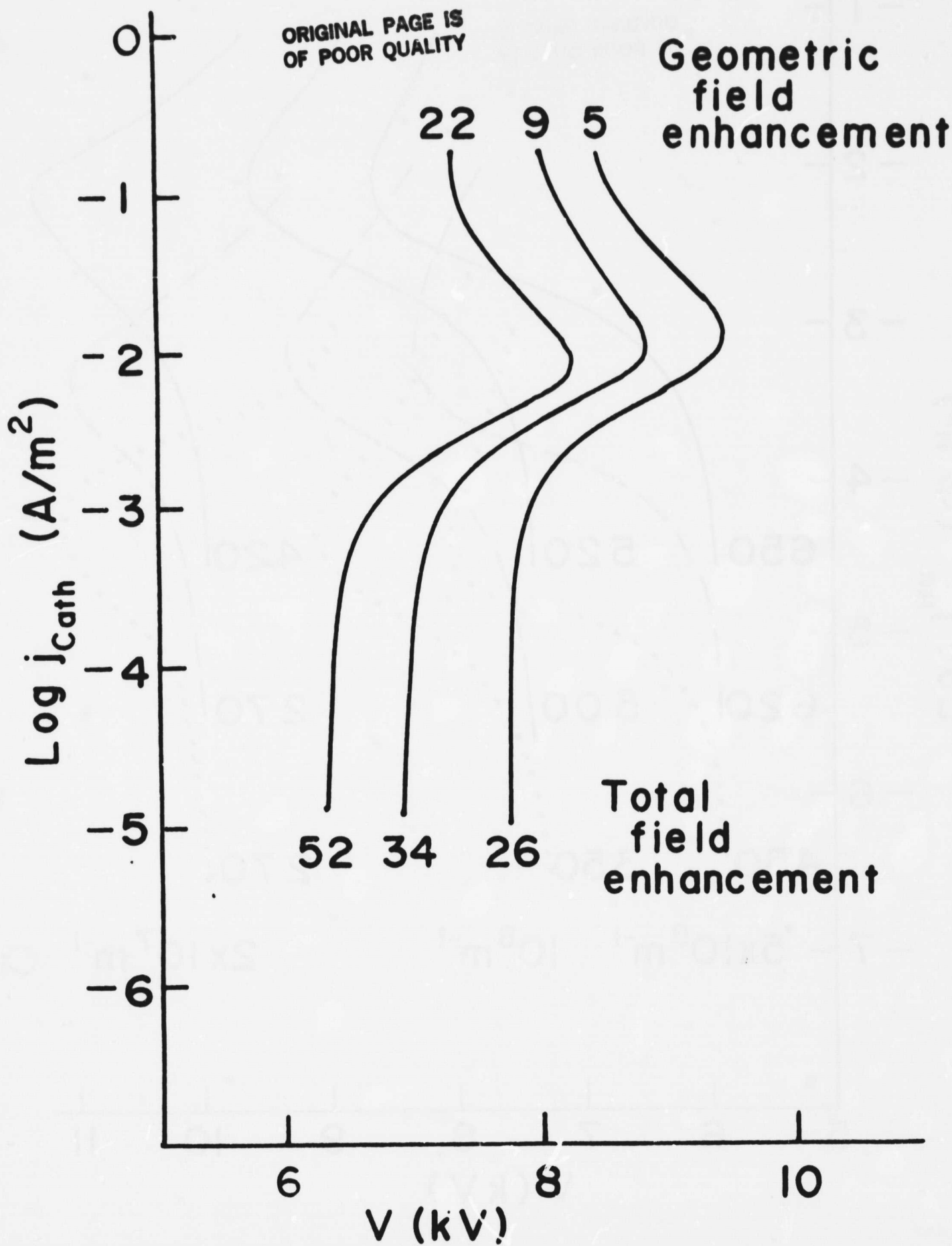


Fig. 4

